Mixed Plasmonic Nanoparticles for Enhanced-Performance Organic Solar Cells

Neda Etebari Alamdari

A Thesis
in
the Department
of
Physics

Presented in Partial Fulfillment of the Requirements
for the Degree of Master of science at
Concordia University
Montreal, Quebec, Canada

February 2013

CONCORDIA UNIVERSITY
SCHOOL OF GRADUATE STUDIES

This is to certify that the thesis prepared

By: Neda Etebari Alamdari

Entitled: Mixed Plasmonic Nanoparticles for Enhanced Performance

Organic Solar Cells

and submitted in partial fulfillment of the requirements for the degree of

Master of Science

complies with the regulations of the University and meets the accepted standards with respect to originality and quality.

Signed by the final examining committee:

Prof. Truong Vo-Van Chair

Prof. Mariana Frank Examiner

Prof. Sushil Misra Examiner

Prof. Truong Vo-Van Supervisor

Prof. Ricardo Izquierdo Co-Supervisor

Approved by

Prof. Truong Vo-Van

Chair of Department or Graduate Program Director

February 21, 2013

Prof. Brian Lewis

Dean of Faculty

ABSTRACT

Mixed Plasmonic Nanoparticles for Enhanced-Performance Organic Solar Cells

Neda Etebari Alamdari

Photovoltaics (PVs) are considered as a promising approach to provide a renewable and environmentally friendly energy source. Ease of process, low-cost, light-weight, optical tunability, mechanical flexibility, semi-transparency and low-temperature fabrication makes organic solar cells (OSCs) a competitive choice in comparison with the currently dominating inorganic polycrystalline and Si-based devices. To commercialize the polymer PVs, however, higher efficiencies will be required. The reason behind the undesirable performance of organic devices is their insufficient light harvesting efficiency which could be enhanced by exploitation of localized surface plasmon resonance (LSPR). The intensified local electric field in the vicinity of metal nanoparticles (MNPs), which is induced by excitation of LSPR, is expected to intensify the light harvesting capacity inside the active layer of OSCs.

In this study, the performance of polymer:fullerene bulk heterojunction (BHJ) OSCs incorporated with various MNPs are investigated. We analyzed the enhancement in optical absorption of poly(3-hexylthiophene):3´-phenyl-3´H-cyclopropa [1,9][5,6] fullerene-C60-Ih-3´-butanoic acid methyl ester (P3HT:PCBM) active medium while MNPs with different shapes, sizes and densities are deposited on top of the indium tin oxide (ITO) modified anode. The characterization results revealed both optical and electrical improvements of fabricated OSCs. A remarkable enhancement of 30% in the power conversion efficiency (PCE) has been achieved, attributed to the plasmonic effect observed in the MNPs.

ACKNOWLEDGMENTS

I would like to express my sincere gratitude to my advisor professor Truong Vo-Van for accepting me in his research group, for his confidence in my abilities and for the continuous support of my master study. I am so grateful for his patience, motivation, enthusiasm, knowledge and expertise as well as his positive attitude during the past two years.

I would like to sincerely appreciate my co-supervisor professor Ricardo Izquierdo for his supportive manner and immense knowledge. His accurate guidance helped me in all time of my research and writing of this thesis. I am so thankful for his encouragements, practical advices and his on-going support during my work at NanoQAM laboratory.

The unique experience of living in Montreal and studying at a prestigious university would not be achievable without the support of professor Mahdi Rezaei Keramati. He has supervised me throughout my undergraduate studies with his deep understanding, wide knowledge and cordial manner.

I am also thankful to all members of our research group both at Concordia University and Université du Québec à Montréal (UQAM). My special thank goes to my dear colleague and friend Alaa Mahmoud for her whole-hearted help, valuable suggestions, kindness, deep knowledge and her great availability during my project. I also wish to thank Dr. Hongjun Gao, as a kind friend and considerate group member, for being so helpful at the time of fixing technical problems.

I would like to gratefully acknowledge Ms. Adrienne Willott for being incredibly helpful at the time of my application for master studies at Concordia University.

I am more than thankful to Mehdi Najafi and his sweet wife Zahra Choolaei for being so supportive, thoughtful and full of energy. I cannot thank them enough for all they have done for me during my stay in Montreal.

Last but foremost, I would like to thank my dearest family; my devoted parents and my beloved brother, for their endless love and priceless support. They have been so close to me, although we have been thousands miles away for the past two years.

DEDICATION

To my beloved family

TABLE OF CONTENTS

LIST OF TABLES IX

LIST OF FIGURES X

LIST OF SYMBOLS XVII

1. INTRODUCTION 1

2. BACKGROUND AND MOTIVATION 4

3. ORGANIC SOLAR CELLS 7

3.1 Operation Principle 7

3.1.1 Light absorption and excitons generation 8

3.1.2 Diffusion of excitons to active interfaces 10

3.1.3 Exciton dissociation 11

3.1.4 Charge transfer and collection 11

3.2 Device Structure 13

3.2.1 Bilayer devices 13

3.2.2 Bulk heterojunction devices 14

3.3 Characterization 18

3.3.1 MIM (Metal-Insulator-Metal) model 18

3.3.2 Current-voltage characteristics 20

3.3.3 Open circuit voltage of OSCs 21

3.3.4 Short circuit current of OSCs 22

3.4 Theoretical assessments 23

4. METAL NANOPARTICLES: PROPERTIES AND APPLICATION IN ORGANIC SOLAR CELLS 26

4.1 Plasmonic Effect 26

4.1.1 The effect of particle geometry and surrounding medium 29

4.1.2 Silver nanoparticles 32

4.1.3 Gold nanorods 36

4.2 Plasmonics Organic Solar Cells 39

5. DEVICE FABRICATION AND CHARACTERIZATION 43

6. RESULTS AND DISCUSSION 51

6.1 Silver Nanospheres-Incorporated OSCs 52

6.2 Gold Nanorods-Incorporated OSCs 59

6.3 Comparison between Incorporated OSCs with either Au NRs or Ag NSs 66

6.4 Bimetallic Nanostructured OSCs 71

6.5 Comparison and Analysis of Results 77

CONCLUSIONS 83

REFERENCES 86

LIST OF TABLES

Table 3-1. Standard parameter set for P3HT:PCBM bulk heterojunction SC. Reproduced from ref. [59]. 23

Table 6-1. Average values for PV parameters for reference and Ag NSs devices along with their corresponding standard deviations. Rs is extracted from the slope of J-V curve in the dark condition at 0.8 V. 55

Table 6-2. Average values for PV parameters for reference and Au NRs devices along with their corresponding standard deviations. Rs is extracted from the slope of JV curve in the dark condition at 0.8 V. 63

Table 6-3. Average values for PV parameters for reference devices as well as the devices with either Au NRs or Ag NSs, along with their corresponding standard deviations. Rs is extracted from the slope of JV curve in the dark condition at 0.8 V. 70

Table 6-4. Average values for PV parameters of reference and Au NRs+Ag NSs dual metallic device along with their corresponding standard deviations. Rs is extracted from the slope of JV curve in the dark condition at 0.8 V. 74

Table 6-5. Average values of PV parameters for reference device as well as the devices with either Au NRs, Ag NSs and Au NRs+Ag NSs along with their corresponding standard deviations. Rs is extracted from the slope of JV curve in the dark condition at 0.8 V. 79

LIST OF FIGURES

Figure 3-1. (a) 3D and (b) 2D energy diagrams of an OSC which represent the four main steps in order to generate photocurrent: (1) light absorption and exciton generation, (2) diffusion of excitons to the donor-acceptor interface, (3) exciton dissociation to free charge carriers, and (4) collection of electrons and holes by their respective electrodes. Reproduced from ref. [27]. 7

Figure 3-2. Absorption coefficient of diverse photoactive materials. Reproduced from ref. [32]...9

Figure 3-3. Correspondence between maximum potential energy generated by an OSC and involved energy levels. Reproduced from ref. [32]. 12

Figure 3-4. A bilayer configuration of an OSC based on PCBM as an acceptor and MDMO-PVP as a donor. Reproduced from ref. [37]. 13

Figure 3-5. (a) Schematic layout structure of a polymer:fullerene BHJ OSC. (b) TEM image of involved layers. (c) AFM and TEM images of photoactive layer (MDMO:PPV/PCBM), the green color in AFM and light gray in TEM represent the polymer phase, and PCBM is shown with red color in AFM and dark gray in TEM; demonstrate the phase separation in a bulk heterojunction layer as a bicontinuous interpenetrating network. Reproduced from ref. [44]. 15

Figure 3-6. (a) Bright field TEM (BF TEM) image, (b) the zoom in, and (c) the schematic representation of the pristine bulk heterojunction P3HT:PCBM blend. The inset in Figure 3-6 (a) is the corresponding selected area electron diffraction (SAED) pattern. Reproduced from ref. [48]. Molecular structure of (d) P3HT and (e) PCBM. 17

Figure 3-7. Nanoscale morphology, device properties, and molecular structure are closely interconnected parameters which affect the performance of an OSC. 17

Figure 3-8. MIM picture of organic diode device under (a) Closed circuit, (b) open circuit, (c) reversed bias, and (d) forward bias conditions. Reproduced from ref. [50]. 19

Figure 3-9. (a) J-V curves of an OSC; Under illumination (full line) and in the dark (dashed line). (b) A simplified equivalent circuit for a solar cell. Reproduced from ref. [50]. 21

Figure 3-10. Calculated J-V curves (a) in the dark and (b) under illumination for a P3HT:PCBM BHJ solar cell; With a device structure of ITO/PEDOT:PSS/P3HT:PCBM/LiF/AL. Reproduced from ref. [59]. 24

Figure 3-11. Numerically calculated impact of electron/hole mobility on PCE of the organic BHJ SC. Reproduced from ref. [59]. 25

Figure 3-12. Effect of cell thickness on the PCE of the polymer: fullerene BHJ OSC. Reproduced from ref. [59]. 25

Figure 4-1. The green Lycurgus cup, while light is illuminating from outside, turns to red when light is shone from inside. The glass contains tiny amount of MNPs which give it this unusual optical characteristic. 27

Figure 4-2. Interaction between the electromagnetic field of incident light with metallic nanoparticles results in the creation of a dipole. Reproduced from ref. [67]. 28

Figure 4-3. (a) Calculated optical absorption spectrum for Ag NPs with different sizes, (b) the relationship between FWHM and the particle radius; the inset represents a linear correspondence between FWHM and the inverse of the radius. Reproduced from ref. [71]. 30

Figure 4-4. Transverse and longitudinal oscillations of conduction band electrons of a metal nanorod due to the interaction with the electromagnetic field of incident light. Reproduced from ref. [87]. 31

Figure 4-5. TEM of Ag NSs with 20 nm, 60 nm, and 100 nm radius. The scale bar is 50 nm. Reproduced from ref. [92]. 33

Figure 4-6. Size-dependent extinction spectra for Ag NSs with various diameters ranging from 10 nm to 100 nm. Reproduced from ref. [93]. 34

Figure 4-7. Relationship between extinction spectra of 50 nm Ag NSs embedded in air, water and silica. As refractive index of the surrounding medium increasing the extinction spectrum red-shifts. Reproduced from ref. [93]. 35

Figure 4-8. (a) Schematic and (b) Calculated representation of the near-field enhancement induced by LSPR effect for an Ag NS. (a) is reproduced from ref. [94] and (b) is reproduced from ref. [95]. 35

Figure 4-9. TEM image of 25 nm diameter Au NRs. Reproduced from ref. [97]. 36

Figure 4-10. Influence of the aspect ratio on the absorption spectra and color of Au NRs. Reproduced from ref. [98]. 37

Figure 4-11. (a) Effect of surrounding medium on the absorbance spectra of Au NRs embedded in different solvents. (b) Alteration in the longitudinal plasmon band position associated with different refractive indexes. Reproduced from ref. [96]. 38

Figure 4-12. Calculated local electric field enhancement in the vicinity of an Au NR with a diameter of 28 nm deposited on the silicon substrate. The polarization of incident light is along the rod axis with a wavelength of λ= 780 nm. Image shows the enhancement (a) in the

central cross-section of the rod and (b) in the top layer of the substrate. Reproduced from ref. [99]. 38

Figure 4-13. (a) Light scattering inside the photoactive material by means of MNPs. This effect intensifies the optical path length and in turn increases the light harvesting. Reproduced from ref. [101], (b) Optical electric field concentration induced by LSPR. Reproduced from ref. [102]. 40

Figure 5-1. Fabrication process of a standard OSC starts with (a) cutting ITO-coated glass substrate, continues with (b) etching and (c-d) ends with incorporation of different appropriate materials with various deposition techniques on top of the patterned ITO. Consequently, the final structure of ITO/PEDOT:PSS/P3HT:PCBM/LiF/Al would be achieved. 43

Figure 5-2. (a) Size distribution and (b) TEM of 40 nm radius Ag NSs. Images are provided by Sigma-Aldrich. 45

Figure 5-3. TEM of 25×60 nm^2 Au NRs. Image is provided by Sigma-Adrich. 45

Figure 5-4. Schematic structure of dually incorporated OSC by the combined nanostructure of Au NRs and Ag NSs on top of the ITO-coated glass substrate. The yellow ellipsoids and gray spheres respresent Au NRs and Ag NSs, respectively. The device structure respects the following sequence: ITO/Au NRs+Ag NSs/ PEDOT:PSS/P3HT:PCBM/LiF/Al. 48

Figure 6-1. Comparison between the absorption spectrum of P3HT:PCBM and the AM1.5 spectrum of the sun. Reproduced from ref. [112]. 51

Figure 6-2. Comparison between absorption profiles of P3HT:PCBM film and Ag NSs solution. 52

Figure 6-3. SEM micrographs of Ag NSs deposited on ITO substrate. The light gray spheres represent Ag NSs. 53

Figure 6-4. J-V characteristics of reference and plasmonic (with Ag NSs) devices (a) under illumination and (b) in the dark. The insets illustrate the semi-log graphs. 54

Figure 6-5. Comparison between absorption profile of pristine P3HT:PCBM film and Ag NSs-incorporated P3HT:PCBM film. Curve D illustrates the absorption enhancement of Ag NSs-integrated film compared to that of the pristine device. 57

Figure 6-6. Absorption enhancement of Ag NSs-incorporated P3HT:PCBM film compared to the pristine P3HT:PCBM. 58

Figure 6-7. Comparison between the absorption profiles of pristine P3HT:PCBM film and Au NRs solution. 60

Figure 6-8. SEM micrographs of Au NRs deposited on ITO substrate. The light gray ellipsoids represent the MNPs. 61

Figure 6-9. J-V characteristics of plasmonic (with Au NRs) and reference (without MNPs) devices (a) in the dark and (b) under illumination. The insets illustrate the semi-log graphs. 62

Figure 6-10. Energy band diagram of the materials which are involved in device structure illustrates a precise compatibility between the work function of Au NRs with that of the PEDOT:PSS and also with the HOMO level of P3HT. Reproduced from ref. [109]. 64

Figure 6-11. Comparison between absorption profiles of pristine P3HT:PCBM film and Au NRs-incorporated P3HT:PCBM film. Curve D illustrates the absorption enhancement of Au NRs-integrated film compared to that of the pristine device. 65

Figure 6-12. Absorption enhancement of Au NRs-incorporated P3HT:PCBM film compared to the pristine P3HT:PCBM. 65

Figure 6-13. Absorption modes of a pristine P3HT:PCBM film (black solid line), an Au NRs colloidal solution (blue dashed line), and an Ag NSs colloidal solution (red dashed line). ..67

Figure 6-14. Comparison between the absorption enhancement of Au NRs-incorporated P3HT:PCBM film with that of Ag NSs-integrated film. 68

Figure 6-15. J-V characteristics of plasmonic (with either Au NRs or Ag NSs) and reference (without MNPs) devices (a) in the dark and (b) under illumination. The insets illustrate the semi-log graphs. 69

Figure 6-16. Absorption modes of a pristine P3HT:PCBM film (black dashed line), an Ag NSs+Au NRs blend colloidal solution (red solid line)..... 71

Figure 6-17. SEM micrographs of Au NRs+Ag NSs dual plasmonic nanostructured colloidal solution deposited on the ITO substrate. The light gray ellipsoids and spheres represent Au NRs and Ag NSs, respectively. 72

Figure 6-18. J-V characteristics of plasmonic (with Au NRs+Ag NSs bimetallic nanostructure) and reference devices (a) in the dark and (b) under illumination. The insets illustrate the semi-log graphs. 73

Figure 6-19. Comparison between absorption profiles of pristine P3HT:PCBM film and (Au NRs+Ag NSs) dual metallic nanostructure-integrated P3HT:PCBM film. The difference between these two films depicted as Curve D..... 75

Figure 6-20. Absorption enhancement of (Au NRs+Ag NSs)-incorporated P3HT:PCBM film compared to the pristine P3HT:PCBM film..... 76

Figure 6-21. Absorption modes of a pristine P3HT:PCBM film (black dashed line), an Au NRs colloidal solution (purple solid line), and an Ag NSs colloidal solution (blue dotted line) and (Au NRs+Ag NSs) bimetallic nanostructure colloidal solution (green dashed line). 77

Figure 6-22. J-V characteristics of plasmonic (with either Au NRs, Ag NSs or Au NRs+Ag NSs) and reference devices (a) under illumination and (b) in the dark.....78

Figure 6-23. Comparative study between PV parameters of OSCs with different conditions. The x axis in all graphs is scaled according to the device number; #1, #2, #3 and #4 stand for reference, Ag NSs, Au NRs, and Ag NSs+Au NRs devices, respectively. Various PV parameters including (a) V_{OC} , (b) FF, (c) J_{SC}, and (d) PCE are investigated. 80

Figure 6-24. Comparison between absorption profiles of P3HT:PCBM film under different conditions: without MNPs(pristine), with Au NRs, with Ag NSs, and with (Au NRs+Ag NSs) dual metallic nanostructure. 81

Figure 6-25. Absorption enhancement of MNPs-incorporated P3HT:PCBM films from that of the pristine P3HT:PCBM one (film I). A comparison between Ag NSs (film III), Au NRs (film II), and Ag NSs+Au NRs integrated films (film IV).....82

LIST OF SYMBOLS

AFM	Atomic force microscopy
Ag NPs	Silver nanoparticles
Ag NSs	Silver nanospheres
AL	Aluminum
Au NPs	Gold nanoparticles
Au NRs	Gold nanorods
BF	Bright field
BHJ	Bulk heterojunction
DI	Deionized
EM	Electromagnetic field
FF	Fill factor
FWHM	Full-width-at-half-maximum
HCL	Hydrochloric acid
HOMO	Highest occupied molecular orbital
I_{MPP}	Maximum power point current

ITO	Indium tin oxide
J_{SC}	Short circuit current density
J-V	Current density-voltage
LD	Exciton diffusion length
LED	Light-emitting diode
LiF	Lithium fluoride
LSPR	Localized surface plasmon resonance
LUMO	Lowest unoccupied molecular orbital
MDMO-PPV	Poly[2-methoxy-5-(3′,7′-dimethyloctyloxy)-1,4-phenylenevinylene]
MIM	Metal-Insulator-Metal
MNPs	Metal nanoparticles
MPP	Maximum power point
NIR	Near infrared
NPs	Nanoparticles
OD	Optical density
OPVs	Organic photovoltaics
OSCs	Organic solar cells
P3HT	Poly(3-hexylthiophene-2,5-diyl)

PCBM	[6,6]-phenyl-C61-butyric acid methyl ester
PCE	Power conversion efficiency
PEDOT:PSS	Poly(3,4-ethylenedioxythiophene) poly(styrenesulfonate)
P_{in}	Incident light power density
PVs	Photovoltaics
R_S	Series resistance
R_{Sh}	Shunt resistance
SAED	Selected area electron diffraction
SCs	Solar cells
SPR	Surface plasmon resonance
TEM	Transmission electron microscopy
V_{MPP}	Maximum power point voltage
V_{OC}	Open circuit voltage

1. INTRODUCTION

Solar energy is one of the most consequential sources of renewable energy along with water power, wind and biomass. Nowadays, due to population increase and ongoing environmental problems there is a compelling demand for green and regenerative energy. The hazardous effect of greenhouse gases caused by fossil fuels and natural oils could be mitigated by using more environmentally friendly energy sources.

On the other hand, the annual output of solar irradiation (5% UV, 43% visible, 52% IR) exceeds by far the world's yearly energy consumption. Therefore, solar energy is considered as a promising replacement for current contaminating and limited energy sources [1]. That is to say, solar energy could be a reliable solution to the problems of climate change and environmental contaminations without any supply limit.

As reported by the International Energy Agency, "the world needs a clean energy revolution in order to break dependence on fossil fuels. Such a revolution would enhance global energy security, promote enduring economic growth and tackle environmental challenges such as climate change. It would break the long-standing link between economic growth and carbon dioxide (CO_2) emissions [2]."

Consequently, converting the energy of light directly into electricity by means of PVs becomes one of the most pertinent research topics nowadays. The demand for fundamentally new technologies in this field stimulated scientific research to develop inexpensive and efficient solar cells (SCs). The extended use of these SCs requires affordable prices as well as high efficiencies comparable to the fossil fuels.

Although during the past decades, SCs technology has been introduced and developed commercially, the global use of PVs is emerging at a slow pace. The reason behind this is high cost of traditional inorganic SCs. Despite the technology advancement which resulted in a remarkable price drop of inorganic PVs, the cost is still unaffordable as compared to that of current energy sources. Moreover, the manufacturing process often leads to the formation of contaminants and invasive chemicals. The inflexibility of inorganic modules is another challenge, which prevents large scale installations [3].

The organic photovoltaics (OPVs) have the potential to contribute significantly to the solar energy market due to their many favorable properties including ease of processing, low-temperature fabrication, light-weight, portability, flexibility and substantial ecological benefits. For polymer-based PVs, there is also the possibility of improving the properties of polymer materials by facile chemical manipulation. The low-cost fabrication and cheaper organic semiconductor materials in comparison with costly inorganic semiconductors would make OSCs more practical devices in the PV market. Moreover, OSCs could be printed out using an inkjet printer resulting in flexible and roll-to-roll devices. This could also facilitate their installation process.

Besides, polymer-based devices could be fabricated with a very thin layer of active material due to their high optical absorption coefficient. However, the OSCs possess quite lower efficiencies than their inorganic counterparts. The low charge carrier mobility and charge collection properties as well as the mismatch between the absorption spectra of the device and the solar radiation could be mentioned as some of the principal obstacles to achieve a highly efficient OSC [3].

Researches on enhanced-efficiency polymer SCs have recently attracted lots of interest both from the scientific community and industry due to their high potential of application.

2. BACKGROUND AND MOTIVATION

Throughout the years, the PV market is dominated by Si-based SCs. Monocrystalline GaAs devices with efficiencies as high as 26% have already been manufactured with a theoretical predicted maximum performance being about 31% for monojunctions and 40% for multijunctions [4].

However, Si-based SC industries are dealing with some serious obstacles, such as resource shortage and high-cost manufacturing process. In order to bring green energy in our day-to-day life through SCs technology, more affordable devices should be developed.

Thus, OSCs can be a reliable substitute for inorganic ones if they could perform at higher efficiencies. The most outstanding property of organic semiconductor-based SCs relies on their facile, green and low-cost fabrication process which leads to inexpensive, flexible and environmentally friendly devices. However, organic devices are still far behind their inorganic counterparts considering their low performance. The most recent reported efficiency of OSCs is around 7.4% [5], which implies a prolonged way to achieve an OSCs-dominated PV market. Morphology-dependent charge transport properties, long-term stability, light-harvesting limitations, photocurrent and efficiency are still the remaining issues at the center of scientific attention in the OSCs field.

From 1986, when the first bilayer OSC was developed by Tang [6], a lot of attempts have been made in order to overcome the drawbacks of increasing the performance of these devices. The PCE of pure conjugated polymer-based SCs is in the range of 1-2 % [7].

Over the years, the performance of standard typical devices enhanced remarkably by various design, material, structure and morphology manipulations such as development of BHJ active layer instead of bilayer structure [8], taking advantage of various buffer layers such as Poly(3,4-ethylenedioxythiophene) poly(styrenesulfonate) (PEDOT:PSS) and lithium fluoride (LiF) [9], morphology modifications [10, 11], investigations on metal electrodes [12, 13], using different active layer materials with different concentrations and deposition techniques [14, 15], and introduction of tandem SCs [16]. However, new technologies should be developed in order to improve the performance of OSCs.

One recent approach is the incorporation of noble MNPs in OSCs which could significantly contribute to the performance of the devices mainly through LSPR and scattering effects. LSPR is defined as the collective oscillations of conduction band electrons at the interface of MNPs and the dielectric environment resonated by the incident light. According to the literature [17, 18], MNPs improved the performance of inorganic SCs due to enhanced light-harvesting efficiency inside the photoactive material via scattering effect.

Regarding organic devices, there have been multiple studies for incorporation of MNPs, either directly on top of the ITO electrode [17, 19, 20] within the hole transport buffer layer [21, 22], or within the BHJ active layer [23, 24, 25] of single-junction OSCs as well as the interconnecting layer of tandem OSCs [18, 26].

The current study, on the other hand, presents a different approach: an efficiency-enhanced BHJ OSC using a dual plasmonic nanostructure consisting of gold nanorods (Au NRs) mixed with silver nanospheres (Ag NSs). In this method, each MNP contributes to the photocurrent and efficiency of OSCs depending on its size, shape and absorption spectra. In other words, different types of MNPs complement each other to broaden the region in which absorption enhancement

takes place. The performance of the devices is first characterized and optimized for deposition of only Au NRs and only Ag NSs on the ITO transparent anode. Afterwards, the effects arising from integration of dual metallic nanostructure on the ITO anode are investigated through various characterization techniques. Finally, a comparison is done among the characteristics of the devices incorporated with only Au NRs, only Ag NSs, and the combined nanostructure of Au NRs and Ag NSs.

The thesis is divided into six chapters starting with a general introduction and continued by background and motivation. The concept of organic solar cells is described in chapter 3. Chapter 4 is dedicated to the characteristics and application of metal nanoparticles. The details of device fabrication and characterization are explained in chapter 5. Finally, the thesis ended up with results of research which were covered in chapter 6.

3. ORGANIC SOLAR CELLS

3.1 Operation Principle

Conventional bilayer OSC was inverted in 1986 by Tang [6]. Since then there have been noticeable improvements in the performance and stability of these cells. The main difference between polymer-based SCs and conventional inorganic devices is the process of converting absorbed light into free charge carriers. That is, the light absorption process inside inorganic semiconductors leads to the creation of free electrons and holes. However, upon light absorption, the polymer-based materials generate bound electron-hole pairs named excitons. Therefore, the charge creation, transport and collection properties would be different in OSCs compared to their inorganic counterparts.

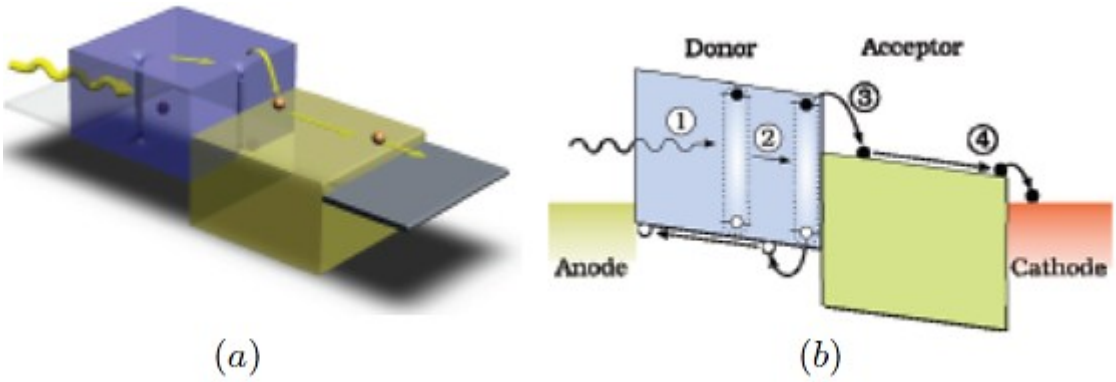

Figure 3-1. (a) 3D and (b) 2D energy diagrams of an OSC which represent the four main steps in order to generate photocurrent: (1) light absorption and exciton generation, (2) diffusion of excitons to the donor-acceptor interface, (3) exciton dissociation to free charge carriers, and (4) collection of electrons and holes by their respective electrodes. Reproduced from ref. [27].

As it is shown schematically in Figure 3-1, the basic mechanism of photocurrent generation inside an OSC could be explained in 4 main steps [15],

- Light absorption and excitons generation
- Diffusion of excitons to active interfaces
- Charge separation
- Charge transport and collection

In order to convert the incident light directly into electricity by means of an OSC, there should be an active layer which is basically made of two photoactive materials in which the light absorption and generation of excitons take place. The photogenerated excitons are supposed to be diffused and dissociated to free electrons and holes. The free charge carriers would be collected by two metallic electrodes, between which the active area is sandwiched. One of the electrodes, namely either the cathode or the anode, is transparent in order to transmit the incident light inside the device.

3.1.1 Light absorption and excitons generation

In order to optimize the amount of transferred light into the absorbing layer, the first material in the device structure that encounter with photons should be as transparent as possible. This could minimize the losses through reflections at the air-substrate interfaces. During light incidence from one layer to another, light losses could be minimized by reducing the difference of the optical refractive index between two sequential layers. The device reflectance depends on all layers and it is different from the reflectance in air-substrate interface. Light-harvesting could be enhanced by any redirecting of incident light due to the path length increase inside the device. Dielectric functions of layers, layer ordering and thickness of layers are of great importance considering

antireflection losses [28]. Losses are also reducible by surface patterning such as one-dimensional gratings [29].

A mismatch between the absorption spectrum of the photoactive organic layer and solar spectrum could negatively affect the efficiency of photon collection of the device. The active layer should be thick enough to efficiently absorb the incident light. The optimal thickness of the active layer of a typical polymer-based device is in the order of 100-200 nm, which results in low absorption of incident light. Increasing the thickness, however, causes low carrier mobilities and in turn results in higher device resistance [18, 30]. A detailed investigation about the impact of the active layer thickness on the performance of BHJ SCs could be found in the literature [31].

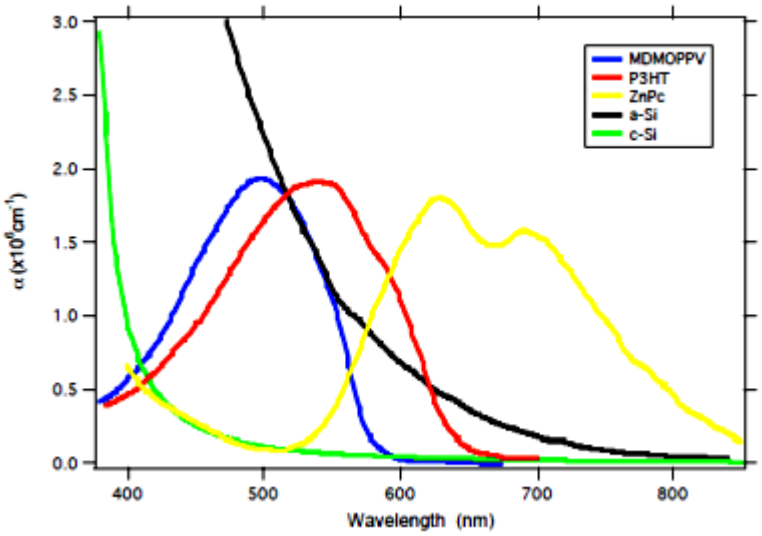

Figure 3-2. Absorption coefficient of diverse photoactive materials. Reproduced from ref. [32].

In general, organic materials possess higher optical absorption coefficient (α) as compared with that of crystalline or multicrystalline silicon. As it is shown in Figure 3-2, P3HT possesses an optical absorption coefficient of more than 10^5 cm^{-1} in the visible spectrum region. Due to the lack of light absorption in the red and near infrared (NIR) part of the spectrum for P3HT and Poly[2-methoxy-5-(3′,7′-dimethyloctyloxy)-1,4-phenylenevinylene] (MDMO-PPV), recent

researches are focused on developing of organic polymers with an optical band in the NIR as well. These materials are named small band-gap polymers [33, 32]. A band gap of 1.1 eV (1100 nm) could absorb approximately 77% of the incident light. Since the semiconductor polymers usually have higher band gaps around 2 eV (620 nm), the light harvesting of solar irradiation on earth reduces to 30% [34]. After light absorption inside the photoactive material, electrically neutral excitons are generated.

3.1.2 Diffusion of excitons to active interfaces

For an ideal device, all generated excitons lead to the creation of free electrons and holes. However, this value is confined by re-emitting of a photon in luminescence or radiative recombination to the ground state. Considering the conjugated polymers as the active material, it is estimated that only 10% of the photoexcitations ends up as free charge carriers [35].

The exciton diffusion length, L_D, is defined as the distance that an exciton could cross during its lifetime. It is typically in the order of 10 nm, however, its precise value is determined by the device structure and the dielectric environment [36].

Since the exciton transport is restricted by radiative and nonradiative decay processes, the life time of an exciton corresponds to the reciprocal value of all these decay rates. For molecular material, this value is estimated around only several nanoseconds. For an efficient device, excitons should reach the photoactive interface during this period of time. In other words, only the excitons which are generated in few nanometers distance (less than L_D) around the interface could contribute to charge separation. This area is known as diffusion zone. Consequently, to increase the charge separation probability all excitons should be generated within the diffusion zone.

3.1.3 Exciton dissociation

Transformation of excitons to free charge carriers occurs at dissociation sites which are photoactive interfaces of two dissimilar materials with different electron affinities. Strong electric fields are necessary for efficient charge separation. Both internal and external electric fields could contribute to this phenomenon. A strong local electric field is created at the interfaces where sharp changes of the potential energy take place [37].

If the created electric field is too weak for separation beyond electrostatic attraction, two kinds of free charge carrier loss might occur including geminate and nongeminate recombinations. Geminate recombination is defined as a recombination of a dissociated electron and hole and regeneration of an exciton. On the other hand, if an electron and a hole from different excitons recombine, it is introduced as biomolecular nongeminate recombination [28, 38].

3.1.4 Charge transfer and collection

The separated free charge carries should be transported towards the appropriate electrodes in order to contribute to the photogenerated current. Since electrons and holes possess different mobilities in the material, they might trap into localized states. There is a correspondence between the distance that free charge carriers move in order to reach electrodes and the possibility of getting trapped. Therefore, a thin active layer is better than a thick one. However, thinner active layer results in a lower optical absorption, since the light harvesting efficiency is proportional to the thickness of the photoactive material.

Efficient charge transportation occurs if there is a strong enough driving force to push the free electrons and holes towards the electrodes. The difference between the highest occupied molecular orbital (HOMO) of the donor and the lowest unoccupied molecular orbital (LUMO) of

the acceptor creates a gradient at the donor-acceptor junction. This internal electric field not only controls the maximum value of open circuit voltage (V_{OC}) but also intensifies charge carrier transportation to the electrodes (Figure 3-3).

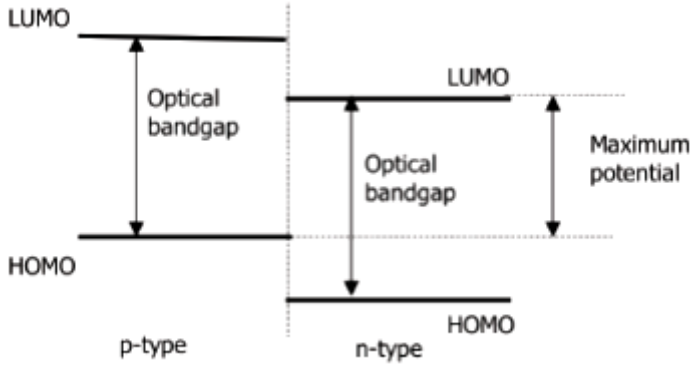

Figure 3-3. Correspondence between maximum potential energy generated by an OSC and involved energy levels. Reproduced from ref. [32].

Taking advantage of asymmetrical contacts, one with low work-function metal for the collection of electrons and one with high work-function metal for the collection of the holes, gives rise to the driving power required to pass on the electrons and holes. Finally, the charge carriers are supposed to be collected by electrodes. The best choice would be a positive anode which matches with HOMO level of the active layer polymer (i.e. ITO and P3HT), and a negative metallic cathode such as aluminum (AL) matches with LUMO level of the acceptor material (PCBM). The transport phenomenon in organic semiconductors is investigated with more details in the literature [39, 40].

3.2 Device Structure

3.2.1 Bilayer devices

The first OSCs were formed using a single layer of organic material sandwiched between two dissimilar electrodes, in which the PV characteristics were determined by the nature of these electrodes. The heavily conjugated photoactive materials resulted in the highest possible efficiency of 0.3% for this design. A demand for devices with better performance induced the development of a double-layer heterojunction structure that consisted of p-type and n-type organic semiconductors, which was introduced by Tang in 1986.

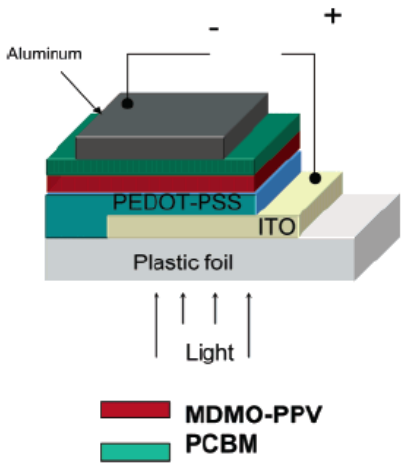

Figure 3-4. A bilayer configuration of an OSC based on PCBM as an acceptor and MDMO-PVP as a donor. Reproduced from ref. [37].

It was made of copper phthalocyanine as the electron donor, and a perylene tetracarboxylic derivative as the electron acceptor. Two dissimilar electrodes, including ITO and Ag were responsible to collect positive and negative charges, respectively. The Power Conversion

Efficiency of the device was around 1% under AM2 illumination [6]. Figure 3-4 represents a bilayer configuration using MDMO-PPV and PCBM as organic semiconductors. The photoactive material of bilayer design was largely investigated throughout the years [41, 42].

However, the efficiency remained poor due to the limited interfacial area between n- and p-type organic materials. In this design, only the excitons formed within the L_D distance from the interface could reach the dissociation sites. The other photogenerated excitons further away from the diffusion zone were diminished since they were not able to reach the donor-acceptor interface before they lost their excitation energy. This limit on the performance of OSCs was solved by the development of BHJ concept which could give rise to the interfacial area between donor and acceptor.

3.2.2 Bulk heterojunction devices

Solution-processed BHJ PVs were first reported in 1995 [8]. It is defined as a nanoscale interpenetrating network composed of a donor-acceptor blend. In which a 10-20 nm phase separation length scale is the reason behind the prolonged interfacial between two combined organic semiconductors. Applying this structure results in the photogeneration of all excitons within the diffusion length. Therefore, irrespective of the active layer thickness, these created electron-hole pairs could contribute to the charge separation process and in turn improve the efficiency of the OSCs.

Morphology of the solution became one of the most consequential challenges since the separated free charge carriers should be able to reach the electrodes. Inside the mixture, however, there is no preferred direction for internal fields of electrons and holes. This means there should be a strong driving force to navigate them towards corresponding electrodes. Moreover, the pathways

through which all free charges could transfer to the electrodes are required. Holes are supposed to be transported by p-type semiconductor and electrons by n-type material so the mixture should be a bicontinuous and interpenetrating network [43]. One of the first and the most utilized BHJ photoactive materials were achieved by mixing PCBM and MDMO-PPV as the acceptor and donor, respectively. The schematic structure of MDMO-PPV:PCBM bulk heterojunction OSC along with Atomic force microscopy (AFM) and Transmission electron microscopy (TEM) images of active material are depicted in Figure 3-5.

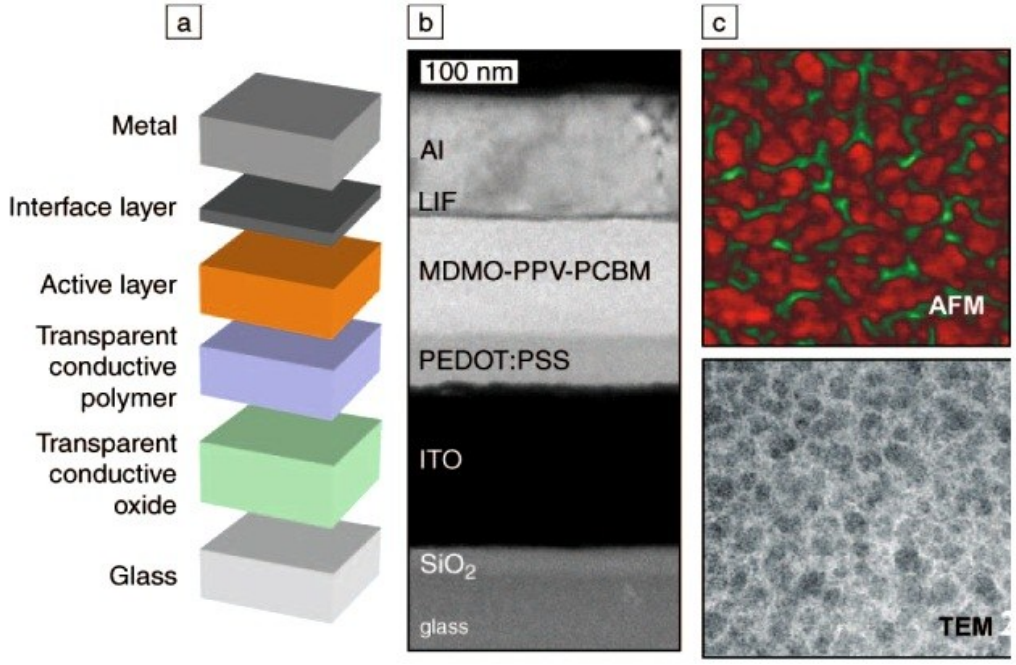

Figure 3-5. (a) Schematic layout structure of a polymer:fullerene BHJ OSC. (b) TEM image of involved layers. (c) AFM and TEM images of photoactive layer (MDMO:PPV/PCBM), the green color in AFM and light gray in TEM represent the polymer phase, and PCBM is shown with red color in AFM and dark gray in TEM; demonstrate the phase separation in a bulk heterojunction layer as a bicontinuous interpenetrating network. Reproduced from ref. [44].

A mismatch between the solar radiation spectrum and the absorption spectrum of the active material is one of the limiting factors in order to achieve high current densities in OSCs. Moreover, polymer semiconductors normally possess low charge carrier mobilities which could be considered as another delimiting parameter.

In this regard, P3HT is known as a low band gap and high charge carrier mobility polymer semiconductor. This is the reason behind substituting P3HT:PCBM blend for MDMO-PPV:PCBM. P3HT with a band-gap energy of 1.85eV absorbs photons with wavelengths smaller than 675 nm. If the polymer defines the optical absorption of the composite, P3HT:PCBM could absorb 27% of the available photons and 44.3% of the available power [33]. A polymer with a band-gap as low as 1.1 eV would increase the absorption of solar photons by up to 77% [34].

Figure 3-6 illustrates FEM image of P3HT:PCBM as well as the molecular structure of P3HT and PCBM. Research in this area is still ongoing in order to achieve enhanced-performance BHJ OSCs by means of new materials and low band-gap polymers [45, 46].

Furthermore, polymer-based devices are dealing with degradation and stability problems. Since the active material is affected by oxygen and water, it should be protected from ambient air. Hence, the stability becomes a crucial parameter in OSCs along with the nanomorphology [47].

Altogether, the performance of BHJ OSCs is influenced by nanoscale morphology, device properties and the molecular structure (Figure 3-7).

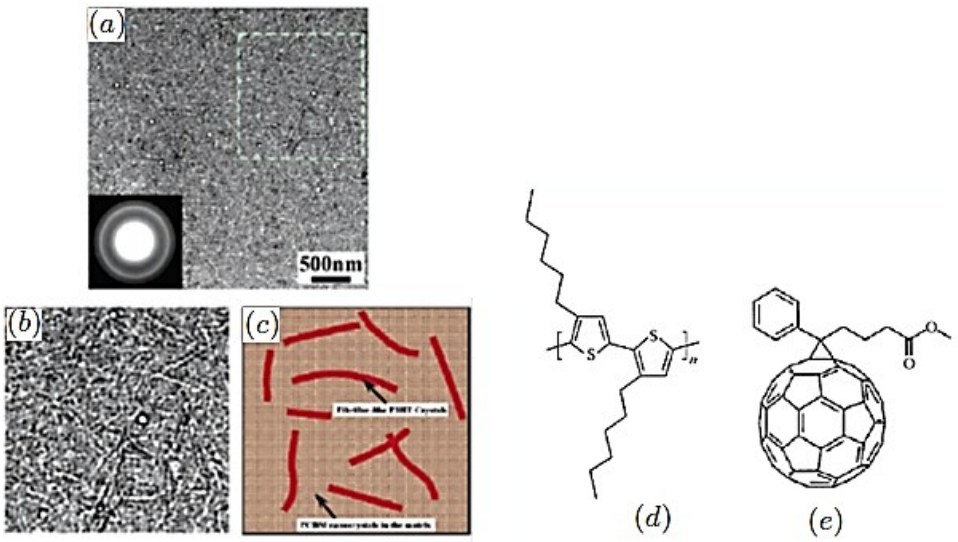

Figure 3-6. (a) Bright field TEM (BF TEM) image, (b) the zoom in, and (c) the schematic representation of the pristine bulk heterojunction P3HT:PCBM blend. The inset in Figure 3-6 (a) is the corresponding selected area electron diffraction (SAED) pattern. Reproduced from ref. [48]. Molecular structure of (d) P3HT and (e) PCBM.

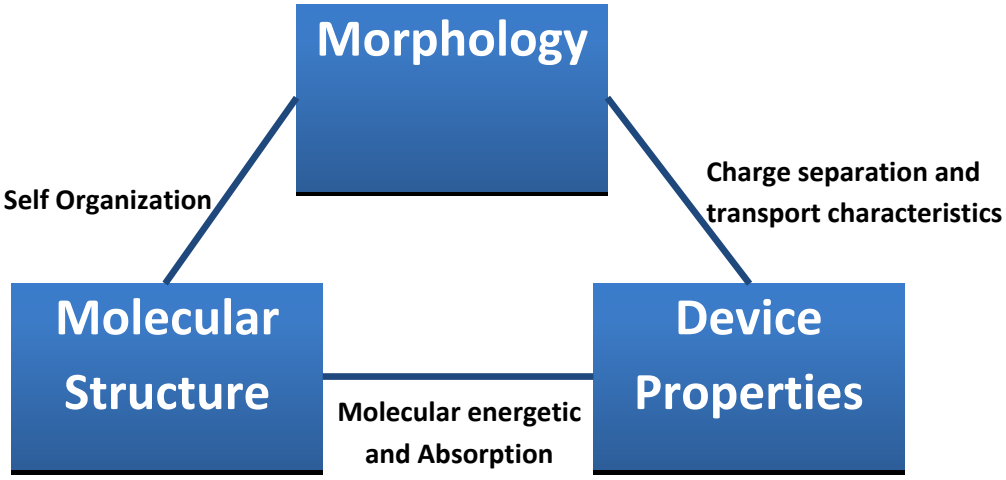

Figure 3-7. Nanoscale morphology, device properties, and molecular structure are closely interconnected parameters which affect the performance of an OSC.

3.3 Characterization

The number of free charge carriers collected by the electrodes corresponds to the electric field produced by a device. The photogenerated current is determined by the charge separation, transportation and collection process which has already been introduced in chapter 1.2. There are some limiting factors which affect the number of absorbed photons such as the absorption coefficient and the thickness of the absorbing material, the multiple reflections from various layers of the device like electrodes, and a mismatch between the absorption spectra of the light absorbing layer and solar irradiation spectrum. The probability that excitons would be generated within the diffusion zone and also would be separated in the dissociation sites is a key factor which determines the fraction of dissociated electron-hole pairs [49].

Altogether, the photocurrent efficiency (η_j) depends on the fraction of absorbed photons (η_{abs}), the fraction of dissociated excitons (η_{diss}), and the fraction of free electrons and holes which could reach the electrodes (η_{out}), $\eta_j = \eta_{abs}\eta_{diss}\eta_{out}$ [50].

3.3.1 MIM (Metal-Insulator-Metal) model

The Metal-Insulator-Metal (MIM) model [51] could explain the different conditions in which an undoped semiconductor device is characterized in the dark. Figure 3-8 shows a rectifying behavior of an intrinsic semiconductor. Following the general structure of an SC, the thin-film layer is sandwiched between two electrodes with different work functions namely Al and ITO. Fermi levels represent the metal electrodes. The semiconductors, however, are depicted by their valence and conduction bands corresponding to the molecular HOMO and LUMO levels [28, 50].

Closed circuit condition: (Figure 3-8.a) There is neither a built-in electric field nor a net current flowing since there is no applied voltage. The Fermi levels are aligned with each other. Under illumination, however, the free charge carriers are transferred to their corresponding electrodes via this electric field. Electrons can drift from LUMO of the acceptor to the low work function electrode (cathode) and from HOMO of the donor to the high work function electrode (anode).

Open circuit condition: (Figure 3-8b) The applied voltage, which is called open circuit voltage, balances the built-in field. Therefore, there is no driving force and in turn the photogenerated current of the device would be zero.

Reverse bias condition: (Figure 3-8c) Anode and cathode act as negative and positive electrodes, respectively. The photogenerated charges drift in strong electric field towards their corresponding contacts resulting in a high current flow.

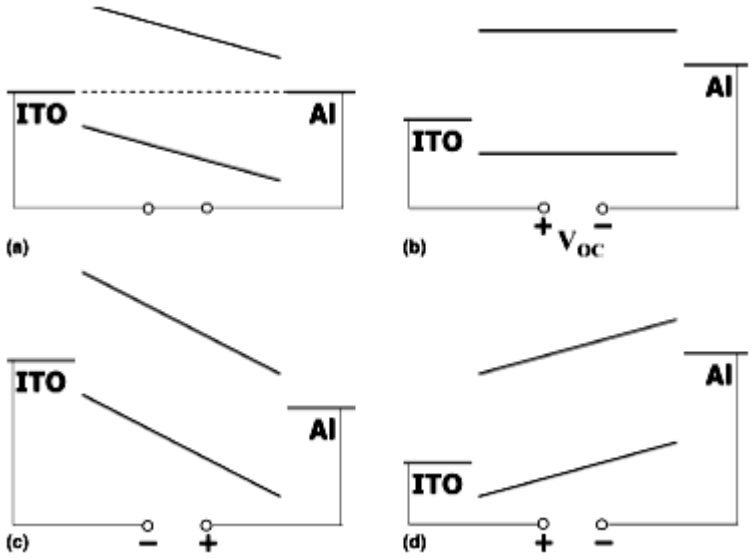

Figure 3-8. MIM picture of organic diode device under (a) Closed circuit, (b) open circuit, (c) reversed bias, and (d) forward bias conditions. Reproduced from ref. [50].

Forward bias condition (larger than V_{OC}): (Figure 3-8d) Electrons are injected from cathode (Al) to LUMO of the acceptor and holes are injected from anode (ITO) to HOMO of the donor. The device works as a light-emitting diode (LED) if these charges can recombine radiatively [28, 50].

3.3.2 Current-voltage characteristics

J-V characteristics for an SC under illumination and in the dark are shown in Figure 3-9-a. In the dark, current starts to flow in forward-bias while the applied bias exceeds the open circuit voltage. Under illumination, J_{SC} represents the maximum photocurrent which flows in a short circuit condition.

V_{OC} is the open circuit voltage in which there is no current flow. The output power generated by the device is determined by the product between current and voltage, which is shown in the fourth quadrant between V_{OC} and J_{SC}.

The maximum output power, named maximum power point (MPP), is obtained where this product is optimized. I_{mpp} and V_{mpp} are respectively the current and the voltage at this point. The power conversion efficiency of the device is given by $\eta_e = (V_{OC} \times J_{SC} \times FF)/(P_{in})$ and $FF = (I_{mpp} \times V_{mpp})/(J_{SC} \times V_{OC})$,where P_{in} is the incident light power density which should respect the standard AM 1.5 spectrum [52], and FF is the fill factor which calculates the applicable part of the V_{OC} and J_{SC} product.

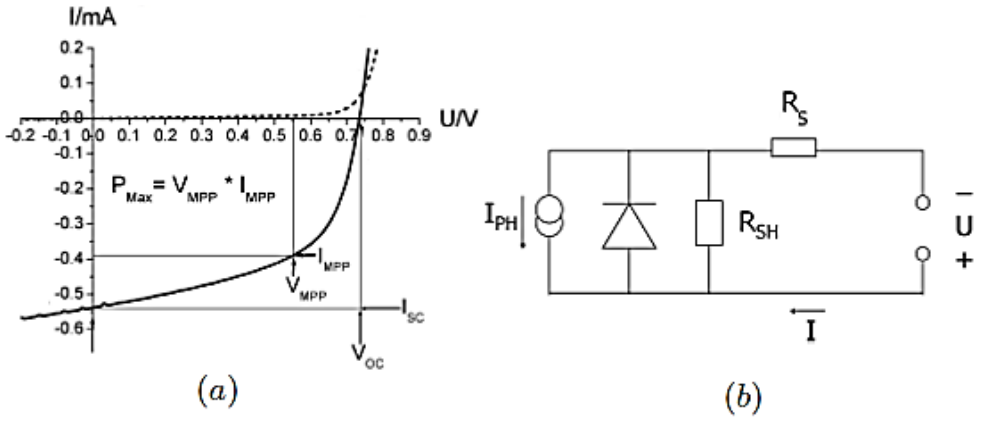

Figure 3-9. (a) J-V curves of an OSC; Under illumination (full line) and in the dark (dashed line). (b) A simplified equivalent circuit for a solar cell. Reproduced from ref. [50].

Figure 3-9-b represents a simplified equivalent circuit of an SC device in which I_{ph} stands for the generated photocurrent under illumination, I_d represents the diode current which is in the opposite direction of that for the diode, R_{sh} stands for the shunt resistance which arises from the potential leakage current of the device, and finally R_s represents ohmic series resistance, which results from the active layer and electrodes contact. The device should be free of "shorts" between electrodes to maximize the parallel shunt resistance and in turn achieve a high-performance SC. In contrast with R_{sh}, R_s should be minimized to increase the overall efficiency, and specifically FF [50]. The slopes of J-V curve at V_{OC} and J_{SC} show the series and shunt resistance, respectively.

3.3.3 Open circuit voltage of OSCs

In OSCs, the open circuit voltage depends on the energy difference between HOMO of the donor

(quasi Fermi level of p-type semiconductor) and LUMO of the acceptor (quasi Fermi level of the n-type semiconductor). The nanomorphology of the active layer has a crucial impact on the V_{OC} of the polymer fullerene BHJ SCs [53, 54].

Moreover, charge carrier losses at the interfaces of electrodes and photoactive layer could lower the $V_{OC.}$ The surface of ITO could be modified with plasma etching or by deposition of a thin layer of hole conducting transparent organic material in order to match the HOMO of the photoactive material and energy levels of the anode. The same modification could be done for the cathode by adding a thin layer of LiF between Al and active material. Furthermore, metal-organic semiconductor interfacial properties such as work function alternations could affect V_{OC}. In depth studies about the reciprocal effects between V_{OC} and OSCs characteristics could be found in the literature [55, 56].

3.3.4 Short circuit current of OSCs

Assuming an ideal device, short circuit current density (J_{SC}) mainly depends on the charge carrier mobility and photoinduced charge carrier density of photoactive organic material. If the efficiency of photoinduced charge generation and in turn the density of corresponding charge carriers is given according to the absorption profile of the device, the variable parameter would be the mobility.

All the factors that affect the nanomorphology of the active material such as deposition techniques, solvent type and crystallization time have a direct impact on the short circuit current density of the SC. Therefore, optimization of J_{SC} becomes possible by controlling the nanoscale morphology of the device [37].

3.4 Theoretical assessments

Modeling and simulations have always been one of the complementary tools in order to estimate the theoretical performing limits of devices [57, 58].

In this section, some results of numerical calculations are provided for characterization of P3HT:PCBM bulk heterojunction OSCs which are all reproduced from ref. [59].

The simulated polymer:fullerene device is influenced by generation, transportation and collection properties of charge carriers. The structure of ITO/PEDOT:PSS/P3HT:PCBM/LiF/Al is considered with thickness of ITO=140 nm, PEDOT:PSS=50 nm, P3HT:PCBM=100 nm and Al= 100 nm. The standard parameter set for P3HT:PCBM device is given in Table 3-1.

Table 3-1. Standard parameter set for P3HT:PCBM bulk heterojunction SC. Reproduced from ref. [59].

Parameter	Symbol	Value
p-contact: ITO/PEDOT-PSS work function	Φ_{m1}	4.7 eV
n-contact: Al/LiF work function	Φ_{m2}	4.3 eV
Effective medium: P3HT/PCBM		
Thickness	d	100 nm
Band gap	E_g	1.05 eV
Electron affinity	χ	3.95 eV
Electron mobility	μ_n	$2 \times 10^{-3}\,cm^2V^{-1}s^{-1}$ [Mihailetchi *et al.*, 2006]
Hole mobility	μ_p	$2 \times 10^{-3}\,cm^2V^{-1}s^{-1}$ [Mihailetchi *et al.*, 2006]
Conduction band effective density of state	N_C	$1 \times 10^{-19}\,cm^{-3}$
Valence band effective density of state	N_V	$1 \times 10^{-19}\,cm^{-3}$
Electron thermal velocity	v_{th}	$1 \times 10^{7}\,cms^{-1}$
Hole thermal velocity	v_{th}	$1 \times 10^{7}\,cm^{-1}$
Dielectric constant (relative)	ε_s	4
Maximum absorption constant	α_{max}	$1.0 \times 10^{5}\,cm^{-1}$
Wavelength of maximum absorption	λ_{max}	650 nm

Furthermore, J-V characteristics of the device are shown in Figure 3-10.

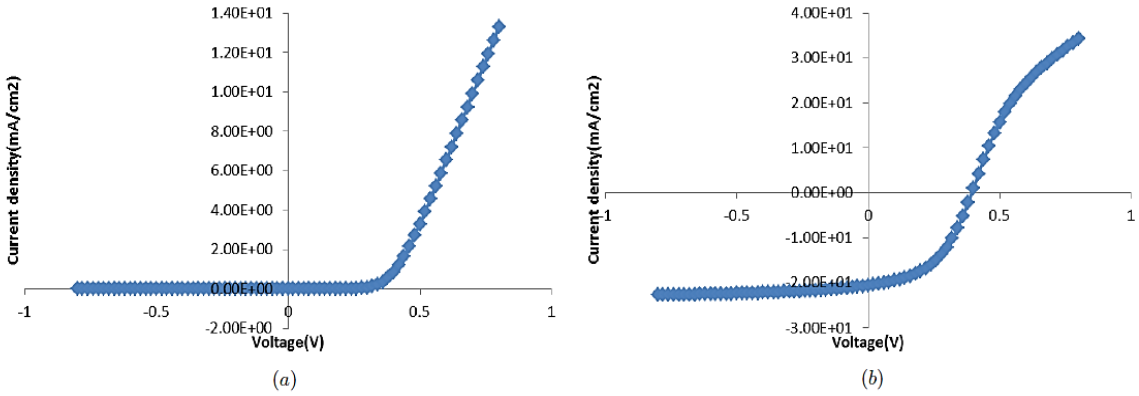

Figure 3-10. Calculated J-V curves (a) in the dark and (b) under illumination for a P3HT:PCBM BHJ solar cell; With a device structure of ITO/PEDOT:PSS/P3HT:PCBM/LiF/AL. Reproduced from ref. [59].

The acquired SC parameters are V_{OC} =0.39V, J_{SC}=20.61 mA/cm^2, FF=48% and PCE=3.88%. Moreover, the influence of the free charge carriers mobility on PCE of the device has been studied as it is shown in Figure 3-11. J_{SC} increases by the enhancement of the charge carrier mobility, however, lower PCE at high mobilities results from lower V_{OC}.

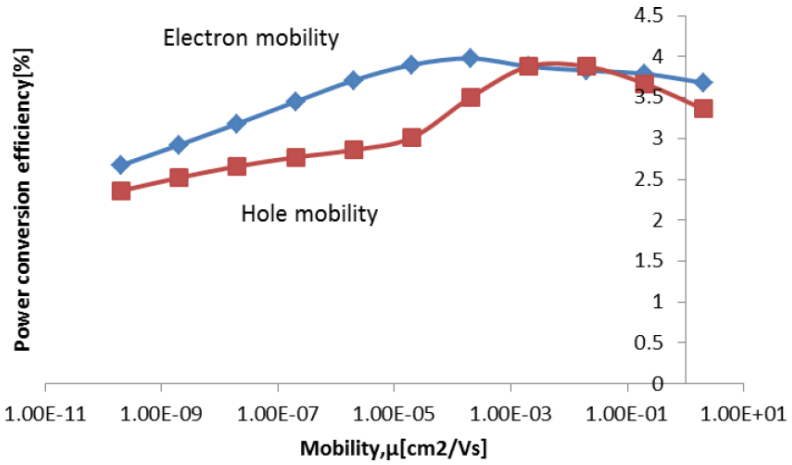

Figure 3-11. Numerically calculated impact of electron/hole mobility on PCE of the organic BHJ SC. Reproduced from ref. [59].

Finally, the effect of active layer thickness on PCE is discussed. According to the results depicted in Figure 3-12, there is a point in which the efficiency is optimized.

As explained previously in this chapter, increasing the thickness of an organic semiconductor BHJ layer correspondingly enhances the device resistance. On the other hand, very thin layer leads to low absorption of light.

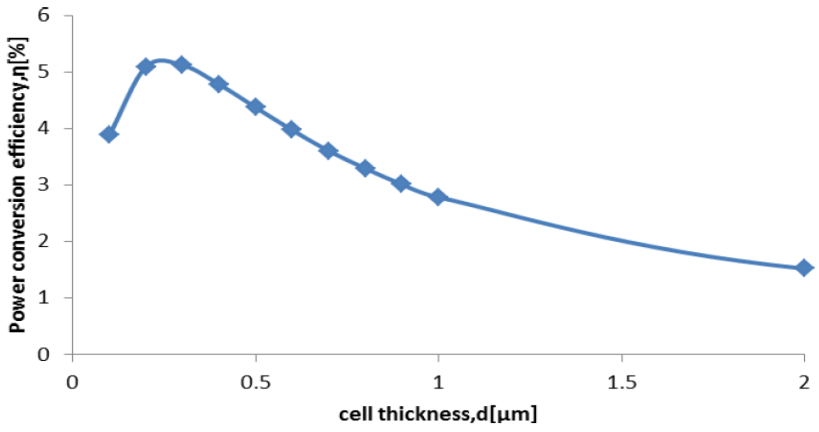

Figure 3-12. Effect of cell thickness on the PCE of the polymer: fullerene BHJ OSC. Reproduced from ref. [59].

4. METAL NANOPARTICLES: PROPERTIES AND APPLICATION IN ORGANIC SOLAR CELLS

4.1 Plasmonic Effect

The collective oscillations of conduction electrons stimulated by the electromagnetic field (EM) of incident light is identified as surface plasmon resonance (SPR). The phenomenon is only observed in nanoscale metallic particles in which the electrons are confined in three dimensions. Due to this effect, an electric field is induced around nanoparticles (NPs) which could be larger than that of the incident light by orders of magnitude. SPR is a nanoscaled-size effect; that is, the bulk metal particles do not possess such properties. In the case of MNPs, the electrons are confined in three dimensions, which results in LSPR. Nanowires, nanotubes and nanofilms could also exhibit SPs. In consequence of their large dimensions compared to the light wavelength; however, the induced EM field propagates along the interface of the metal and dielectric medium instead of being localized [60].

Recent researches proved that SPs have the potential for a broad range of beneficial applications in diverse areas such as drug delivery [61], PV cells [62], sensing [63], superlenzing [64], cancer diagnosis and therapy [65], light emitting devices [66]. Due to the diverse practical applications of MNPs, their various synthesis techniques and unique properties have been investigated [67, 68].

In 1908, Gustav Mie came up with a rigorous theoretical treatment to explain the optical properties of metallic colloids [69]. Although this was the beginning point to investigate the SPs

scientifically, the evidences from ancient civilizations show the use of MNPs as of centuries ago. The most well-known example is a Roman glass cage cup, named Lycurgus cup, which looks green or red while the light is illuminating from outside or inside, respectively (Figure 4-1). The reason behind is the presence of MNPs in the glass [70].

Figure 4-1. The green Lycurgus cup, while light is illuminating from outside, turns to red when light is shone from inside. The glass contains tiny amount of MNPs which give it this unusual optical characteristic.

In scientific point of view, a lattice of ionic cores along with the free conductive band electrons, could be a useful description for a MNP [71]. The dissimilar charges are separated towards the surface upon the incident of EM field of light. Hence, an electric dipole would be generated due to the accumulation of opposite charges in different sides of the surface. The internal created electric field by this dipole would resist to EM field of the incident light. Moreover, the external light field will force the accumulated charges to return back to their initial position [72, 73] (Figure 4-2). This could be simulated by a simple linear oscillator in which there is a force to return the situation to equilibrium.

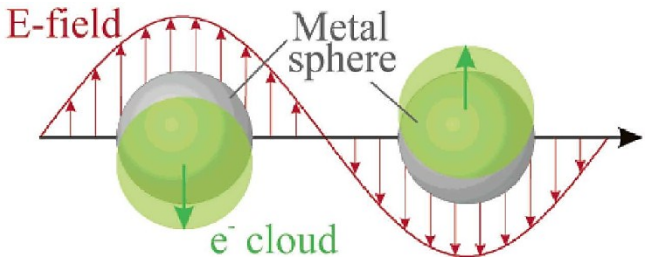

Figure 4-2. Interaction between the electromagnetic field of incident light with metallic nanoparticles results in the creation of a dipole. Reproduced from ref. [67].

The plasmonic frequency is defined as a frequency at which electrons will keep oscillating after removing the external field. A resonance occurs while an external force with frequency equal to the plasmonic frequency applies to the MNPs. The alternating applied frequency defines the frequency by which the electrons oscillate; however, the amplitude and phase depend on both internal and external forces. The illuminated light provides the kinetic and electrostatic energy of the oscillating electrons associated with the electric fields of the dipole. Excitation requires more energy due to larger oscillations. In other words, more light quenches at the time of resonating SPs inside the MNPs. Consequently, the peaks in the absorption spectrum of MNPs correspond to the excitation of SPs. The absorbed light brings the electrons to their excited states [74].

The efficiency of an MNP depends on its scattering and absorbing properties [75]. The absorption/scattering efficiency of an MNP is proportional to its absorption/ scattering cross sections; the area in which all incident photons are absorbed/scattered. The extinction cross section is the sum of these two areas; the geometrical section of the particle where all photons are removed from the incident light by either absorbing or scattering.

In general, the extinction cross section of noble MNPs exceeds their geometrical sections. This could be enhanced by up to 10 times [76]. Larger extinction cross sections represent higher efficiency of MNPs in terms of absorbing and scattering the illuminated light. MNPs owe this

unique characteristic to SPR effect; that is, the excitation of SPs results in concentration of incident light by NPs to induce an intensified extinction cross section. However, the relation between the light absorption intensity and absorption cross section is exponential. In other words, a small increase in the absorption cross section leads to a huge enhancement of the absorption efficiency [71].

SPR effect and in turn the optical properties of MNPs dramatically depend on the particle geometry and the surrounding medium [77].

4.1.1 The effect of particle geometry and surrounding medium

The properties of metal nanoscaled-size particles could be divided into two regions based on their sizes; nanoparticles with radius smaller than 50 nm, known as “quasi-static” regime, and the ones with sizes comparable to the light wavelength [78]. The performance of small size particles could be successfully explained by a dielectric dipole. In this case, the width and intensity of the resonance band are determined by the size dependency of the SPR effect. However, the impact on resonance wavelength is negligible [79]. As it is shown in Figure 4-3-a, the resonance absorption intensity of silver nanoparticles (Ag NPs) with different sizes embedded in silica (n=1.5) is significantly affected; larger radius particles represent higher intensities. As it was expected, there is no remarkable alteration in the wavelength region which proves the independency of resonance wavelength from size effect. The size-dependency of MNPs optical properties has been investigated extensively in the literature [71, 77, 80].

According to Figure 4-3-b, for particles smaller than 5 nm, there is a linear relationship between the full-width-at-half-maximum (FWHM) of the SP resonance band and the inverse of particle radius.

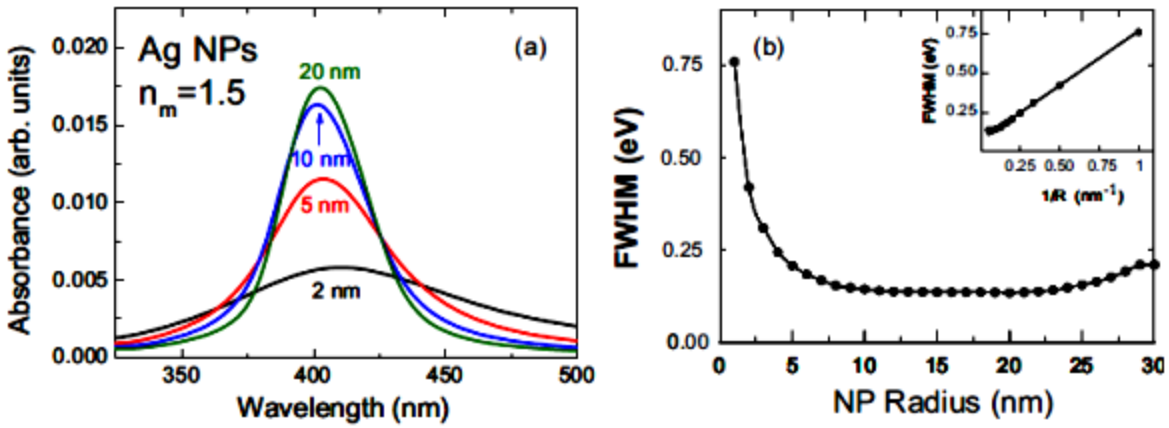

Figure 4-3. (a) Calculated optical absorption spectrum for Ag NPs with different sizes, (b) the relationship between FWHM and the particle radius; the inset represents a linear correspondence between FWHM and the inverse of the radius. Reproduced from ref. [71].

On the other hand, a dipole is not accurate enough to describe the optical behavior of large particles which have radius sizes comparable to the light wavelength. Consequently, the several peaks of resonance band should be explained by multipolar terms like quadrupole for two peaks. A detailed dipole and quadrupole behavior of MNPs can be found elsewhere [81].

Particles with further large radius show thoroughly different characteristics, which could not be explained by multipolar terms. In this case, the excitation of SPs is related to the propagating EM waves at the interface of metal and dielectric medium, which is kind of different phenomenon.

The other parameter which noticeably affects the resonance of SPs is the shape of MNPs. The resonance wavelength could be adjusted based on the required wavelength for any specific application by proper selection of MNPs shape [82, 83, 84].

As mentioned before, the accumulated charges on the surface of MNPs are impelled to return back to their equilibrium position by a restoring force. This results in the dependency of this force on the shape of MNPs.

One of the most well-known shapes that exhibits the effect of particle geometry on optical properties is nanorod [71, 85, 86].

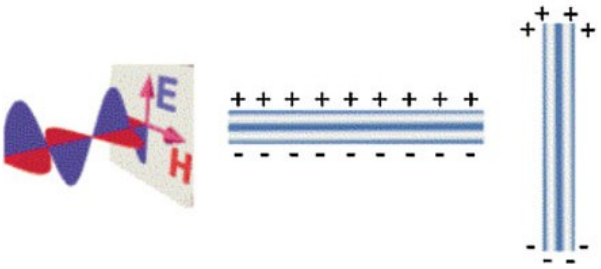

Figure 4-4. Transverse and longitudinal oscillations of conduction band electrons of a metal nanorod due to the interaction with the electromagnetic field of incident light. Reproduced from ref. [87].

Figure 4-4 illustrates the difference between the oscillation of electrons along the rod axis and perpendicular to that. Maximum charge accumulation is observed while the electrons oscillate normal to the rod axis, these oscillations correspond to the transversal plasmons.

On the other hand, charge oscillation parallel to the rod axis, namely longitudinal plasmons, represent the minimum charge accumulation at two ends of the nanorod. Less agglomeration of charges in the latter case induces a smaller restoring force. That is, the resonant frequency for longitudinal plasmons would be smaller and in turn the resonance wavelength goes more towards the near infrared (NIR) wavelength region. Moreover, considerable number of collected dissimilar charges at two sides of a nanorod require more force and consequently results in higher frequencies. Therefore, the resonance wavelength associated with transversal plasmons would be

smaller than that of the longitudinal ones and it appears approximately within the same wavelength region as for the spherical nanoparticles. In conclusion, the most crucial factor is the aspect ratio which controls the absorption wavelength of MNPs [71].

Finally, the effect of surrounding medium on the optical behavior of MNPs is inevitable. The dielectric function of surrounding medium not only controls the geometry of the electric field around MNPs but also adjusts the resonance wavelength. More details could be found in the literature [88, 89].

It is worth noting that if MNPs are close enough to eachother, the resonant conditions resulted from each nanoparticle would be modified due to the local electric field of adjacent nanoparticles. Interparticles interactions usually red-shift the absorption wavelength and increase the FWHM [78, 90]

4.1.2 Silver nanoparticles

A spherical nanostructure with the diameter of around tens of nanometers or less is defined as a nanosphere. Ag NSs are one of the most common and famous noble MNPs which possess unique optical, electrical and magnetic properties. The range of its applications including implementations in optics, electronics, biomedicine and chemistry extends by technology development. So far, the beneficial properties of Ag NPs have been investigated in surface enhanced spectroscopy, surface plasmonic photovoltaics, printed electronics, sensors, antimicrobical coatings, food preservation, catalysts, polymers, LEDs, biomedical devices, sterile equipments and etc. [91].

The unique optical properties of Ag NSs such as high extinction efficiency come from LSPR and scattering effects. Figure 4-5, shows TEM images of Ag NSs with 20 nm, 60 nm and 100 nm, respectively.

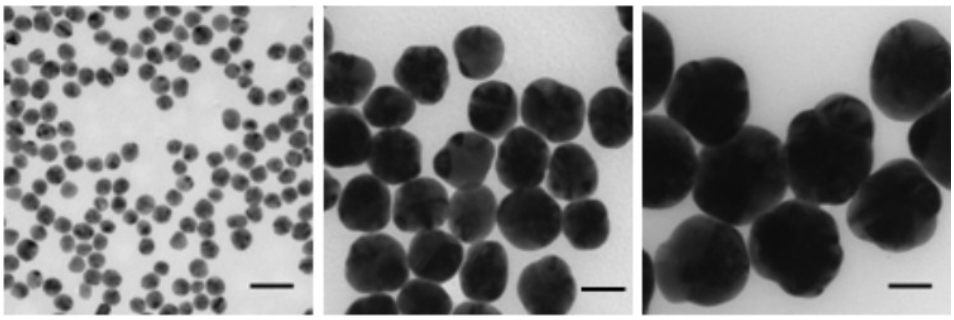

Figure 4-5. TEM of Ag NSs with 20 nm, 60 nm, and 100 nm radius. The scale bar is 50 nm. Reproduced from ref. [92].

The effect of nanoparticle size on optical density (OD) of Ag NPs is illustrated in Figure 4-6. As it has already been explained in this chapter, the optical characteristics of small nanoparticles with radius less than 50 nm could be described by a dielectric dipolar. In this range, the width and the intensity of the resonance band is more affected by the size alteration rather than the absorbance wavelength. For larger Ag NSs, the optical behavior could be explained by a dielectric quadrupole. As the diameter increases, the plasmon resonance peak shifts towards longer wavelengths (known as red-shifting) and it also broadens more noticeably.

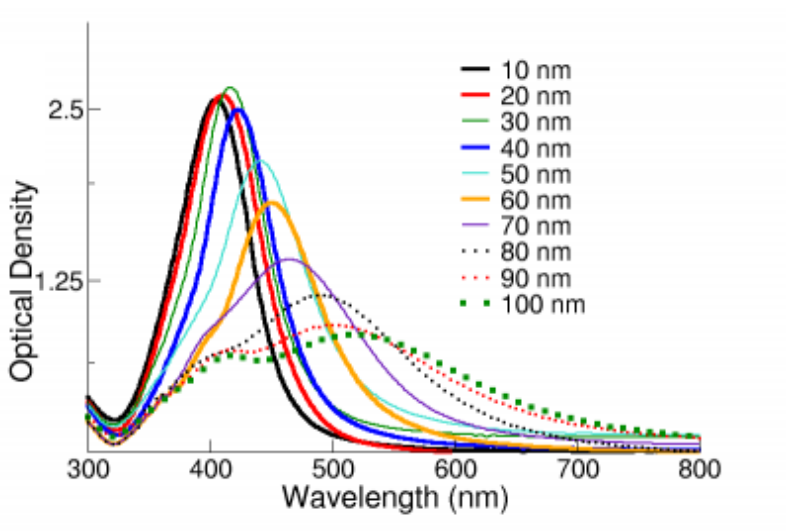

Figure 4-6. Size-dependent extinction spectra for Ag NSs with various diameters ranging from 10 nm to 100 nm. Reproduced from ref. [93].

The effect of surrounding medium on the optical properties of Ag NSs is shown in Figure 4-7. ***n*** stands for the refractive index of a material in which Ag NPs are incorporated. By increasing the refractive index of the surrounding medium, for a 50 nm Ag NSs, the exctinction peak shifts towards longer wavelengths and the extinction cross section also intensifies.

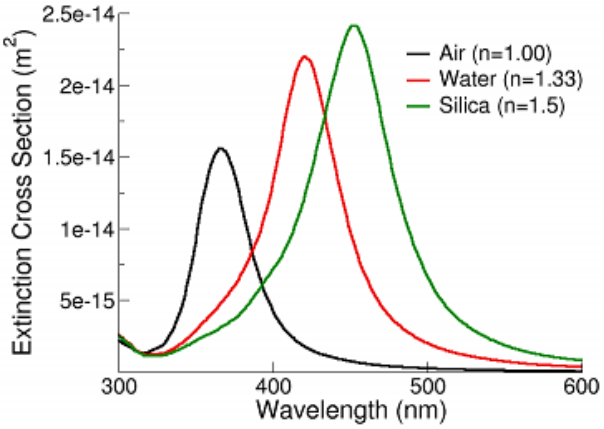

Figure 4-7. Relationship between extinction spectra of 50 nm Ag NSs embedded in air, water and silica. As refractive index of the surrounding medium increasing the extinction spectrum red-shifts. Reproduced from ref. [93].

The enhancement of local electric field supported by LSPR for an Ag NS in the air is shown in Figure 4-8-a schematically and in Figure 4-8-b by calculation.

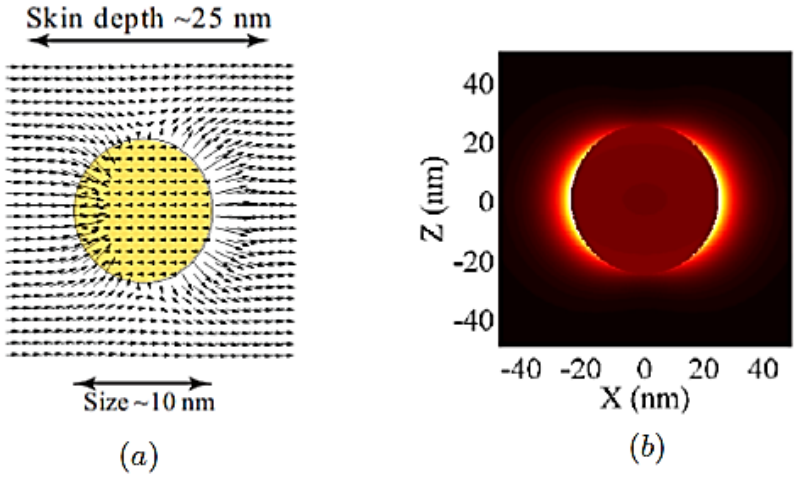

Figure 4-8. (a) Schematic and (b) Calculated representation of the near-field enhancement induced by LSPR effect for an Ag NS. (a) is reproduced from ref. [94] and (b) is reproduced from ref. [95].

4.1.3 Gold nanorods

The special shape of Au NRs provides it with unique optical, electrical and conductive properties [96] (Figure 4-9).

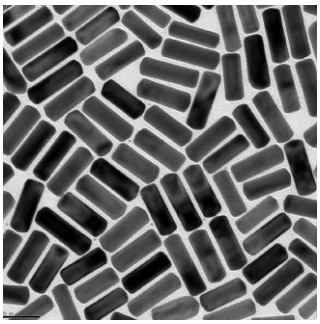

Figure 4-9. TEM image of 25 nm diameter Au NRs. Reproduced from ref. [97].

These outstanding characteristics give rise to the various applications in different fields such as catalysis, biomedical, biodiagnostics, high technology electronics, environmental and energy fields.

Despite the spherical gold nanostructures, in which the maximum extinction peak could be observed at around 580 nm, the tunable aspect ratio of Au NRs broadens the extinction peak by up to 1400 nm.

Figure 4-10 shows the effect of aspect ratio on the absorption spectra and color of Au NRs. The absorption peak appears at 524 nm for a nanosphere, while by increasing the aspect ratio up to the four times of its initial value, the longitudinal plasmon resonance peak shifts to 704 nm.

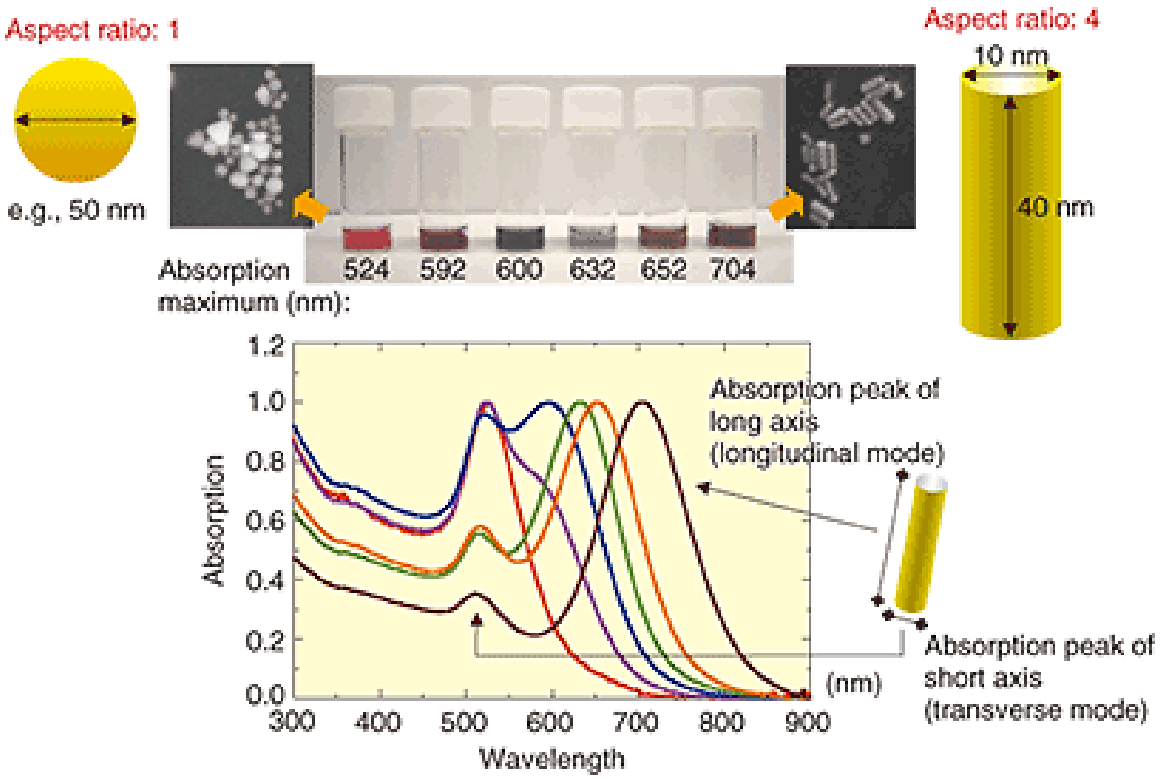

Figure 4-10. Influence of the aspect ratio on the absorption spectra and color of Au NRs. Reproduced from ref. [98].

The effect of surrounding medium on optical properties of Au NRs is investigated by incorporation of an Au NRs in various solvents. Figure 4-11 shows the linear relation between the refractive index and longitudinal plasmon band position. Moreover, increasing the refractive index leads to a better absorbance and broader band width.

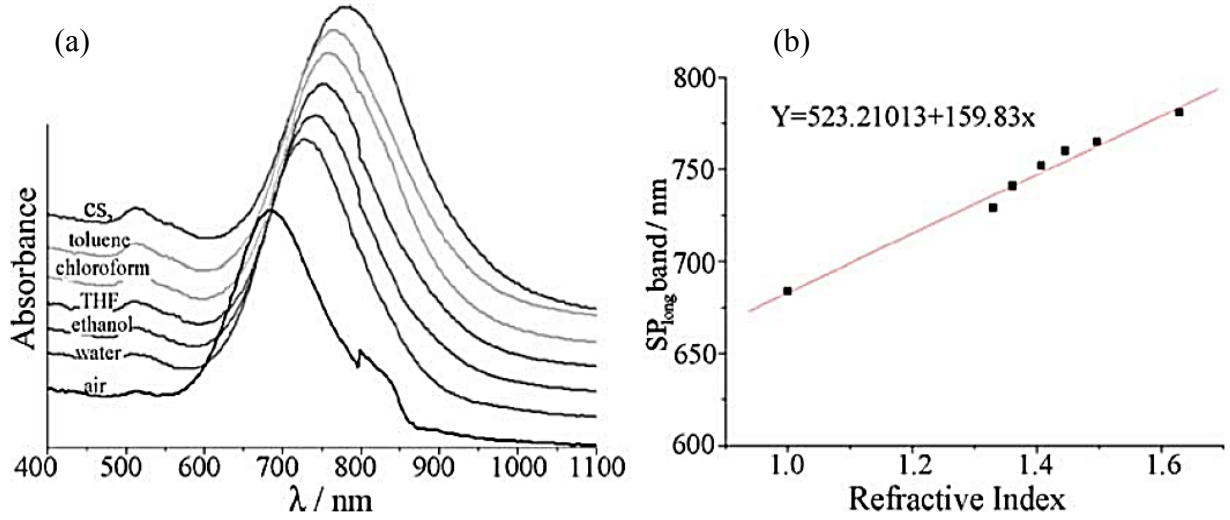

Figure 4-11. (a) Effect of surrounding medium on the absorbance spectra of Au NRs embedded in different solvents. (b) Alteration in the longitudinal plasmon band position associated with different refractive indexes. Reproduced from ref. [96].

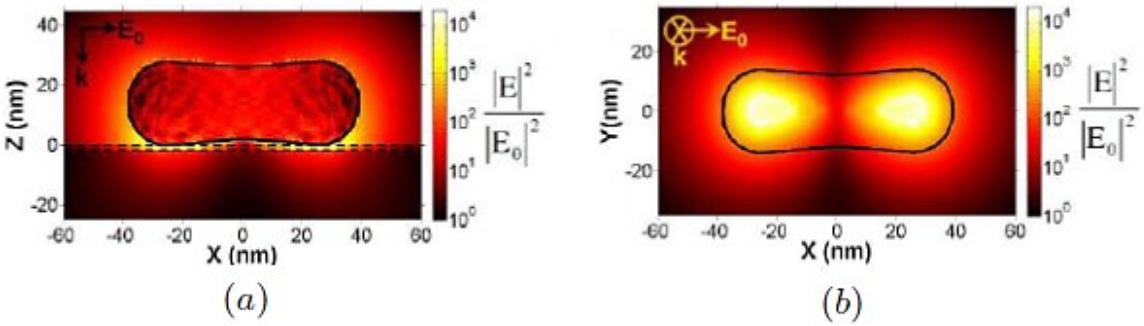

Figure 4-12. Calculated local electric field enhancement in the vicinity of an Au NR with a diameter of 28 nm deposited on the silicon substrate. The polarization of incident light is along the rod axis with a wavelength of λ= 780 nm. Image shows the enhancement (a) in the central cross-section of the rod and (b) in the top layer of the substrate. Reproduced from ref. [99].

Regarding the LSPR effect, the calculated image of a near-field enhancement close to the surface of a 28 nm diameter gold nanorod is depicted in Figure 4-12. The incident light has a polarization parallel to the rod axis (77 nm) and a wavelength of λ= 780 nm. The magnitude of the enhanced electric-field is indicated by the color scale [99].

4.2 Plasmonics Organic Solar Cells

The enhanced extinction cross section of MNPs upon the light illumination makes them an appropriate option for increasing the light harvesting inside an SC. If the medium in which the MNPs are incorporated is homogenous, the forward and backward scattering could occur with equal probabilities. However, while the MNPs are deposited close to the interface of two dielectrics with different permittivity, light would fold preferably to the dielectric with larger permittivity [62].

Scattering of light would increase the absorption due to the enhanced optical path length (Figure 4-13-a). On the other hand, excitation of LSPR leads to the optical electric field concentration (Figure 4-13-b). If a semiconductor is close enough to this enhanced-field, the absorption would locally increase due to the high density of states of the photons [100]. Photon absorption enhancement results in either more exciton generation or dissociation and in turn improves the photocurrent of the SC.

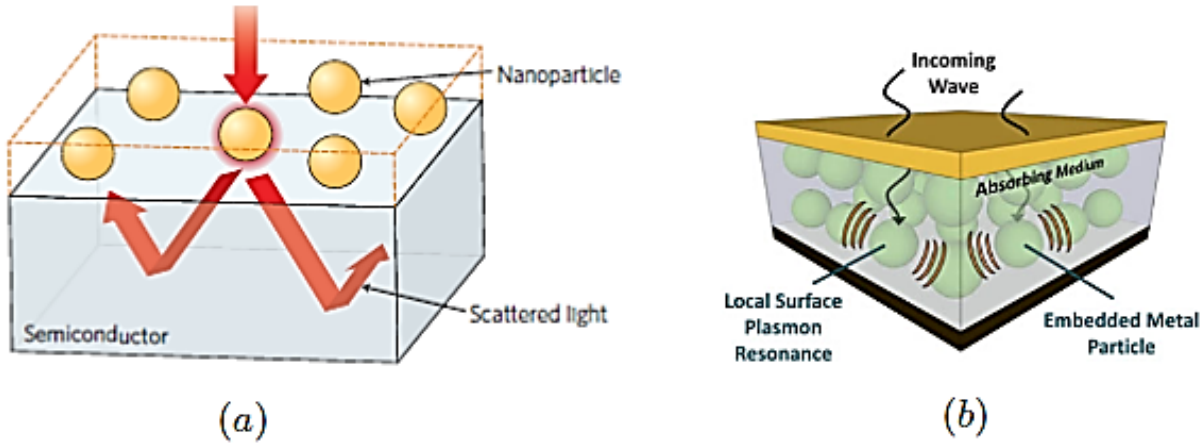

Figure 4-13. (a) Light scattering inside the photoactive material by means of MNPs. This effect intensifies the optical path length and in turn increases the light harvesting. Reproduced from ref. [101], (b) Optical electric field concentration induced by LSPR. Reproduced from ref. [102].

The main performance improvement of Si-based inorganic SCs by MNPs incorporation mainly comes from the scattering effect which reduces the reflection and increases the light-trapping capability of the device [103].

The performance of plasmon-enhanced OSCs has been studied widely using various deposition techniques for incorporation of different kinds, sizes and shapes of MNPs within diverse layers of the device structure [21, 104, 105, 106]. An organized overview could be prepared by categorizing the previous studies according to the layer in which MNPs are embedded including buffer layer, photoactive material, front and back electrodes.

Hwang Lee et al. reported a layer-by-layer deposition of Au NRs directly on the ITO electrode which is thermally transferred to nanodots in P3HT:PCBM bulk heterojunction device. An increase in PCE from 3.05% to 3.69% is explained according to the strong coupling between the organic excitons and plasmons of the gold nanodots [17].

The performance of P3HT:PCBM bulk heterojunction device with incorporation of low density Au NRs on the ITO electrode is investigated through various deposition techniques including spin-casting, drop-casting and vertical deposition. PCE for the latter case enhanced up to 18% due to an improvement in the photo-generation of excitons. The enhanced near-field in the vicinity of nanoparticles also gives rise to the short circuit current density of the device by up to 16% [20].

The fabrication of silver nanoparticles on ITO using vapor-phase deposition technique increased PCE of P3HT:PCBM device from 1.3% to 2.2% for thin plasmon-active layer. The better performance achieved due to the intensified electric field inside the absorbing organic material owing to LSPR effect of deposited Ag NPs [107].

In another study, uniform-sized Ag NPs with 13 nm diameter are electrodeposited on the ITO modified electrode, which results in an enhancement of PCE from 3.05% to 3.69%. This improvement comes from an intensified photogenerated current density which corresponds to the enhanced absorption in photoactive material [19].

A deposition of a self-assembled monolayer of 4 nm silver nanoparticles between PEDOT:PSS and photoactive layer of polymer:fullerene SC results in higher short circuit current densities compared to the reference devices. However, a dramatic decrease in V_{OC} and FF is observed. This suggests that although exciton generation is increased due to the LSPR effect, Ag NPs enhance the surface recombination at the interface of the buffer layer and P3HT:PCBM [108].

The beneficial effects in photocurrent and device efficiency from the plasmon resonance of MNPs embeddedd in the buffer layer of an OSC have also been reported. A blend of Au NRs with buffer layer of P3HT:PCBM bulk heterojunction device represented a noticeable enlargement in PCE and J_{SC} up to 21.3% and 13%, respectively. The localized transverse and

longitudinal plasmon resonance modes are reported as the origin for the enhancement of device performance [109].

Improvements of both FF and photocurrent due to the LSPR effect of blended Au NPs in the hole conducting buffer layer is reported by Jyh-Lih et al. Owing to the enhanced local electric field, strong coupling between surface plasmons and excitons occurred, which facilitated charge transform. PCE of the modified device is increased from 3.57% to 4.24% due to the enhancement of exciton generation and dissociation [21].

Various concentrations of ~30-40 nm Au NPs are blended with the anodic buffer layer in a polymer:fullerene BHJ device. 20% increase in PCE (from 3.45% to 4.19%) reported using 20% Au NRs. The reason is an increase both in the rate of exciton generation and exciton dissociation owing to the LSPR effect [22].

The effect of Au NPs embedded in the BHJ material of polymer:fullerene SC is investigated by Park et al. V_{OC} and FF of the device remained the same. However, 50% PCE enhancement was achieved for nanoparticle–polymer composite film with the weight fraction of 6.25×10^{-8} for gold nanoparticle/P3HT. The enhanced light absorption is suggested as a main reason for both photocurrent and PCE increase [24].

5 wt% Au NPs with 70 nm diameter were blended into the photoactive materials of BHJ OSCs. After exploring various polymer:fullerene composites, an increase in PCE from 3.54% to 4.36% for P3HT/PC70BM, from 5.77% to 6.45% for PCDTBT/PC70BM and from 3.92% to 4.54% for Si-PCPDTBT/PC70BM is observed. The authors explained the overall improvement of the device performance by increased charge transportation and enhanced light absorption [25]. Plasmon-enhanced tandem SCs using MNPs in the interconnecting layer of the device has also been reported [18, 26].

5. DEVICE FABRICATION AND CHARACTERIZATION

Figure 5-1 shows the structure and fabrication process of a standard OSC. Etching of each ITO-coated glass sample results in 8 devices. Each reference device (without incorporation of MNPs) includes three main layers starting with ITO as a transparent positive anode, 0.16 cm^2 of the active area (P3HT:PCBM) sandwiched between two dissimilar buffer layers and ending with a layer of Aluminum (Al) as a negative metallic cathode [23].

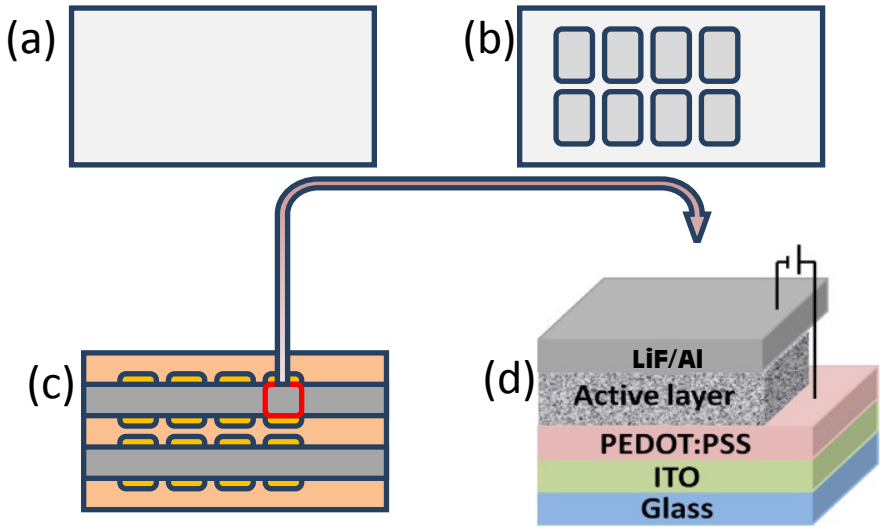

Figure 5-1. Fabrication process of a standard OSC starts with (a) cutting ITO-coated glass substrate, continues with (b) etching and (c-d) ends with incorporation of different appropriate materials with various deposition techniques on top of the patterned ITO. Consequently, the final structure of ITO/PEDOT:PSS/P3HT:PCBM/LiF/Al would be achieved.

In order to fabricate P3HT:PCBM bulk heterojunction SCs, some materials were required as listed below: Poly(3,4-ethylenedioxythiophene) poly(styrenesulfonate) (PEDOT:PSS) (CLEVIOS™ P VP AI 4083) was purchased from HC Stark. Al wire and Lithium Fluoride (LiF) were purchased from Alfa Aesar. High regioregularity (98%) poly(3-hexylthiophene-2,5-diyl) P3HT with average molecular weight of <50,000 MW was purchased from Rieke Metals. [6,6]-phenyl-C_{61}-butyric acid methyl ester (PCBM) (>99.5%) and 1, 2-dichlorobenzene (anhydrous, 99%) were purchased from Sigma- Aldrich. S1811 positive photoresist with material no 10018337 and MF-319 developer with material no 10018042 both were purchased from ROHM and HAAS electronic materials. The materials were used as received without further purification.

Moreover, Ag NSs and Au NRs were also purchased from Sigma-Aldrich to investigate the performance of MNPs- incorporated OSCs.

The colloidal Ag NSs in the aqueous buffer possess a particle concentration of 5.4E+10 particles/mL and a mass concentration of 0.021 mg/mL, and it contains sodium citrate as stabilizer. The average diameter of nanospheres is 40±4 nm which results in a plasmon resonance peak at 412 nm. The size distribution of Ag NSs solution and the TEM are shown in Figure 5-2-a and Figure 5-2-b, respectively. The images are provided by Sigma-Aldrich.

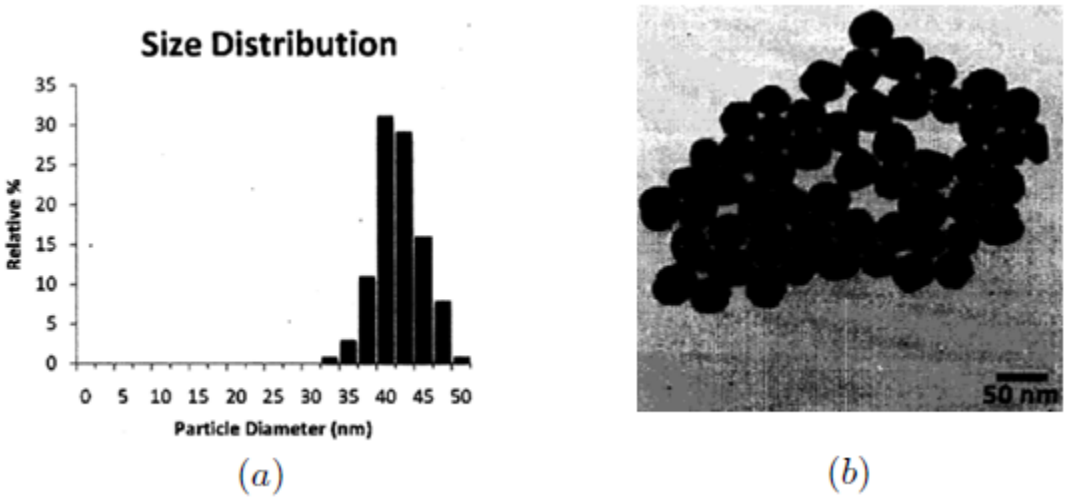

(a) (b)

Figure 5-2. (a) Size distribution and (b) TEM of 40 nm radius Ag NSs. Images are provided by Sigma-Aldrich.

The colloidal Au NRs in the aqueous buffer possess a particle concentration of 8.5E+10 particles/mL and a mass concentration of 0.135 mg/mL, and it contains CTAB as stabilizer. The average diameter of 25 nm and a length of 60 nm (+/- 10%) results in a transverse and longitudinal plasmon resonance peak at 520 nm and 650 nm, respectively. Figure 5-3 represents TEM image of Au NRs.

Figure 5-3. TEM of 25×60 nm^2 Au NRs. Image is provided by Sigma-Adrich.

All devices were fabricated and characterized respecting an identical batch processing.

In each set of experiment, 4 samples were synthesized and characterized. The control sample was fabricated without any nanoparticles incorporation. However, the ITO surface of second, third and fourth samples were incorporated with only Ag NSs, only Au NRs, and the dual nanostructure of combined Ag NSs and Au NRs, respectively. The dual nanostructure was made by blending Ag NSs and Au NRs solutions with the ratio of 1:1.

The fabrication process starts with cutting ITO-coated glass into 2.6 cm × 3.7 cm slices using a diamond tip scriber and then continues with patterning the cutted samples through lithography. ITO is a transparent electrically conductive material that would act as the positive transparent anode of the final device.

The samples were cleaned with detergent and rinsed with deionized (DI) water. After ultrasonicating the samples with acetone, isopropanol and DI water for 20 minutes each, the substrates dried with a nitrogen flow and baked at 150 ºC for 20 minutes.

The light-sensitive material, named S1811 positive photoressist were then deposited on ITO at 4000rpm and a thin etching-resistant layer were achieved. Afterwards, the samples were baked at 120 ºC for 1 minute and they were then exposed to ultraviolet light using a mask aligner (OAI hybralign) in which a mask with a desired pattern, including dark and transparent areas, is already placed. Through the light illumination, the exposed layer becomes soluble in the developer. Therefore, the parts of the photoresist layer which were covered by the transparent area of the mask could be removed using a developer (for 1 minute). The samples were baked again at 130 ºC for 3 minutes. Afterwards, in order to remove the ITO which was not concealed under the photoresist material any more, the samples were diped in hydrochloric acid (HCL) for 8 minutes.

Finally, the remaining photoresist layer on top of the patterned ITO was removed using acetone for 2 minutes.

The patterned sample, including 8 devices, was cleaned again by repeating all steps of cleaning process. After baking the substrates for 20 minutes at 150 ºC, they were subjected to an oxygen plasma treatment inside a lab-made plasma asher for 40s. As it is reported [110], the O_2 plasma treatment not only removes the impurities of ITO surface but also enhances its surface energy to match the water-based PEDOT:PSS solution. Therefore, the O_2 plasma treatment could have a noticeable positive effect on the performance of the device. The reference device (without MNPs) fabrication would be followed by PEDOT:PSS deposition. However, for the devices incorporated with MNPs (denoted herein as the "plasmonic device"), the water-based nanoparticles solutions would be spin-coated directly on top of the ITO after oxygen plasma treatment. Spin-coating for all plasmonic devices, including the ones with only Au NRs, only Ag NSs and the combined Ag NSs and Au NRs was performed in two steps, 200 rpm for 3sec and 1000 rpm for 10 sec. The schematic structure of dual metallic nanostructure (Au NRs plus Ag NSs) OSCs is shown in Figure 5-4.

Before deposition on top of the samples, the hole conducting PEDOT:PSS material was passed through a 0.45 μm PVDF membrane filter and then spin-coated at 4000 rpm to achieve a buffer layer of ~35 nm thickness. In all steps of our experiments, the thickness of various materials was measured using a mechanical profilometer (Veeco Dektak150). Incorporating a thin layer of hole conducting PEDOT:PSS stabilizes the electrical contact between ITO and organic active layer by modifying the surface roughness of the substrate [15].

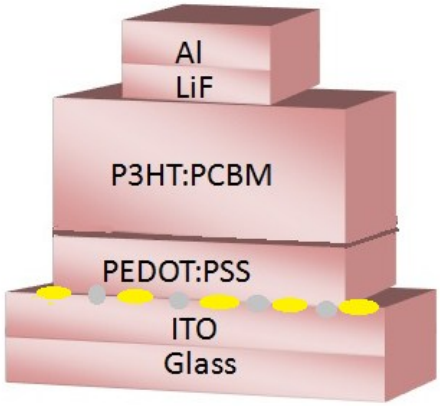

Figure 5-4. Schematic structure of dually incorporated OSC by the combined nanostructure of Au NRs and Ag NSs on top of the ITO-coated glass substrate. The yellow ellipsoids and gray spheres respresent Au NRs and Ag NSs, respectively. The device structure respects the following sequence: ITO/Au NRs+Ag NSs/ PEDOT:PSS/P3HT:PCBM/LiF/Al.

In order to dry the film, the substrates were baked at 140ºC for 10 min. Afterwards, they were transferred to a nitrogen glove box with a pressure of 3 mbar and humidity level less than 0.1 ppm for deposition of the polymer BHJ active layer. The active layer material is a mixture of PCBM as the electron acceptor and P3HT as the donor material.

In order to prepare the active layer blend, first P3HT and PCBM were accurately weighted with a ratio of 1:0.8 (polymer:fullerene). They were then dissolved separately in 1, 2-dichlorobenzene with a concentration of 20 mg/ml (P3HT) and 16 mg/ml (PCBM). The solutions were stirred and baked at 60 ºC for 1 hour. Afterwards, they were mixed with the ratio of 1:1 and then stirred and baked for 14 hours at 40 ºC. The blended solution was passed through a 0.45 µm PTFE membrane filter prior to the deposition process. This eliminated undesirable particles from the solution. Subsequently, the P3HT:PCBM active material spin-coated at 1000 rpm on top of the

ITO/PEDOT:PSS substrate to achieve an active layer of ~150 nm thickness. The deposited mixture instinctively separated into interpenetrated domains which results in an BHJ material [37]. The substrates were then left to dry in covered Petri dishes inside the glove box for 30 minutes before the evaporation of the cathode.

The final step to achieve the complete device is the evaporation of a bilayer LiF/Al cathode. The thermal evaporation was done inside the evaporator using a shadow mask. Once the pressure reaches the desired value of typically less than 10^{-6} torr, LiF can be evaporated at the rate of ~1-2 A/s. The same process was repeated in order to evaporate Al at the rate of ~2.5-5 A/s. The measured thicknesses of the LiF and Al layers were ~1 nm and ~90 nm, respectively. The devices were transferred to the glove box to apply a post-production annealing which is reported as a functional treatment to enhance the device performance. This treatment increases the crystallinity of P3HT and improves the nanoscale morphology of the material [111]. Using a digital hot plate, the devices were baked at 110 ºC for 20 minutes, and then they were left to cool-down and used for measurements.

Since these devices are subject to degradation, which occurs due to the oxygen and water exposure from the atmosphere, it is advised to characterize them right after fabrication. The principal degradation area is at the interface of the Al cathode and P3HT:PCBM. Besides the direct photooxidation of the polymer as one of the degradation reasons, a photochemical reduce of the organic components by Al is of great importance [15].

Immediately after fabrication, current-voltage characteristics were measured under ambient conditions without any device encapsulation. The devices were exposed to a solar simulator made of Xenon lamp (Oriel instruments) which was equipped with AM 1.5G filter. The light intensity of the lamp was precisely calibrated by a light meter (LI-250 Bioscience) using a color filtered

silicon photodiode (LI-200 Pyranometer) at 100 mW/cm^2. The measurements were executed by a semiconductor characterization system (Keithley 2400). PV parameters such as J_{SC}, V_{OC}, FF, PCE, and R_S were extracted and calculated from the J-V characterization results.

For exploring the effects of MNPs incorporation on the absorption spectra of the active layer material, the optical absorption for samples with and without NPs were measured and compared using a UV-Vis spectrophotometer (PerkinElmer LAMBDA 650 spectrophotometer). In order to prepare the samples for this experiment, the ITO-coated glass substrates were cleaned, ultrasonicated, and heated as described earlier. After oxygen plasma treatment, three samples were spin-coated with only Ag NSs, only Au NRs and combined nanostructure of Au NRs plus Ag NSs, separately. The samples were then transferred to the glove box to deposit the P3HT:PCBM material which has already prepared and passed through the appropriate filter. All the spin-coating parameters were identical with the ones utilized for device fabrication. The measurements were carried out after leaving the samples for 30 minutes in covered Petri dishes in order to dry.

Moreover, the surface structure of MNPs-deposited ITO was characterized using a scanning electron microscopy (FEG-SEM Hitachi S-4700).

6. RESULTS AND DISCUSSION

The absorption spectra of pristine P3HT:PCBM is provided along with the solar irradiation spectrum in Figure 6-1. The main absorption regime of photoactive material is situated within the visible regime. However, the amount of absorbed light could be increased not only within the visible area but also in NIR and IR domain where a considerable amount of incident light exists.

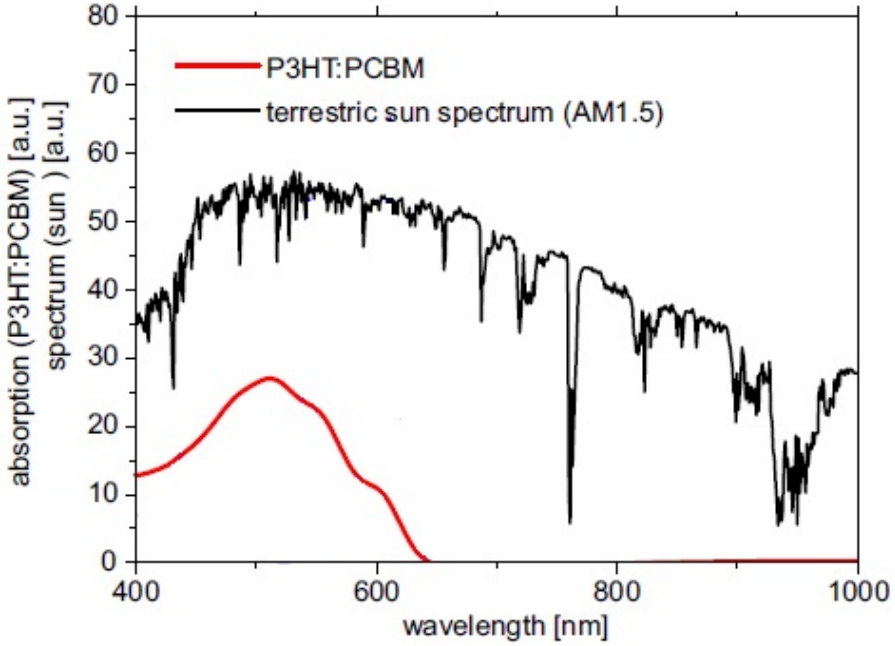

Figure 6-1. Comparison between the absorption spectrum of P3HT:PCBM and the AM1.5 spectrum of the sun. Reproduced from ref. [112].

In this study, P3HT:PCBM system was chosen due to its photoactive efficiency, availability of the materials as well as its ease of fabrication.

6.1 Silver Nanospheres-Incorporated OSCs

The resonance peak of Ag NSs with average diameter of 40±4 nm and 0.02 mg/ml mass concentration in aqueous solution is observed at the wavelength of 412 nm. The size of NPs is selected intentionally in order to increase the absorption of the active material in this particular range. The Ag NSs incorporated-devices could absorb the incident light around 400 nm wavelength where the solar irradiation is not absorbed efficiently by the pristine polymer:fullerene active layer. On the other hand, in order to extend the absorption spectrum of P3HT:PCBM towards the NIR regime, Au NRs would be an appropriate choice, which will be discussed with more details in the next section of this chapter.

Figure 6-2 shows the normalized absorption spectra of P3HT:PCBM and Ag NSs. The absorption spectrum of photoactive material ranges from 400 nm to 650 nm including a major peak at 518 nm and two minor ones at 558 nm and 608 nm. For Ag-NSs solution, the absorption peak observed at 412 nm.

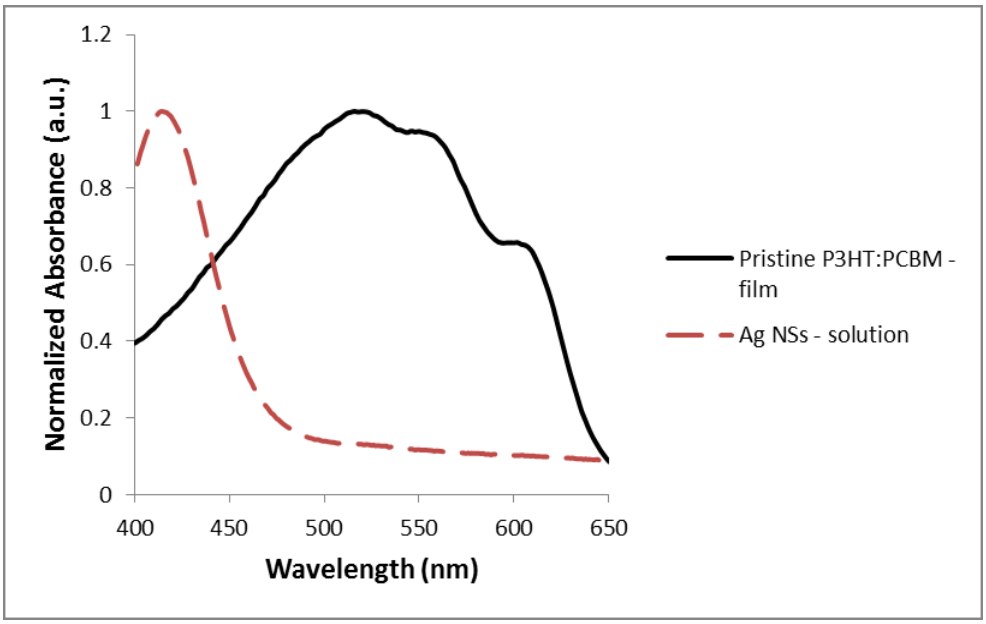

Figure 6-2. Comparison between absorption profiles of P3HT:PCBM film and Ag NSs solution.

SEM micrographs of Ag NSs deposited on ITO substrate are showed in Figure 6-3. The light gray spheres on the dark gray background (ITO surface) are identified as the Ag NSs. SEM pictures show uniformly distributed NPs without any noticeable aggregations. The estimated density is around 6×10^{8} NPs/cm^{2} which is a very low density.

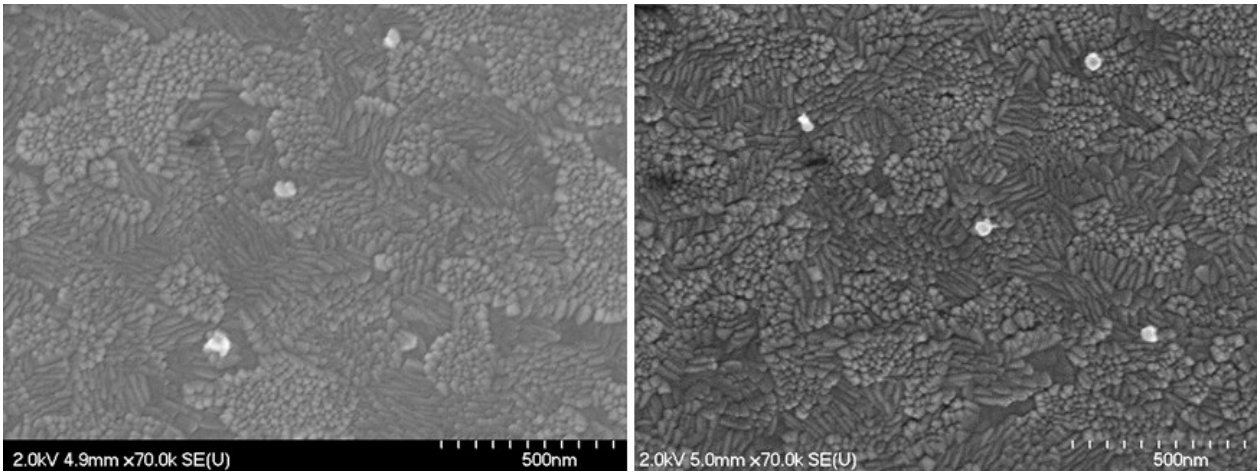

Figure 6-3. SEM micrographs of Ag NSs deposited on ITO substrate. The light gray spheres represent Ag NSs.

As mentioned before, the reference and plasmonic devices have the structure of ITO/ PEDOT:PSS/ P3HT:PCBM/ LiF/ Al and ITO/ Ag NSs/ PEDOT:PSS/ P3HT:PCBM/ LiF/ Al, respectively.

Figure 6-4 shows the J-V curves under illumination and in the dark conditions for both reference and plasmonic devices. The provided insets illustrate the semi-log graphs. In this study, the obtained values for PV parameters are generally low due to the both thin active layer with a thickness of around 150 nm and exposure of the devices to the air at some points of the fabrication and characterization processes. The performance is expected to be improved when working at controlled atmosphere.

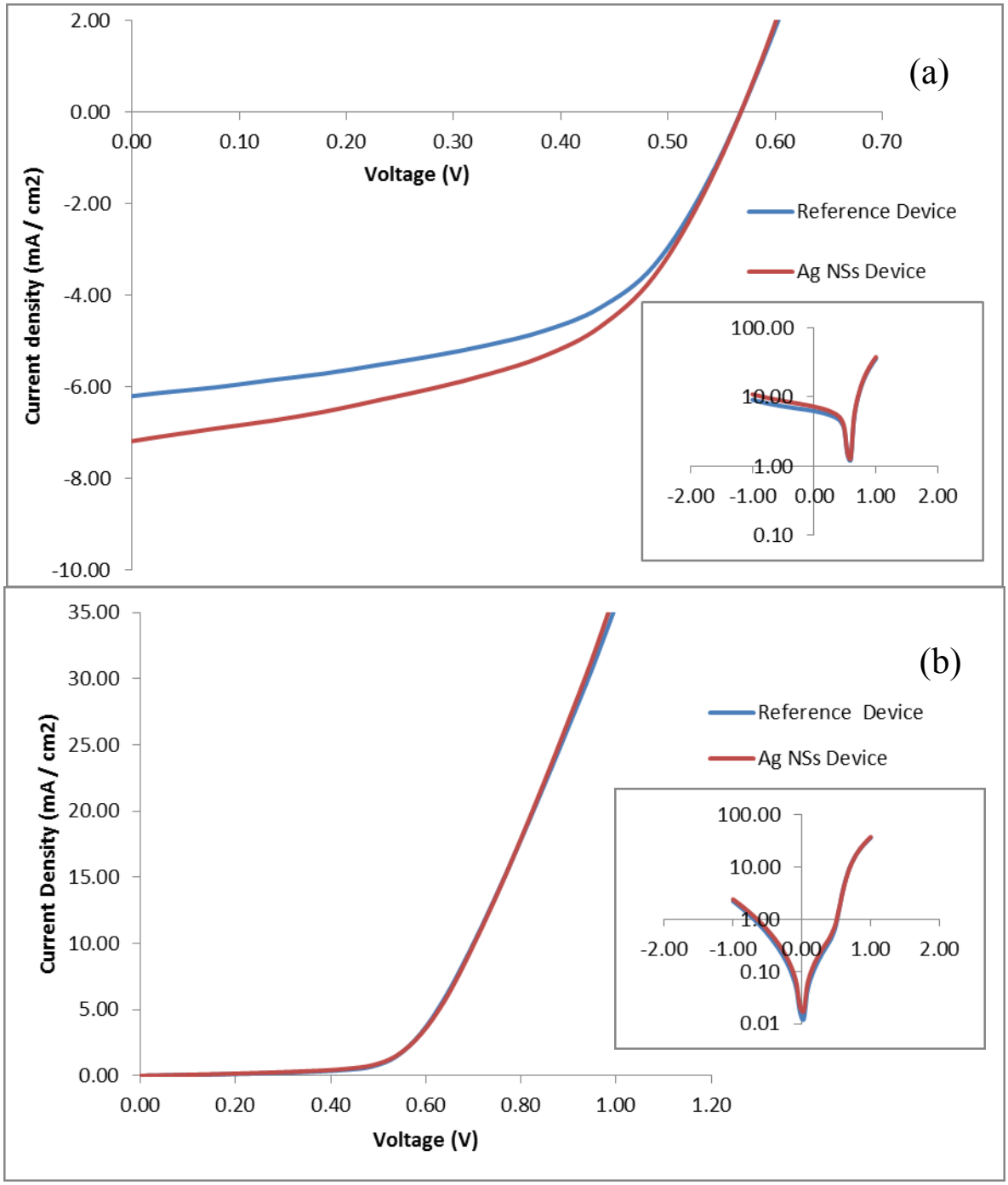

Figure 6-4. J-V characteristics of reference and plasmonic (with Ag NSs) devices (a) under illumination and (b) in the dark. The insets illustrate the semi-log graphs.

PV parameters are summarized in Table 6-1 along with their associated standard deviations. An enhanced optical and electrical performance was observed for plasmonic devices. PCE was found to increase from 1.86% to 2.07% which is a factor of 11.3% increase.

Furthermore, the measured J_{SC} for MNPs-incorporated and reference devices were 7.10 mA/cm^2 and 6.15 mA/cm^2, respectively. The series resistance (Rs) was extracted from the slope of J-V curve in the dark condition at 0.8 V which showed a slight decrease from 12.15 Ω/cm^2 to 11.73 Ω/cm^2. Moreover, the V_{OC} and FF remained almost the same.

Table 6-1. Average values for PV parameters for reference and Ag NSs devices along with their corresponding standard deviations. Rs is extracted from the slope of J-V curve in the dark condition at 0.8 V.

Device type	$Voc\,(V)$	Jsc (mA/cm^2)	Rs (Ω/cm^2)	FF (%)	PCE (%)
Reference - without MNPs	0.56	-6.15 ± 0.39	12.15 ± 2.54	54	1.86 ± 0.06
Ag NSs	0.56	-7.10 ± 0.52	11.73 ± 2.12	53	2.07 ± 0.07

The enhanced photogeneration of excitons due to the increase of the resonant field in the vicinity of Ag NSs could be the origin of an enhanced performance of the plasmonic devices. This would contribute directly to the photocurrent enhancement and in turn results in more efficient SCs.

An unchanged value of V_{OC} implies an unaltered nature of the electrode-organic interface [21]. Moreover, it could also be concluded that the charge-carrier recombination rates did not have a noticeable effect [113].

A significant decrease of V_{OC} is reported for devices in which the MNPs are in direct contact with P3HT:PCBM layer. This could be due to the higher surface recombination at the interface of the MNPs and the photoactive material. Therefore, this undesired effect could be reduced by deposition of MNPs directly on top of the ITO anode and covering them with a thin layer of PEDOT:PSS instead of blending them with the buffer layer [108].

The value of FF remained almost similar, however, the negligible reduction could be explained based on Ag NSs-induced surface morphology roughness which results in the surface recombination enhancement at the interface of the buffer and active layer [108].

In general, the mobility of the holes is less than that of the electrons in the polymer:fullerene active layer material. This means that the holes reach the interfaces slower than electrons. On the other hand, the enhanced local electric field in the vicinity of Ag NSs induced by LSPR would decrease exponentially with distance. Therefore, the holes close to the buffer and active layer interface could benefit from the enhanced electric field [114]. Moreover, the presence of Ag NSs facilitates the hole transportation via buffer layer due to the reduction of the interfaces which should be traveled by holes to reach the anode [25]. These could also explain the slight decrease of the series resistance for the Ag NSs-incorporated device compared to the reference device from 12.15 Ω/cm^2 to 11.73 Ω/cm^2.

In order to show that the LSPR was the main reason behind the improved performance of the plasmonic devices, we made a detailed study on the absorption spectra of P3HT:PCBM film with and without Ag NSs.

To make a comparison, the absorbance profile of pristine P3HT:PCBM deposited on ITO is represented by black solid line and that of the ITO/ Ag NSs/P3HT:PCBM is represented by a dashed red line in the same graph, the difference in the absorption spectra of these two films is

provided in a third curve, namely curve D, in which D stands for the difference (Figure 6-5). The absorbance intensity is clearly higher for the MNPs-integrated sample.

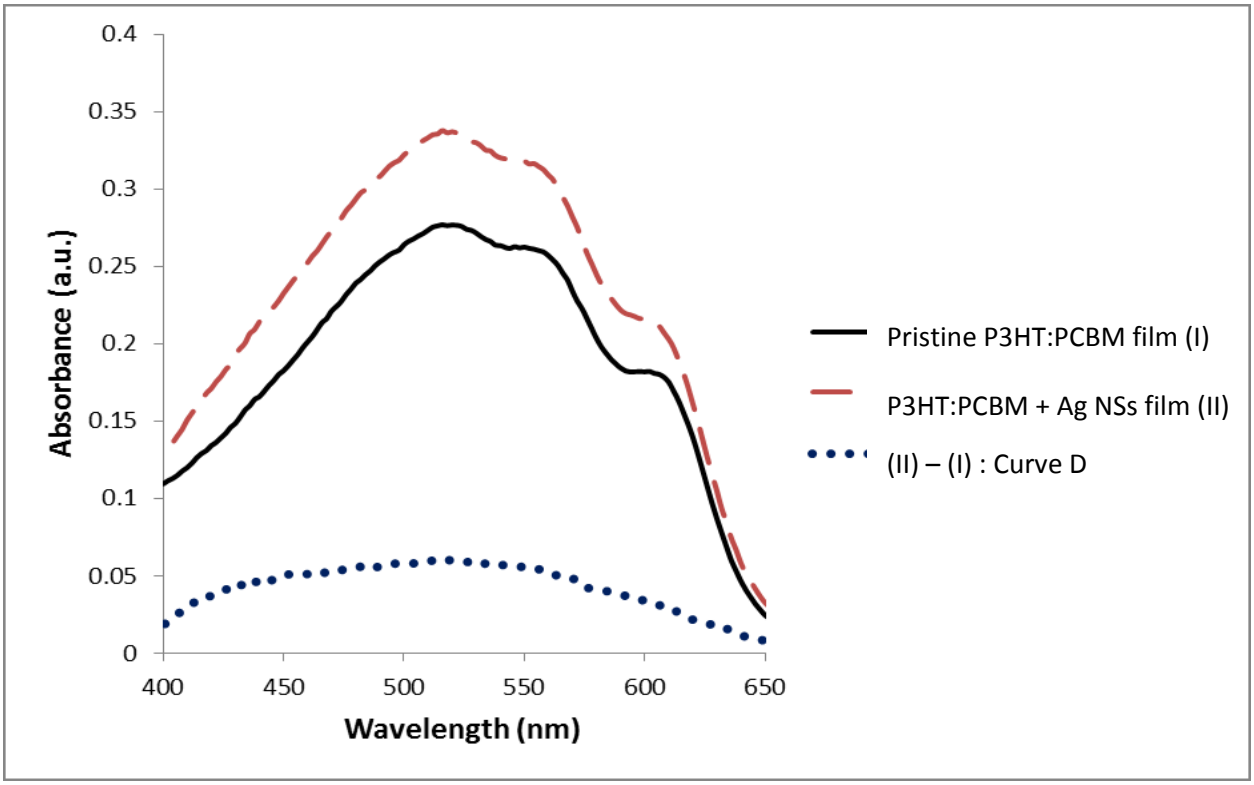

Figure 6-5. Comparison between absorption profile of pristine P3HT:PCBM film and Ag NSs-incorporated P3HT:PCBM film. Curve D illustrates the absorption enhancement of Ag NSs-integrated film compared to that of the pristine device.

Figure 6-6 illustrates the curve D alone which is useful in order to investigate the increased absorbance regime. A broad enhancement is observed from 400 nm to 650 nm. However, the most dominated regime are the wavelengths lower than 550 nm with a peak at 518 nm and a shoulder at 440 nm. Since the absorption peak of Ag NSs solution is located at 412 nm, an enhanced absorption induced by LSPR more towards the blue wavelengths than NIR regime was expected. The observed red-shift of the main enhancement peak, however, could be explained by

the PEDOT:PSS material which is spin-casted as a barrier on top of the Ag NSs that tuned the optical absorption peak.

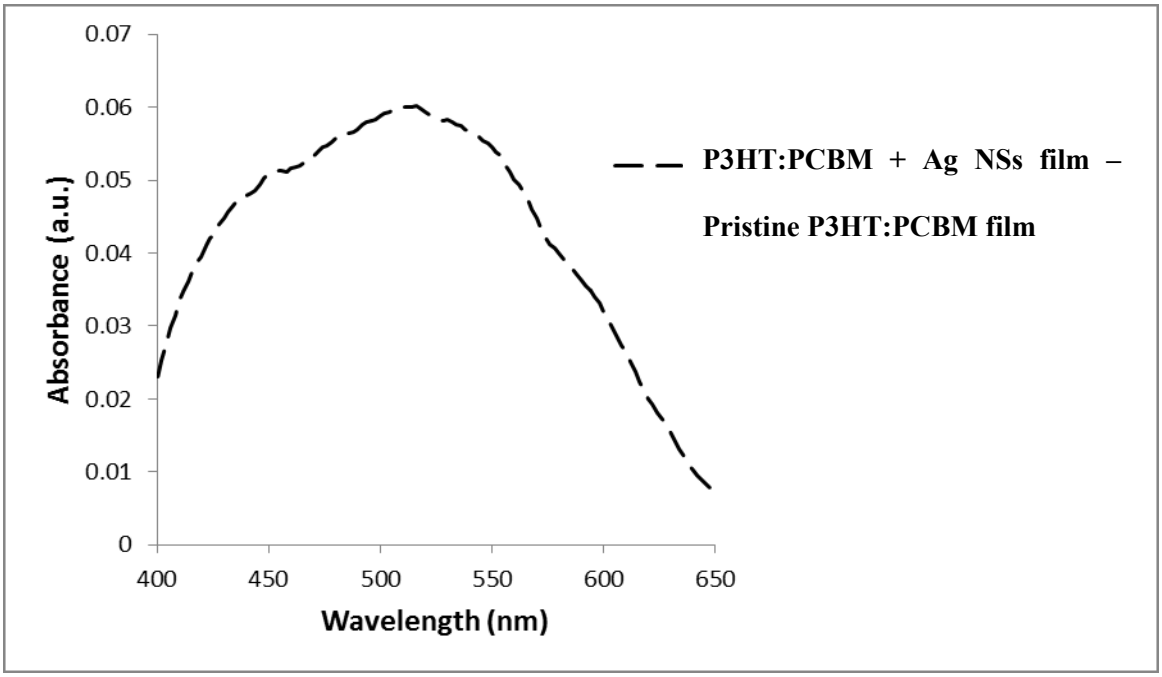

Figure 6-6. Absorption enhancement of Ag NSs-incorporated P3HT:PCBM film compared to the pristine P3HT:PCBM.

The MNPs inside the SCs could also act as the scattering spots and in turn improve the efficiency by increasing the optical path length inside the active layer. However, the light absorption efficiency is higher than the light scattering efficiency for MNPs with diameters smaller than 100 nm. In this study, the average particle radius was around 40 nm, therefore, the achieved improvements in the performance of the OSCs would be prominently related to the LSPR effect [115, 116].

In conclusion, the incorporation of low density Ag NSs directly on top of the ITO anode by means of spin-casting could increase the performance of polymer:fullerene BHJ OSCs. This

enhancement includes not only the optical properties but also the electrical characteristics of the devices as well. That is, the intensified PCE and J_{SC} were observed along with the declined series resistance of the OSC.

6.2 Gold Nanorods-Incorporated OSCs

The Au NRs used in our work possess an average diameter of 25 nm and a length of 60 nm which means an aspect ratio of 2.5. MNPs with this size and shape were selected due to their optical resonance peaks in the wavelength range of interest. Au NPs were used in order to red-shift the plasmon-enhancement wavelength. In general, tuning the plasmon resonance towards the lower energies could be achieved by using Au NPs instead of Ag NPs.

Moreover, although the integrated Au NRs are not considered as big size MNPs in which absorption efficiencies are much higher than scattering ones, their shape give them more ability to forward-scatter the incident light compared to the nanospheres [117]. The concentration of Au NRs in the aqueous solution was ~8.5×10^{10} rods/ml.

The Au NRs with these characteristics demonstrated two absorption resonance peaks. The longitudinal and transverse peaks are observed at 658 nm and 516 nm, respectively. For comparison purposes, the normalized absorption spectra of pristine P3HT:PCBM and Au NRs solution are shown in Figure 6-7.

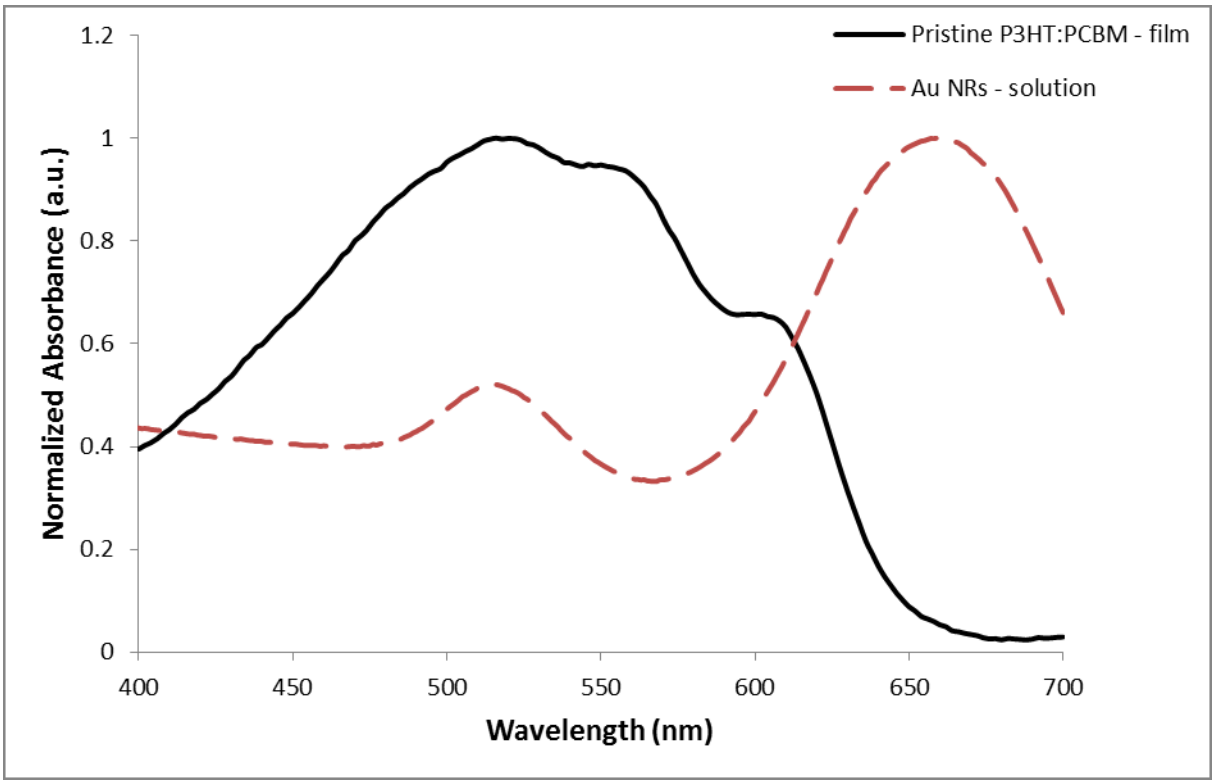

Figure 6-7. Comparison between the absorption profiles of pristine P3HT:PCBM film and Au NRs solution.

The excitation of the conduction band electrons perpendicular to the rod axis (transverse plasmonic mode) and the absorption peak of P3HT:PCBM occurs at almost the same wavelength (518 nm and 516 nm, respectively). This would suggest an intense enhancement in light-harvesting efficiency of the light absorbing material.

Figure 6-8 demonstrates SEM images of Au NRs deposited on ITO-coated glass substrate. The white ellipsoids on the gray background (ITO surface) are Au NRs. The orientation of Au NRs on the ITO surface is arbitrary which implies that both transverse and longitudinal modes are active here. Furthermore, the estimated density based on the SEM images was around 6×10^8 rods/cm^2 which was a very low amount; however, such low densities have already been explored and demonstrated very noticeable contribution to the performance of OSCs [109].

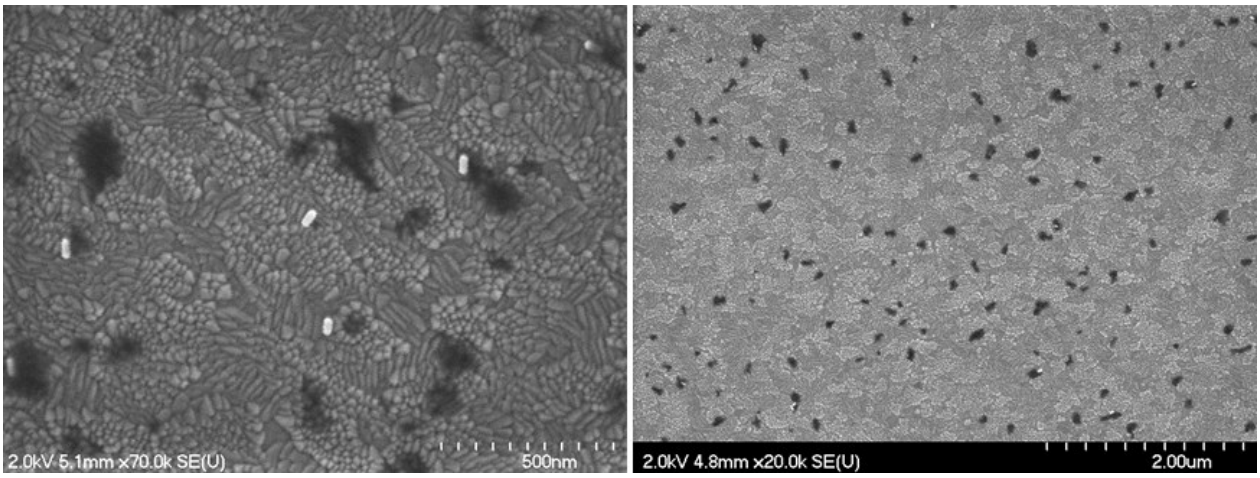

Figure 6-8. SEM micrographs of Au NRs deposited on ITO substrate. The light gray ellipsoids represent the MNPs.

Here again, the reference and plasmonic devices were composed of ITO/ PEDOT:PSS/ P3HT:PCBM/ LiF/ Al and ITO/ Au NRs/ PEDOT:PSS/ P3HT:PCBM/ LiF/ Al, respectively.

Figure 6-9 depicts the J-V characteristics of the fabricated reference and plasmonic devices under illumination and in the dark, respectively. The semi-log graphs are also provided in the insets for more detailed comparison.

Plasmonic SCs integrated with Au NRs on the ITO modified anode exhibited higher performance compared to the base devices without MNPs. PCE was found to increase from 1.86% to 2.10% which is a considerable increase of ~13%. Moreover, the enhancement in J_{SC} by up to 13% shows that the incorporation of Au NRs could contribute to the overall SC performance.

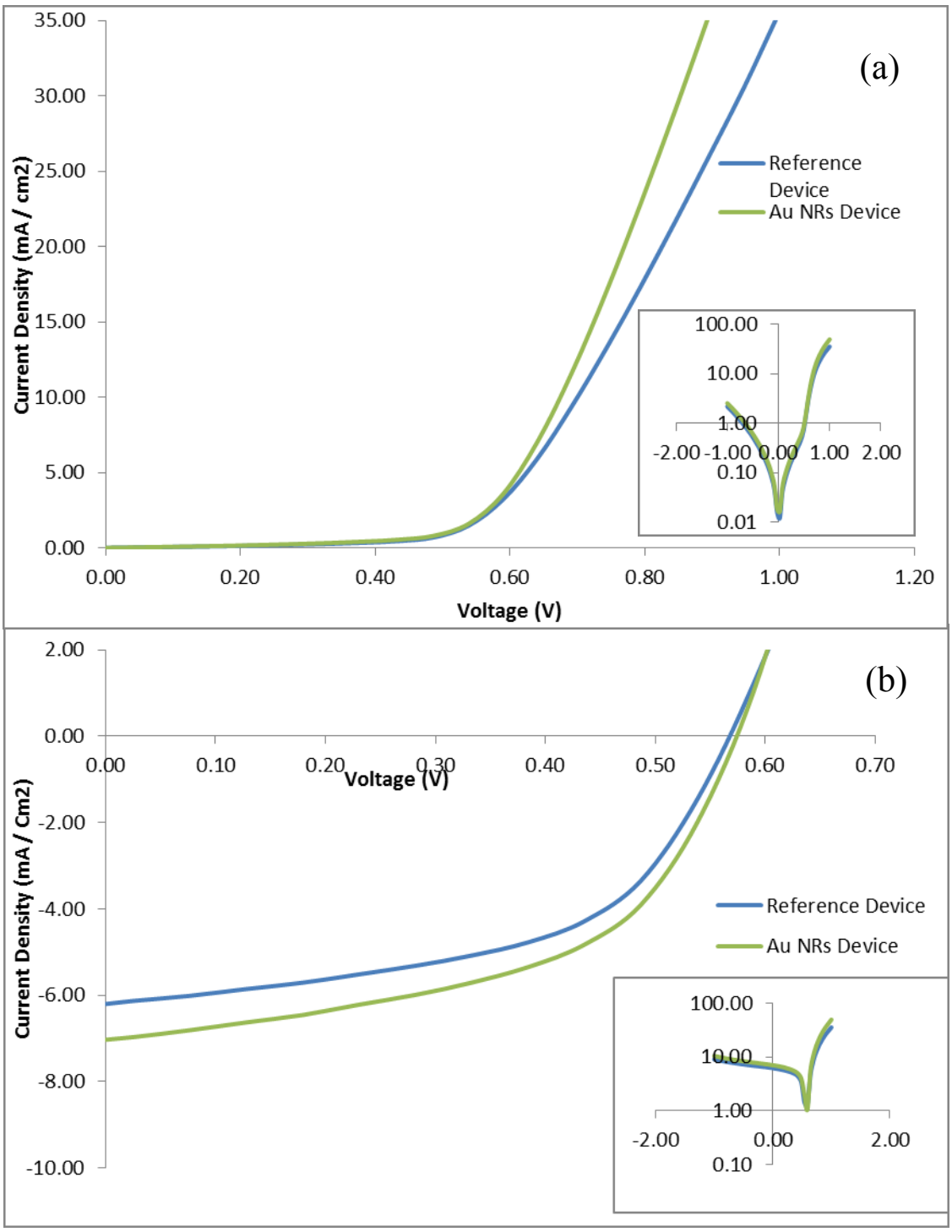

Figure 6-9. J-V characteristics of plasmonic (with Au NRs) and reference (without MNPs) devices (a) in the dark and (b) under illumination. The insets illustrate the semi-log graphs.

Table 6-2 provides a comparative overview of the device characteristics for both reference and plasmonic ones along with their associated standard deviations. The series resistance was calculated according to the slope of J-V curve in the dark condition at 0.8 V.

Table 6-2. Average values for PV parameters for reference and Au NRs devices along with their corresponding standard deviations. Rs is extracted from the slope of JV curve in the dark condition at 0.8 V.

Device type	Voc (V)	Jsc (mA/cm^2)	Rs (Ω/cm^2)	FF (%)	PCE (%)
Reference - without MNPs	0.56	-6.15 ± 0.39	12.15 ± 2.54	54	1.86 ± 0.06
Au NRs	0.58	-6.98 ± 0.41	8.48 ± 4.21	52	2.10 ± 0.07

J_{SC} is affected both by the weak absorbance of photoactive material as well as the insufficient charge transport and collection efficiencies in the interface of the donor and acceptor materials. If the increase in J_{SC} comes from the improvement in charge transportation process inside the P3HT:PCBM material then FF would be enhanced simultaneously [19]. However, in this study we observed an almost similar FF (54% for reference device and 52% for Au NRs-integrated one), implying that the main cause of photocurrent enhancement would be the enhanced absorption in the photoactive material.

Au NRs contributed to the electrical properties of the incorporated device by significantly decreasing the series resistance from 12.15 Ω/cm^2 to 8.48 Ω/cm^2. One reason for the 30% reduction of R_S could be the facilitation of charge transport towards the anode by MNPs as it is

explained in the previous section. However, the unique shape of the Au NRs and their larger size compared to the previously used Ag NSs leads to higher reduction of Rs.

Furthermore, not only the lower series resistance but also the higher open circuit voltage might be achieved due to the work function of Au NRs which matches better with both the PEDOT:PSS work function and the HOMO level of the polymer [109] (Figure 6-10).

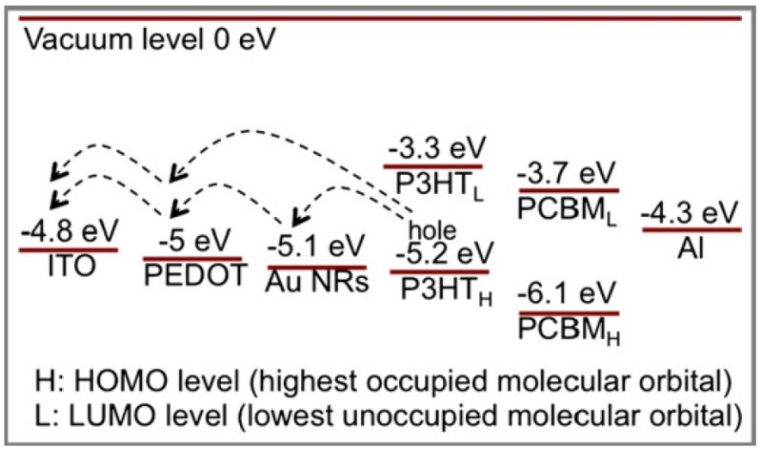

Figure 6-10. Energy band diagram of the materials which are involved in device structure illustrates a precise compatibility between the work function of Au NRs with that of the PEDOT:PSS and also with the HOMO level of P3HT. Reproduced from ref. [109].

In order to make a specific comparison, the absorbance spectra of pristine P3HT:PCBM is depicted along with that of the Au NRs-incorporated device in the same graph (Figure 6-11). The base and plasmonic devices are shown by solid and dashed lines, respectively. Here again, curve D represents the difference between the absorption spectra of devices with and without MNPs on their ITO modified anode.

To better examine the differences, curve D is provided separately in Figure 6-12.

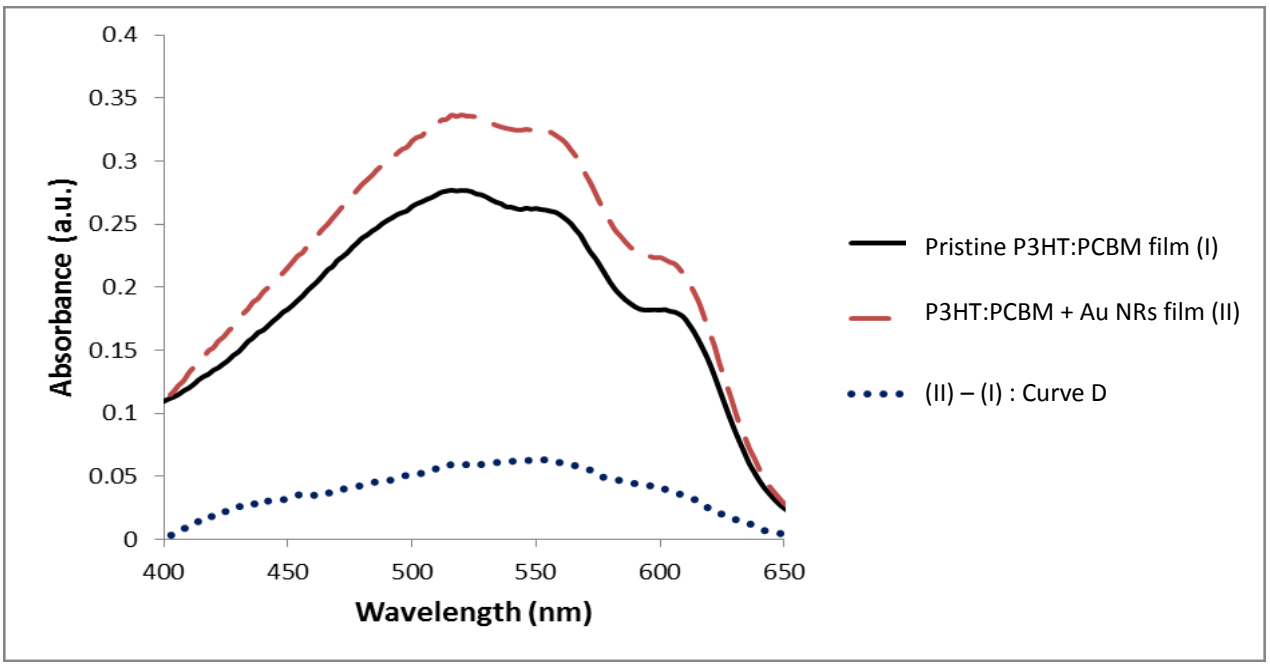

Figure 6-11. Comparison between absorption profiles of pristine P3HT:PCBM film and Au NRs-incorporated P3HT:PCBM film. Curve D illustrates the absorption enhancement of Au NRs-integrated film compared to that of the pristine device.

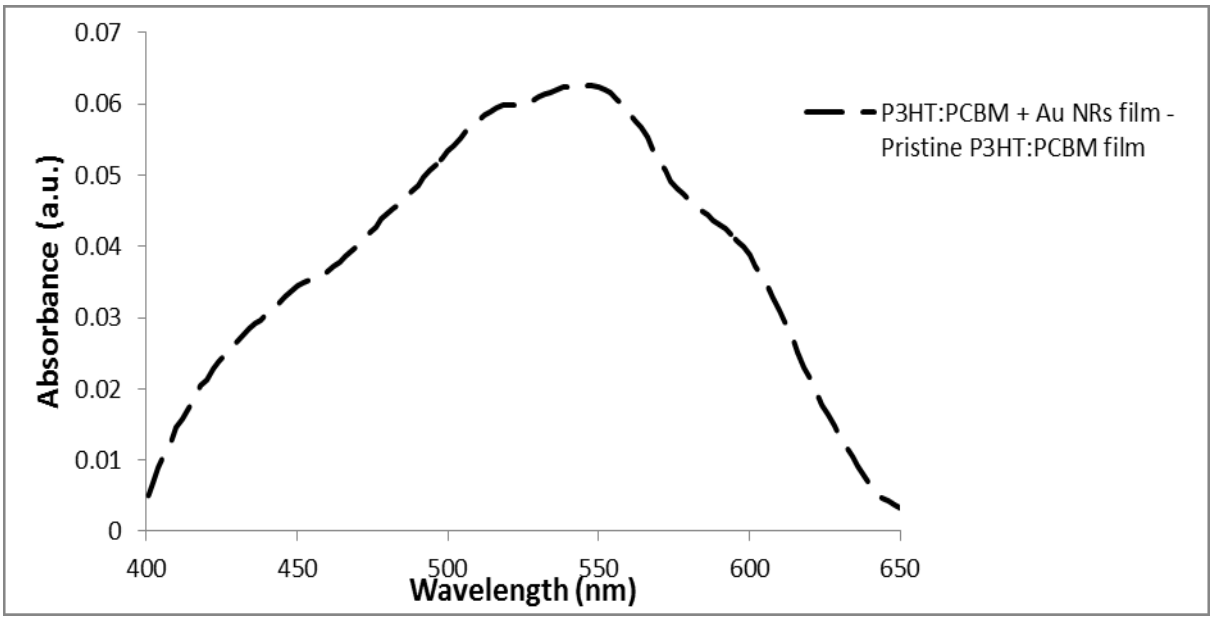

Figure 6-12. Absorption enhancement of Au NRs-incorporated P3HT:PCBM film compared to the pristine P3HT:PCBM.

Curve D shows a peak at 542 nm and a shoulder at 510 nm. These enhancements were expected due to the transverse excitation mode of incorporated Au NRs. The slight convexity towards blue wavelengths might also be related to this absorption mode. The third shoulder at 602 nm could be linked to the longitudinal mode of Au NRs.

According to the characterization results, it could be concluded that the incorporation of Au NRs inside the BHJ OSC could enhance both the optical and electrical performance of the device. The deposited MNPs on the surface of ITO modified anode increased the incident light harvesting by means of LSPR effect. The intensified optical absorption inside the P3HT:PCBM layer would lead to the enhancement of the photoconversion at solar-conversion relevant wavelengths.

6.3 Comparison between Incorporated OSCs with either Au NRs or Ag NSs

In general, incorporation of MNPs with appropriate size, shape and by considering a suitable surrounding medium could increase the performance of OCSs. However, the quality and quantity of these modifications depend mainly on the position and intensity of the MNPs resonance peaks and their compatibility with the absorption spectra of the photoactive material.

Since both plasmonic nanostructured devices, incorporated with either Au-NRs or Ag NSs, were made under similar experimental conditions, it would be interesting to compare their characteristics.

In Figure 6-13, the normalized absorbance spectra of Au NRs, Ag NSs, and pristine P3HT:PCBM are compared.

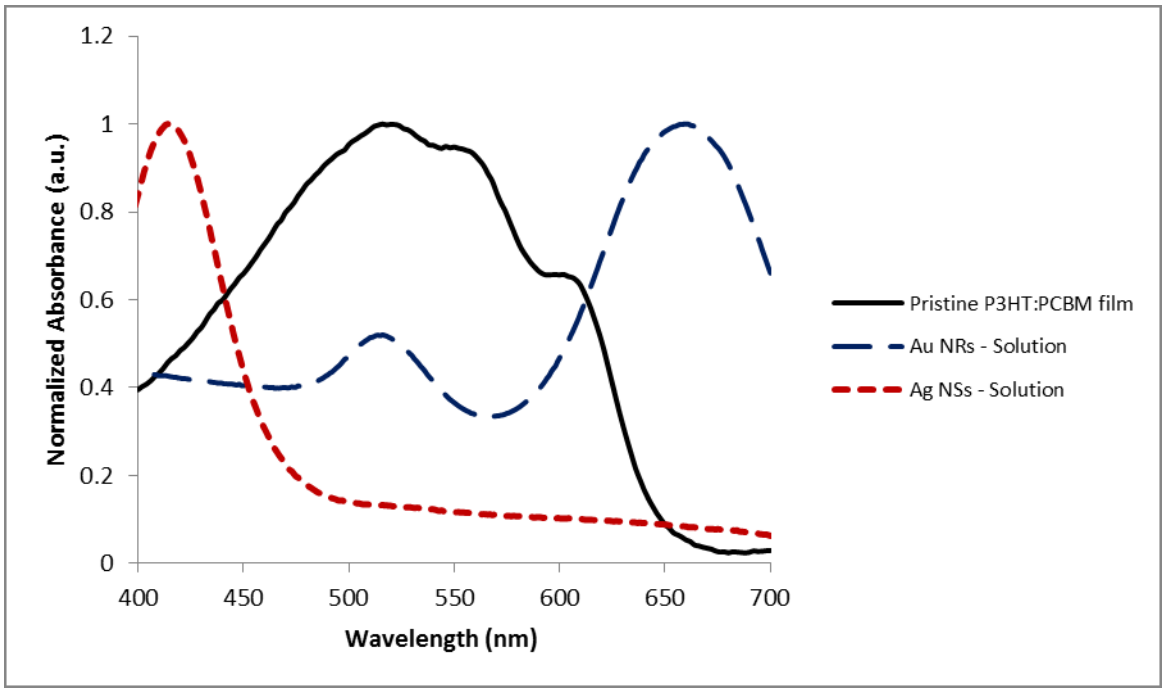

Figure 6-13. Absorption modes of a pristine P3HT:PCBM film (black solid line), an Au NRs colloidal solution (blue dashed line), and an Ag NSs colloidal solution (red dashed line).

Both transverse and longitudinal resonance peaks of Au NRs are located more towards the red wavelengths; on the other hand, the one for Ag NSs is situated near the blue wavelengths. Thereby, the incorporation of these MNPs is expected to give optical enhancements to the light harvesting of photoactive material at or close to their absorption peaks.

The enhanced absorption of modified photoactive material from the base pristine P3HT:PCBM by the incorporation of either Au NRs or Ag NSs is shown in Figure 6-14. Au NRs-integrated films showed an enhanced absorbance in the broad wavelength range from 400 nm to 650 nm just similar to that of the Ag NSs-integrated ones. However, the main intensified peaks are situated at different regimes due to the difference between the absorption peaks of Au NRs and Ag NSs.

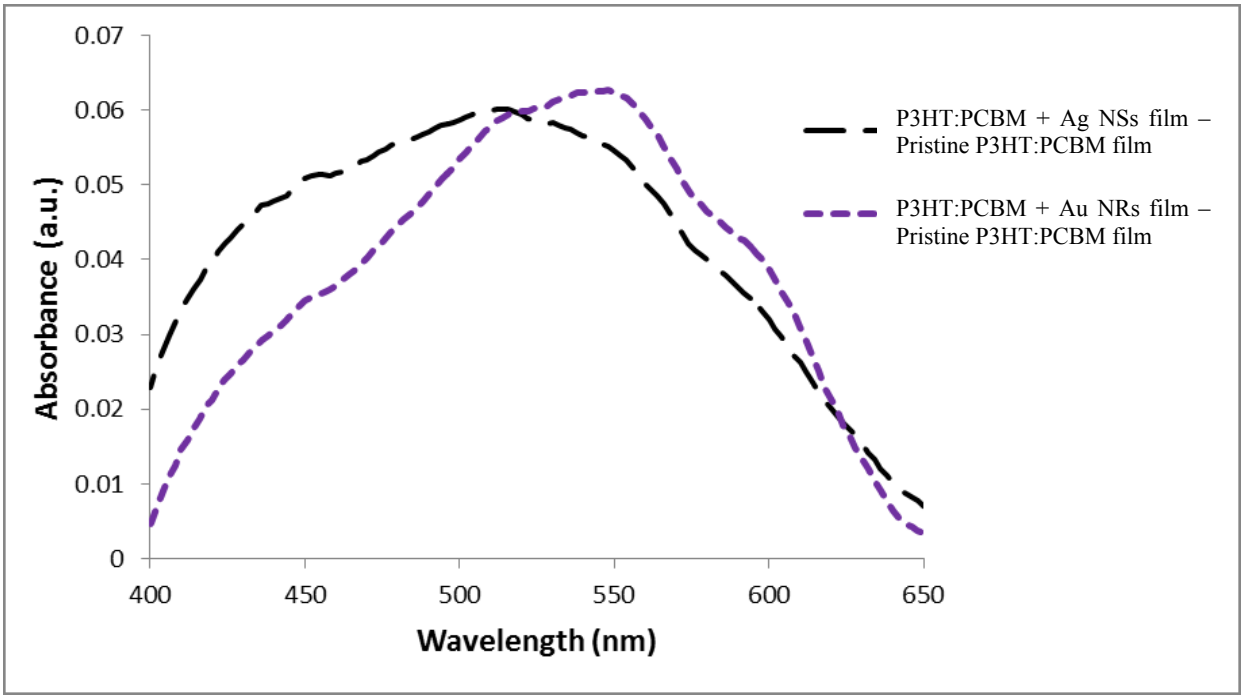

Figure 6-14. Comparison between the absorption enhancement of Au NRs-incorporated P3HT:PCBM film with that of Ag NSs-integrated film.

It is worth noting that while the size of the MNPs are noticeably less than the thickness of the PEDOT:PSS buffer layer, their contribution to the optical absorption is insignificant since the enhanced field is localized around the NPs and it decreases exponentially with distance. Thereby, the intensified EM could not reach the photoactive material.

However, the MNPs with similar sizes or even taller than the thickness of the buffer layer show dramatic increase in the light absorption efficiency of P3HT:PCBM [118]. In this study, the measured thickness of the PEDOT:PSS layer was 35±5 nm, and Ag NSs with diameter of 40 nm and Au NRs with 60 nm length and 25 nm radius were used.

Figure 6-15 depicts the J-V curves of all devices with and without MNPs under illumination and in the dark condition.

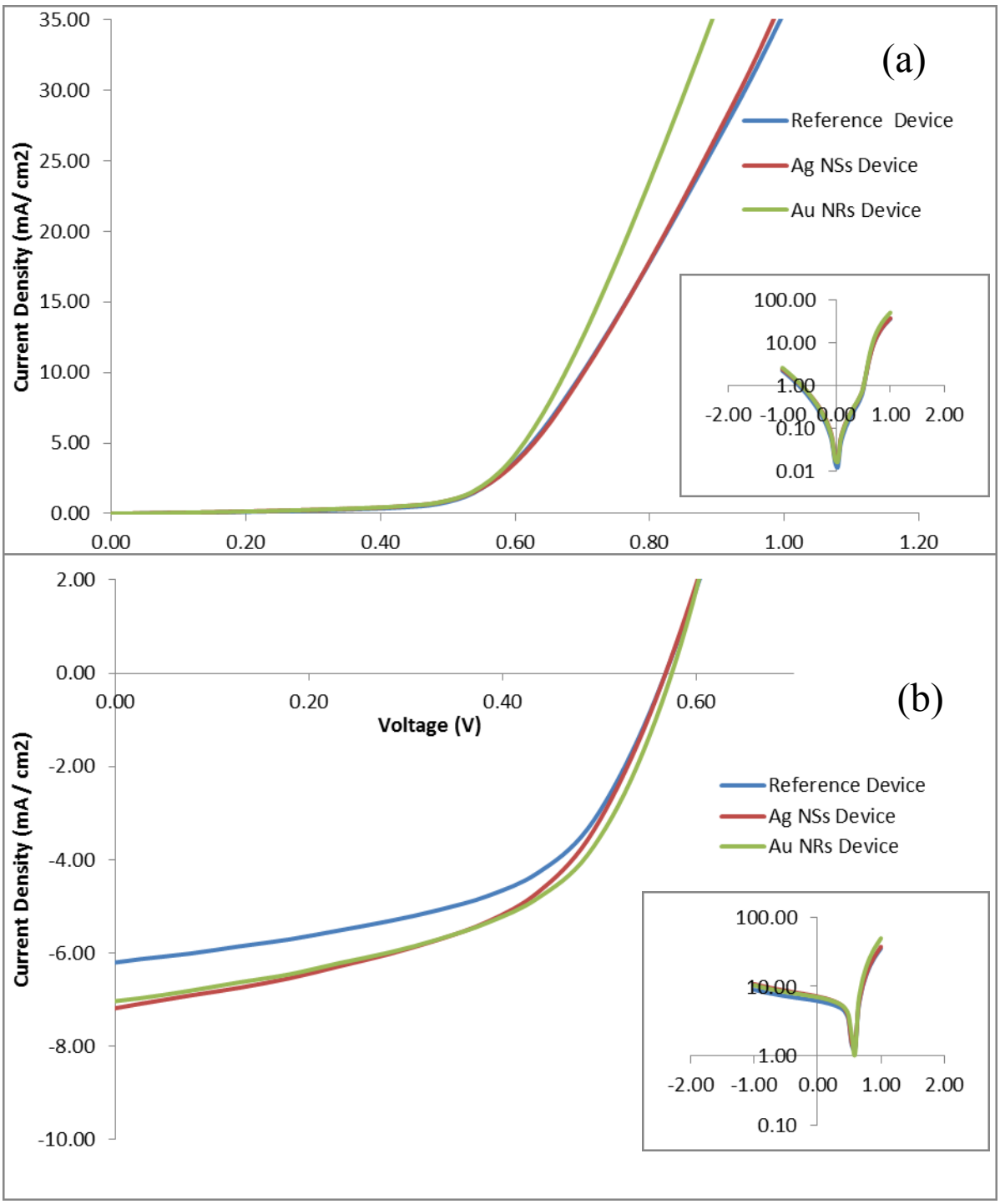

Figure 6-15. J-V characteristics of plasmonic (with either Au NRs or Ag NSs) and reference (without MNPs) devices (a) in the dark and (b) under illumination. The insets illustrate the semi-log graphs.

PCE and J_{SC} of both plasmonic devices showed a noticeable improvement with respect to the reference device. Moreover, FF and V_{OC} almost remained the same with minor modifications in some cases. Moreover, the series resistance were also reduced which could enhance the overall performance of the plasmonic devices incorporated with either Au NRs or Ag NPs. The corresponding photovoltaic parameters are summarized in Table 6-3.

Table 6-3. Average values for PV parameters for reference devices as well as the devices with either Au NRs or Ag NSs, along with their corresponding standard deviations. Rs is extracted from the slope of JV curve in the dark condition at 0.8 V.

Device type	Voc (V)	Jsc (mA/cm^2)	Rs (Ω/cm^2)	FF (%)	PCE (%)
Reference - without MNPs	0.56	-6.15 ± 0.39	12.15 ± 2.54	54	1.86 ± 0.06
Ag NSs	0.56	-7.10 ± 0.52	11.73 ± 2.12	53	2.07 ± 0.07
Au NRs	0.58	-6.98 ± 0.41	8.48 ± 4.21	52	2.10 ± 0.07

Eenhancements in PCE for devices integrated with Ag NSs and Au NRs are ~11% and ~13%, respectively. Respecting the same order, the same plasmonic devices enhanced the J_{SC} of the reference device by up to 15% and 13%, respectively.

However, as it is mentioned before, the difference between series resistance improvements were noticeable which was higher in the case of Au NRs than the Ag NSs-incorporated device. The reason could be the precise match between the work function of Au NRs (~ -5.1 eV) and that of the anode. However, there is a different scenario for Ag NSs, since their presence could even reduce the work function of ITO [107].

Altogether, the deposited MNPs on ITO-coated glass could modify the charge transport and collection process through the anode due to their higher conductivity compared to PEDOT:PSS and their effect on the surface morphology of the buffer layer [118].

6.4 Bimetallic Nanostructured OSCs

In order to take advantage of both MNPs simultaneously, Au NRs and Ag NSs were blended physically with the same ratio. Figure 6-16 depicts the normalized UV-vis absorption spectra for the achieved bimetallic nanostructure along with that of pristine P3HT:PCBM.

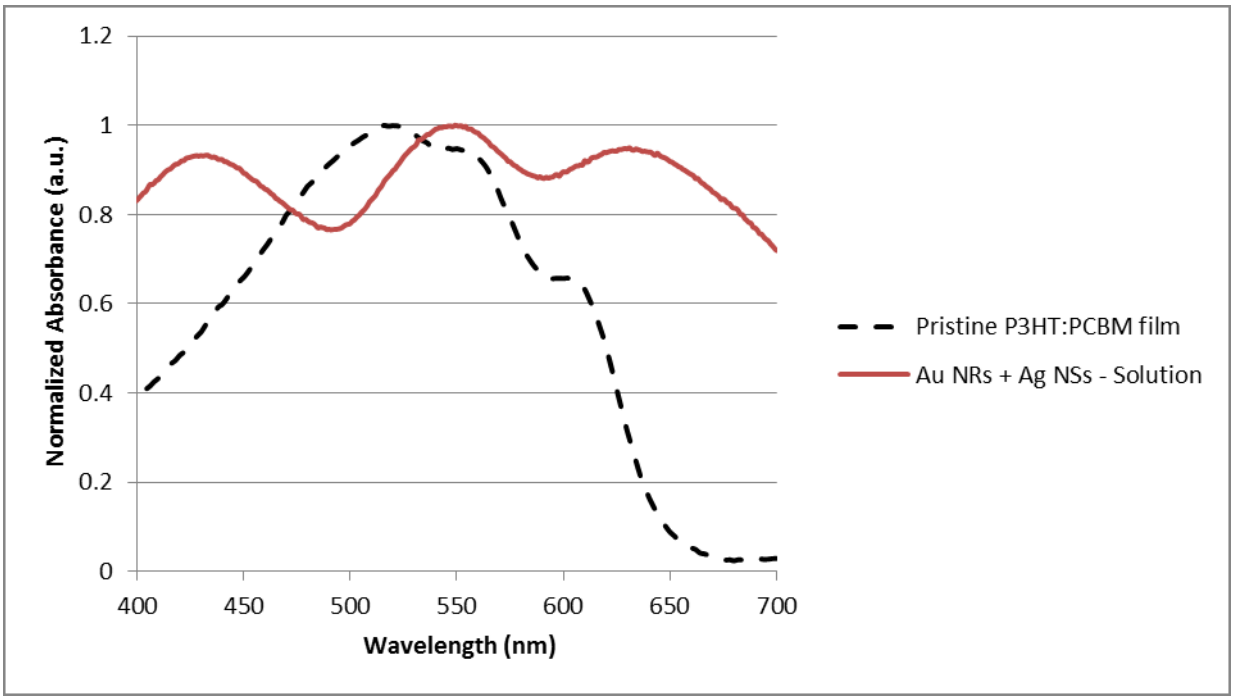

Figure 6-16. Absorption modes of a pristine P3HT:PCBM film (black dashed line), an Ag NSs+Au NRs blend colloidal solution (red solid line).

Three peaks at 432 nm, 550 nm and 636 nm are observed in the absorption spectra of double metallic nanostructure solution, which could fully cover the absorption regime of photoactive material.

Due to the broad absorption spectra of the dual metallic nanostructure and the intense peaks at or close to the absorption peaks and shoulders of P3HT:PCBM, a significant enhancement in the light harvesting efficiency of polymer:fullerene BHJ active material is expected.

SEM micrographs are made for investigating the morphology, uniformity, and aggregation of the deposited bimetallic solution film on ITO modified substrate (Figure 6-17).

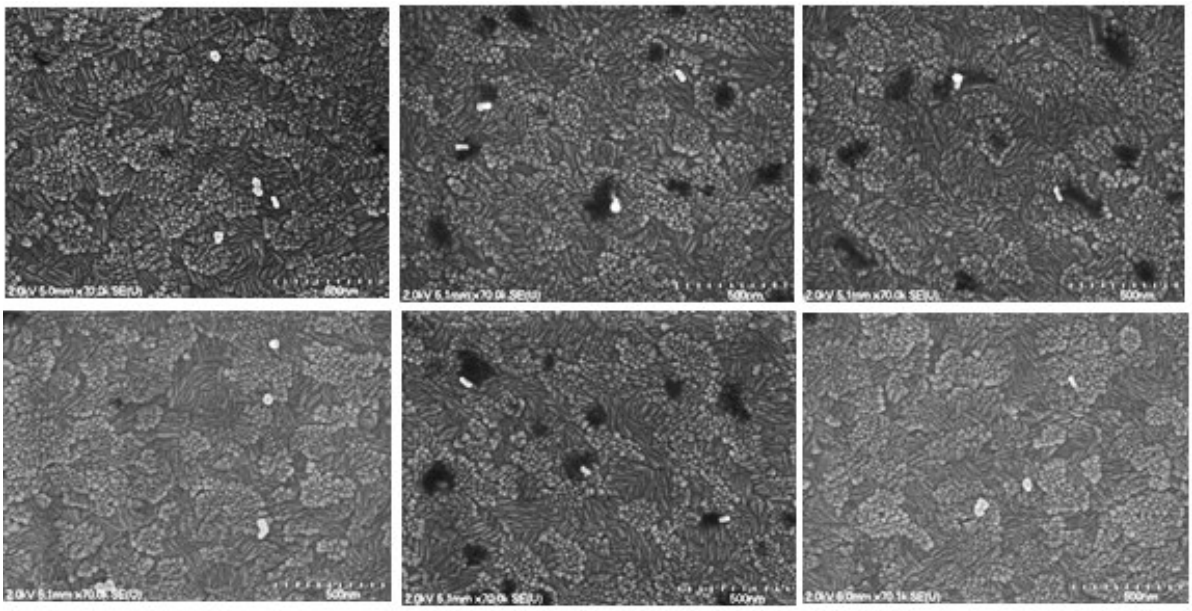

Figure 6-17. SEM micrographs of Au NRs+Ag NSs dual plasmonic nanostructured colloidal solution deposited on the ITO substrate. The light gray ellipsoids and spheres represent Au NRs and Ag NSs, respectively.

According to SEM images, the MNPs are incorporated with arbitrary orientations. The films could be considered homogenous with a very low density around ~8×10^8 NPs/cm^2. The presence of both Au NRs and Ag NSs with almost the same density indicates that both MNPs would be active in contributing to the light-trapping process by means of plasmonic effect.

In this experiment, the reference and MNPs-incorporated devices possess the structure of ITO/ PEDOT:PSS/ P3HT:PCBM/ LiF/ Al and ITO/ Ag NSs+Au NRs/ PEDOT:PSS/ P3HT:PCBM/

LiF/ Al, respectively. J-V characteristics of both plasmonic and reference devices in the dark and under illumination are provided in Figure 6-18.

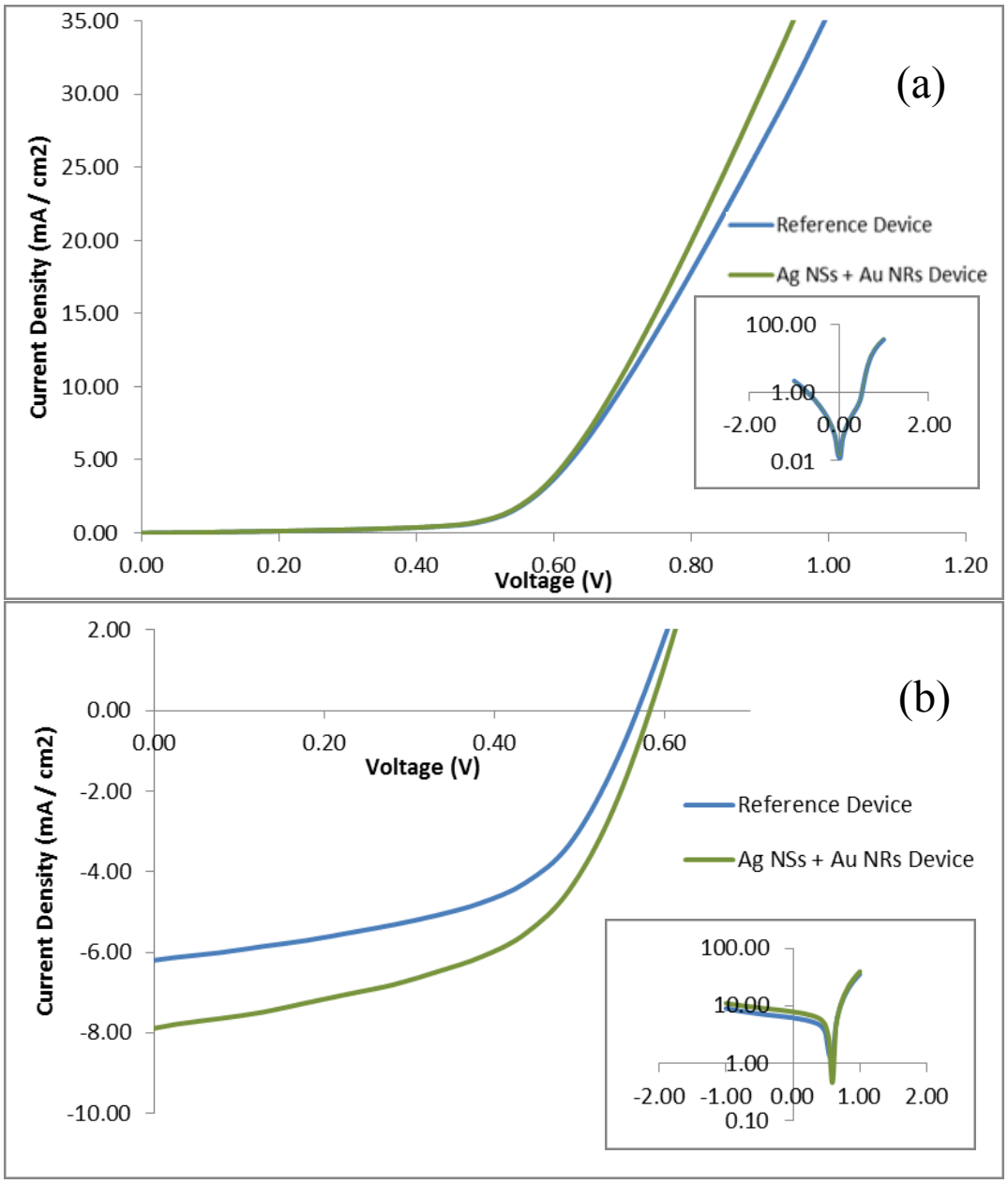

Figure 6-18. J-V characteristics of plasmonic (with Au NRs+Ag NSs bimetallic nanostructure) and reference devices (a) in the dark and (b) under illumination. The insets illustrate the semi-log graphs.

Table 6-4. Average values for PV parameters of reference and Au NRs+Ag NSs dual metallic device along with their corresponding standard deviations. Rs is extracted from the slope of JV curve in the dark condition at 0.8 V.

Device type	Voc (V)	Jsc (mA/cm^2)	Rs (Ω/cm^2)	FF (%)	PCE (%)
Reference - without MNPs	0.56	-6.15 ± 0.39	12.15 ± 2.54	54	1.86 ± 0.06
Ag NSs + Au NRs	0.57	-7.81 ± 0.54	10.41 ± 4.07	54	2.43 ± 0.14

According to the PV parameters which are summarized in Table 6-4, a noticeable upward trend in the value of PCE is observed from 1.86% to 2.43% after introducing the dual metallic nanostructure of Au NRs plus Ag NSs. J_{SC} is also increased from 6.15 mA/cm^2 to 7.81 mA/cm^2, which means an enhancement by up to 27%. Besides, FF and V_{OC} remained at almost the same value. The extracted series resistance of the plasmonic and reference devices were 10.41 Ω/cm^2 and 12.15 Ω/cm^2, respectively.

R_S was derived from the slope of J-V curve in the dark at 0.8 V. The reduction of series resistance by up to 14% indicates remarkable improvement of the electrical properties of the device.

Altogether, the performance of OSCs integrated with bimetallic nanostructure of Au NRs plus Ag NSs showed a significant improvement. To investigate the origin of this enlargement, a comparative study were made between the absorption spectra of bimetallic nanostructured P3HT:PCBM and that of the pristine one.

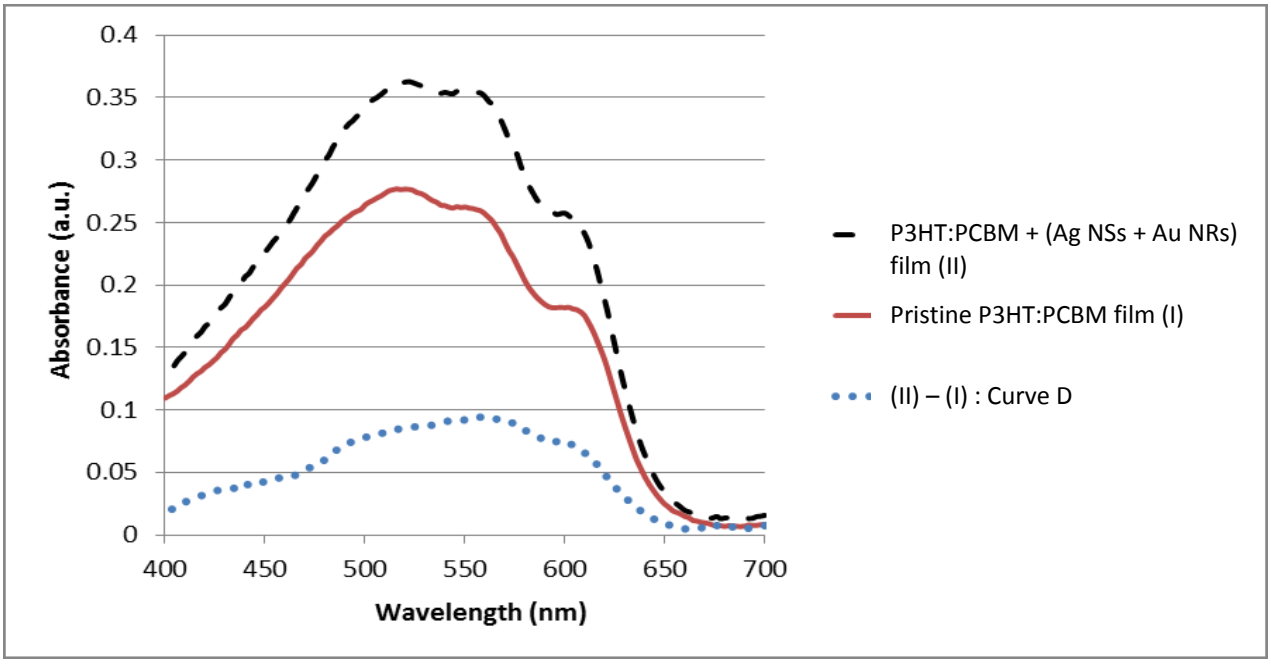

Figure 6-19. Comparison between absorption profiles of pristine P3HT:PCBM film and (Au NRs+Ag NSs) dual metallic nanostructure-integrated P3HT:PCBM film. The difference between these two films depicted as Curve D.

Figure 6-19 represents the absorbance of P3HT:PCBM with (black dashed line) and without (red solid line) dual Au NRs and Ag NSs metallic nanostructure. The third curve (blue doted line) is the difference between these two, which is named as curve D.

Due to the similar absorbance shapes of plasmonic and pristine films, curve D is shown separately in Figure 6-20 in order to determine the multi-mode excitation wavelengths. A main maximum at 558 nm, a main shoulder at 520 nm with a convexity between 478 nm and 520 nm, a second shoulder at 594 nm and a slight convexity between 400 nm and 450 nm are observed in this graph.

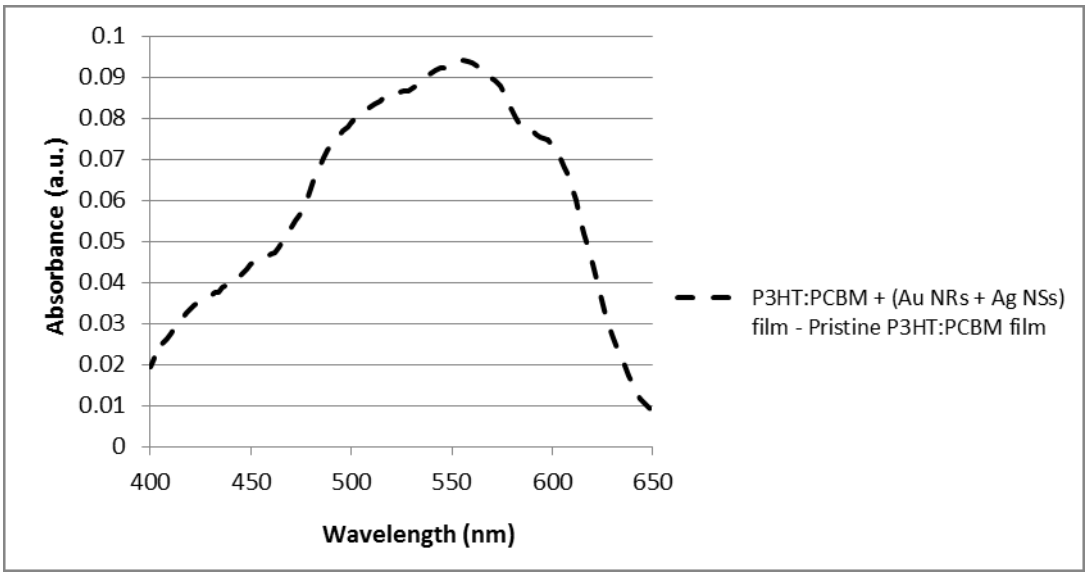

Figure 6-20. Absorption enhancement of (Au NRs+Ag NSs)-incorporated P3HT:PCBM film compared to the pristine P3HT:PCBM film.

The precise match between the resonance peaks of MNPs and the enhanced absorption of photoactive material implies that the reason behind enhanced performance of the plasmonic devices would be the plasmonic effect. The strong near field, induced by LSPR from both Au NRs and Ag NSs, penetrated into the photoactive material and enhanced the light absorption and exciton creation, thereby, increased the generated photocurrent and overall PCE of the MNPs-incorporated OSCs.

In conclusion, OSCs with a dual metallic nanostructure introduced directly on top of the modified ITO showed an enhanced performance. In order to achieve the suggested bimetallic NPs solution, the same ratio of Ag NSs (with 40 nm diameter) and Au NRs (with 60 nm length and 25 nm diameter) were physically mixed. A factor of 30% and 27% enhancement were measured for PCE and J_{SC}, respectively.

6.5 Comparison and Analysis of Results

A comparative study is required in order to determine the differences between the effects of incorporating either Au NRs, Ag NSs or a combination of both MNPs as an interfacial layer between ITO and PEDOT:PSS.

Figure 6-21 represents the absorption spectra of pristine P3HT:PCBM, Au NRs, Ag NSs, and the bimetallic structure in a single graph.

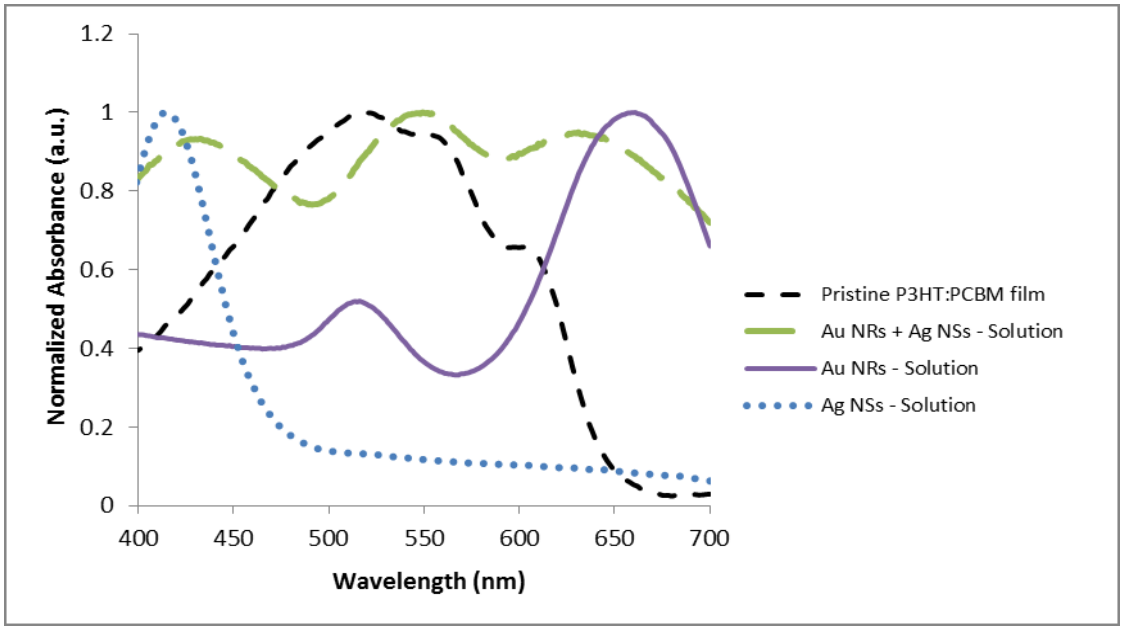

Figure 6-21. Absorption modes of a pristine P3HT:PCBM film (black dashed line), an Au NRs colloidal solution (purple solid line), and an Ag NSs colloidal solution (blue dotted line) and (Au NRs+Ag NSs) bimetallic nanostructure colloidal solution (green dashed line).

The multi-mode excitations of (Au NRs+Ag NSs) solution could be attributed to the absorption peaks of Au NRs and Ag NSs. That is, the peak at 432 nm could be linked to the resonance peak of Ag NSs and the peaks at 550 nm and 636 nm could be related to the transverse and longitudinal modes of Au NRs, respectively. This suggests that the combination of these two

different MNPs with dissimilar shape and size and consequently with various resonance regimes could complement each other and in turn broadens the absorption spectra. Moreover, it could be concluded that all resonance peaks of both MNPs are supposed to actively contribute to the enhanced efficiency. In this scenario, the intensified electric field induced by LSPR increases the photon absorption and consequently exciton generation. As mentioned before, however, the locally enhanced EM field around the MNPs could penetrate inside the active layer if MNPs are located close to the interface between the active layer and PEDOT:PSS. This is why the thickness of PEDOT:PSS and the sizes of MNPs are selected in the same order.

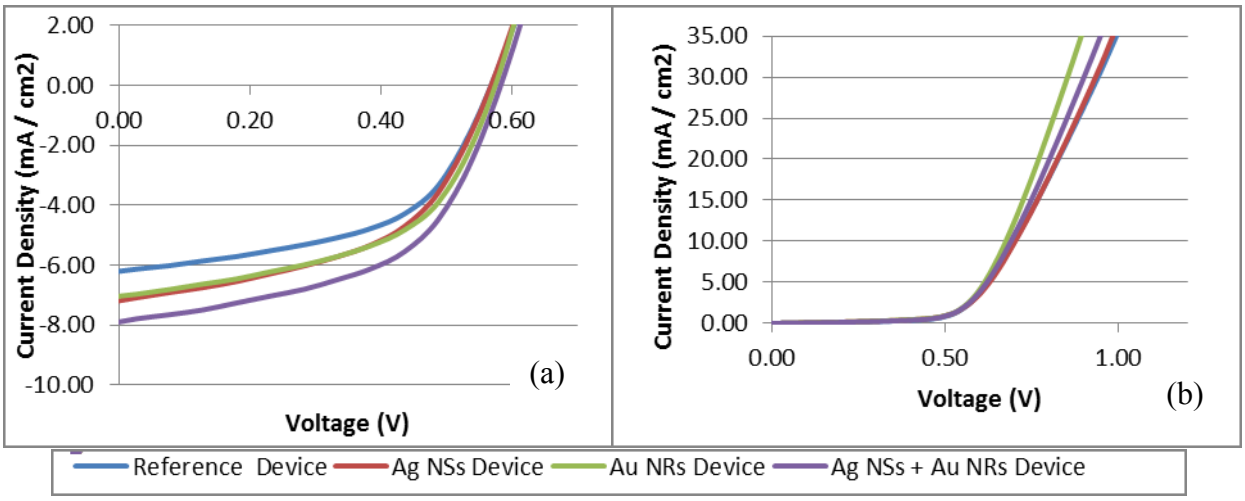

Figure 6-22. J-V characteristics of plasmonic (with either Au NRs, Ag NSs or Au NRs+Ag NSs) and reference devices (a) under illumination and (b) in the dark.

J-V characteristics of reference and plasmonic devices incorporated with either Au NRs, Ag NSs or Au NRs+Ag NSs are presented in the dark and under illumination in Figure 6-22.

PV parameters are provided in Table 6-5 along with their standard deviations.

Table 6-5. Average values of PV parameters for reference device as well as the devices with either Au NRs, Ag NSs and Au NRs+Ag NSs along with their corresponding standard deviations. Rs is extracted from the slope of JV curve in the dark condition at 0.8 V.

Device type	$Voc\ (V)$	Jsc (mA/cm^2)	Rs (Ω/cm^2)	FF (%)	PCE (%)
Reference - without MNPs	0.56	-6.15 ± 0.39	12.15 ± 2.54	54	1.86 ± 0.06
Ag NSs	0.56	-7.10 ± 0.52	11.73 ± 2.12	53	2.07 ± 0.07
Au NRs	0.58	-6.98 ± 0.41	8.48 ± 4.21	52	2.10 ± 0.07
Ag NSs + Au NRs	0.57	-7.81 ± 0.54	10.41 ± 4.07	54	2.43 ± 0.14

Overall device performance is improved by incorporation of MNPs. PCE of the reference device increased by up to 11%, 13% and 30% for plasmonic devices integrated with Ag NSs, Au NRs and Ag NSs+Au NRs, respectively. These values demonstrated the effect of broadened absorption spectra of bimetallic nanostructured plasmonic OSCs as compared with that of the Au NRs- or Ag NSs- integrated devices. Moreover, the values for J_{SC} were increased in a similar manner. That is, the enhancement for devices with metallic nanostructure was more remarkable than that of the devices with only Au NRs or Ag NSs.

Besides, although FF was slightly changed in the case of single MNPs-incorporated devices, it remained at the same value for double MNPs-integrated devices, implying the unchanged nature of the electrode-organic interface. The improvements in the values of both V_{OC} and series resistance are the highest for devices with Au NRs, the lowest for the ones with Ag NSs, and intermediate for OSCs with dual nanostructures. The significant reduction of series resistance of devices with Au NRs could be attributed to the work function of these MNPs, and this value might be lowered in the dual nanostructured devices by the undesirable work function of Ag NSs.

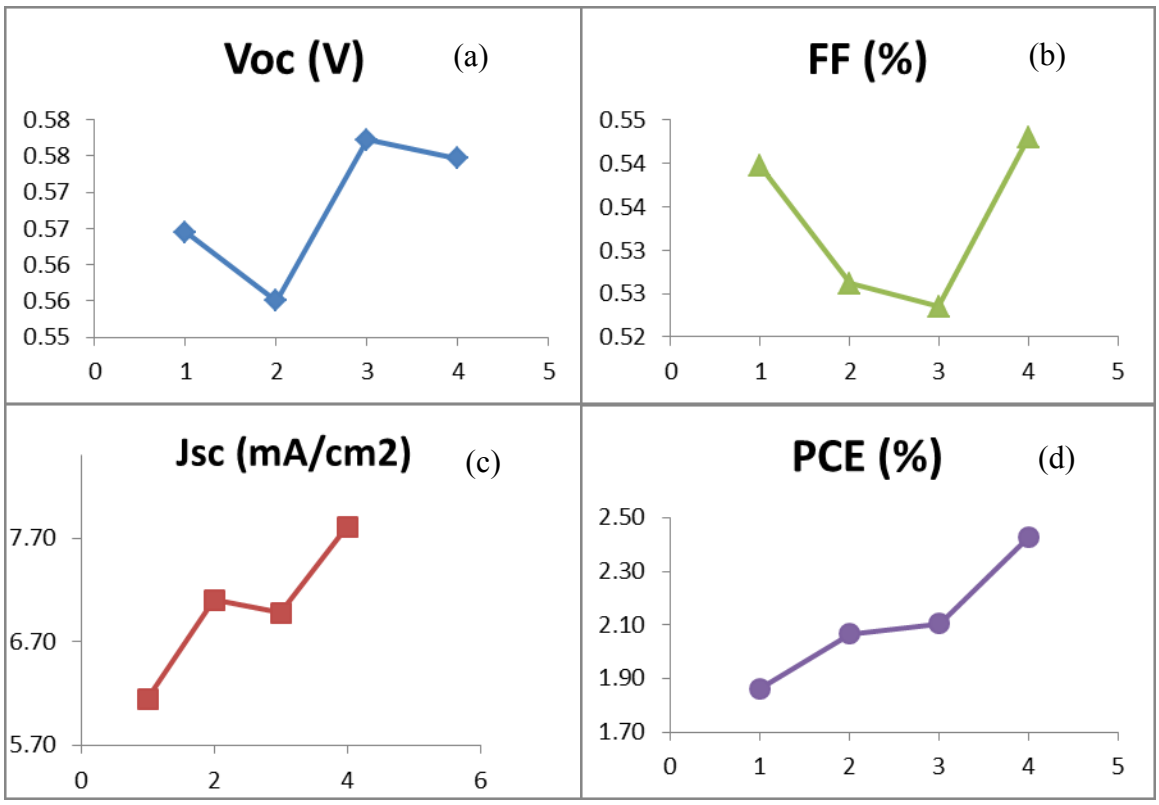

Figure 6-23. Comparative study between PV parameters of OSCs with different conditions. The x axis in all graphs is scaled according to the device number; #1, #2, #3 and #4 stand for reference, Ag NSs, Au NRs, and Ag NSs+Au NRs devices, respectively. Various PV parameters including (a) V_{OC} , (b) FF, (c) J_{SC}, and (d) PCE are investigated.

Figure 6-23 facilitates the comparative study between the main device parameters. The fact that integration of MNPs leads to essential improvements in photogenerated current rather than open circuit voltage or even FF, strongly indicates that these modifications are based on plasmon-enhanced absorption of photoactive material [119]. For more detailed investigations, the absorption spectra of P3HT:PCBM with and without MNPs is shown in Figure 6-24.

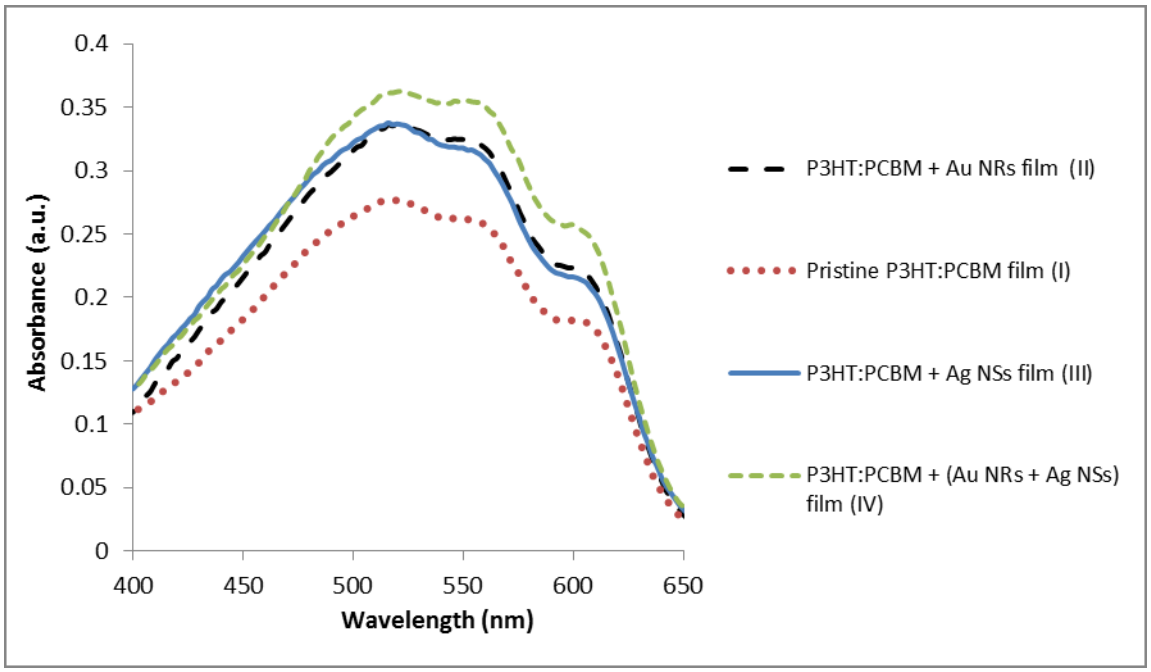

Figure 6-24. Comparison between absorption profiles of P3HT:PCBM film under different conditions: without MNPs(pristine), with Au NRs, with Ag NSs, and with (Au NRs+Ag NSs) dual metallic nanostructure.

Although, a considerable enhancement in optical properties of Au NRs- or Ag NSs-integrated photoactive materials are observed compared to that of the pristine one, the intensified increase is evident in the case of dual metallic nanostructured P3HT:PCBM. Figure 6-25 illustrates the difference of absorption spectra between plasmonic (integrated with Au NRs, Ag NSs, and Ag NSs+Au NRs) and pure polymer:fullerene BHJ material.

Although both MNPs could enhance the absorption of photoactive material within the visible regime, Au NRs offer a stronger absorption between 530 nm and 650 nm whereas this wavelength shifts to 400 nm till 530 nm for Ag NSs. In fact, the 530 nm wavelength is the

intersection of two absorption enhancement spectra of Au NRs- and Ag NSs-incorporated photoactive material based on the pristine P3HT:PCBM.

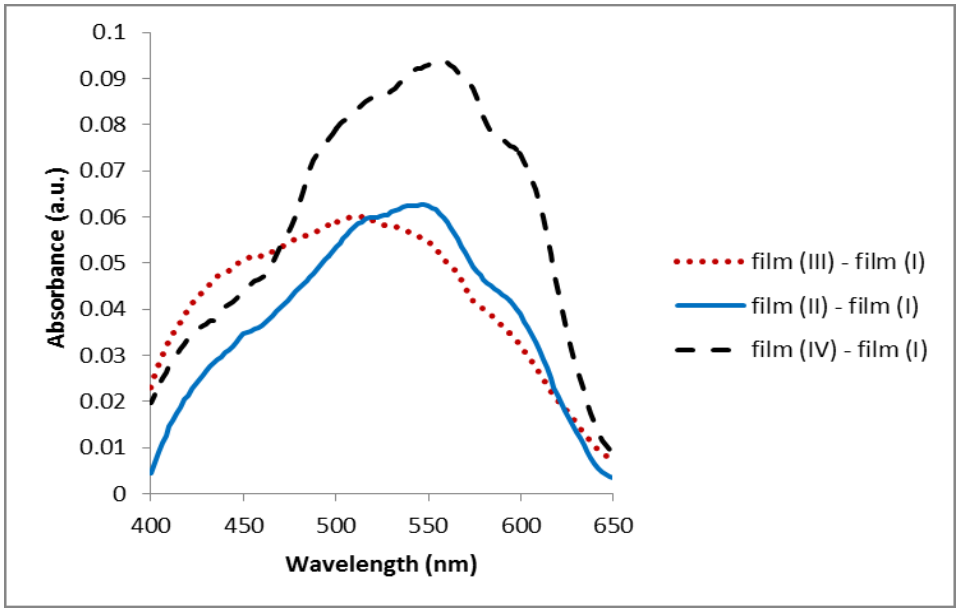

Figure 6-25. Absorption enhancement of MNPs-incorporated P3HT:PCBM films from that of the pristine P3HT:PCBM one (film I). A comparison between Ag NSs (film III), Au NRs (film II), and Ag NSs+Au NRs integrated films (film IV).

This confirms that the absorption enhancement by Au NRs and Ag NSs combine and in turn simultaneously contribute to the light harvesting and exciton generation inside the photoactive layer of bimetallic nanostructured OSCs. The higher values for J_{SC} and PCE of dual metallic nanostructured plasmonic devices as compared to that of Au NRs- or Ag NSs-incorporated OSCs could also be explained based on the same reason.

CONCLUSIONS

This work deals with the effects of a bimetallic nanostructured solution composed of Au NRs and Ag NSs introduced into an OSC by means of spin-casting on top of an ITO modified anode. The results revealed a significant enhancement in PCE and J_{SC} by up to 30% and 27%, respectively.

In order to understand the mechanisms responsible for these improvements, first the OSCs with only one type of MNPs were fabricated and characterized. The fabrication process included various chemical and deposition techniques. In our study, the standard reference OSC possesses the structure of ITO/ PEDOT:PSS/ P3HT:PCBM/ LiF/ Al.

Two dissimilar MNPs with different properties were selected. They were then optimized in terms of various parameters, such as optical and structural effects of nano-meter sized metallic particles resulting from differences in geometry, density, size, and shape (e.g. the match between their resonance peaks and maximum absorption spectra of the photoactive material).

In addition, the sizes of MNPs were also chosen based on the thickness of PEDOT:PSS. Since the enhanced electric field induced by LSPR decreases exponentially with distance, the center of the MNPs should be close enough to the interface of buffer layer and P3HT:PCBM in order to penetrate into the photoactive material and increase its light absorption.

As deduced form the characterization data, the transverse and longitudinal resonance peaks of Au NRs with length of 60 nm and diameter of 25 nm (with aspect ratio of 2.5) are situated towards the NIR regime. Moreover, Au NRs were found to possess enhanced forward-scattering properties due to their unique shape. On the other hand, the absorption peak of Ag NSs with 40 nm radius is situated more towards the blue wavelength regime.

Au NRs-incorporated OSCs showed remarkable enhancements both in PCE and J_{SC}. However, FF and V_{OC} remained the same. A similar behavior was observed for Ag NSs-integrated devices. Consequently, light harvesting enhancement and, in turn, greater exciton generation could be considered as the origin of improved performance of our devices. If the enhanced charge transport and collection efficiency were the main reasons of performance improvements, then the FF should also exhibit significant increases.

It is worth noting that not only the optical characteristics but also the electrical properties of devices were improved significantly by incorporation of MNPs, specifically in the case of Au NRs.

After investigating the individual characteristics of Au NRs and Ag NSs-integrated devices, we studied the impact of the double plasmonic structure on the performance of OSCs. The spectrophotometry results revealed that the absorption spectra of P3HT:PCBM with an interfacial layer of combined Ag NSs and Au NRs was more broad and more intense as compared to that of the incorporated devices with only one type of MNPs. This indicates that the absorption enhancement from different metallic nanoparticles combine and contribute simultaneously to the overall photocurrent and efficiency of the device.

Future directions for this work include exploring coupled plasmonic effects induced by various nanometer-sized metallic structures. In conjunction with the investigation of devices incorporated with specified size, shape, type, and density of MNPs in diverse layers of an OSC, the nanostructures exhibiting optimum results can be integrated in one single device simultaneously in order to combine the advantages from each structure.

Besides, the plasmonic effects induced by metallic arrays and gratings are of great interest. This could also be coupled with MNPs; that is, a metallic grating could be integrated on the back

electrode of a device in which MNPs are already deposited. As an example, the impacts of silver arrays on the back electrode of P3HT:PCBM bulk heterojunction OSC can be combined with plasmonic effects of Au NPs which are spin-casted on the ITO modified anode of the same device. Gold nanostars or nanoflowers would be interesting to explore in further studies because of their broad and rich absorption spectra.

Furthermore, the combined plasmonic effect induced by dissimilar metal nanostructures can also be investigated in tandem SCs.

REFERENCES

[1] D. Wöhrle and D. Meissner, "Organic solar cells," *Advanced Materials*, vol. 3, no. 3, pp. 129–138, 1991. [Online]. Available: http://dx.doi.org/10.1002/adma.19910030303

[2] I. E. Agency, "Clean energy technologies." [Online]. Available: http://www.iea.org/-topics/cleanenergytechnologies/

[3] L. Li, G. Lu, X. Yang, E. Zhou *et al.*, "Progress in polymer solar cell," *Chinese Science Bulletin*, vol. 52, no. 2, pp. 145–158, 2007.

[4] A. Abass, "Plasmonic nanostructures for absorption enhancement in organic solar cells," Master's thesis, Erasmus Mundus, 2009-2010.

[5] Y. Liang, Z. Xu, J. Xia, S.-T. Tsai, Y. Wu, G. Li, C. Ray, and L. Yu, "For the bright Future—Bulk heterojunction polymer solar cells with power conversion efficiency of 7.4%," *Adv. Mater.*, vol. 22, no. 20, pp. E135–E138, 2010. [Online]. Available: http://dx.doi.org/-10.1002/adma.200903528

[6] C. Tang, "Two-layer organic photovoltaic cell," *Applied Physics Letters*, vol. 48, no. 2, pp. 183–185, 1986.

[7] G. Yu, C. Zhang, and A. Heeger, "Dual-function semiconducting polymer devices: Light-emitting and photodetecting diodes," *Applied physics letters*, vol. 64, no. 12, pp. 1540–1542, 1994.

[8] G. Yu, J. Gao, J. Hummelen, F. Wudl, and A. Heeger, "Polymer photovoltaic cells: enhanced efficiencies via a network of internal donor-acceptor heterojunctions," *Science-AAAS-Weekly Paper Edition*, vol. 270, no. 5243, pp. 1789–1790, 1995.

[9] C. Brabec, S. Shaheen, C. Winder, N. Sariciftci, and P. Denk, "Effect of lif/metal electrodes on the performance of plastic solar cells," *Applied physics letters*, vol. 80, no. 7, pp. 1288–1290, 2002.

[10] H. Hoppe, M. Niggemann, C. Winder, J. Kraut, R. Hiesgen, A. Hinsch, D. Meissner, and N. Sariciftci, "Nanoscale morphology of conjugated polymer/fullerene-based bulk-heterojunction solar cells," *Advanced Functional Materials*, vol. 14, no. 10, pp. 1005–1011, 2004. [Online]. Available: http://dx.doi.org/10.1002/adfm.200305026

[11] X. Yang, A. Alexeev, M. Michels, and J. Loos, "Effect of spatial confinement on the morphology evolution of thin poly (p-phenylenevinylene)/methanofullerene composite films," *Macromolecules*, vol. 38, no. 10, pp. 4289–4295, 2005.

[12] Y. Eo, H. Rhee, B. Chin, and J. Yu, "Influence of metal cathode for organic photovoltaic device performance," *Synthetic Metals*, vol. 159, no. 17, pp. 1910–1913, 2009.

[13] S. Alem, J. Gao, and G. Wantz, "Photovoltaic response of symmetric sandwich polymer cells with identical electrodes," *Journal of Applied Physics*, vol. 106, no. 4, pp. 044505–044505, 2009.

[14] S. Alem, R. de Bettignies, J. Nunzi, and M. Cariou, "Efficient polymer-based interpenetrated network photovoltaic cells," *Applied physics letters*, vol. 84, no. 12, pp. 2178–2180, 2004.

[15] P. Frederik C. Krebs, *Polymer Photovoltaics: A Practical Approach*, ser. Spie Press Monograph. Society of Photo Optical, 2008. [Online]. Available: http://books.google.ca/-books?id=v3bDowFRo9UC

[16] T. Ameri, G. Dennler, C. Lungenschmied, and C. Brabec, "Organic tandem solar cells: A review," *Energy & Environmental Science*, vol. 2, no. 4, pp. 347–363, 2009.

[17] J. Lee, J. Park, J. Kim, D. Lee, and K. Cho, “High efficiency polymer solar cells with wet deposited plasmonic gold nanodots,” *Organic Electronics*, vol. 10, no. 3, pp. 416–420, 2009.

[18] A. Yakimov and S. Forrest, “High photovoltage multiple-heterojunction organic solar cells incorporating interfacial metallic nanoclusters,” *Applied Physics Letters*, vol. 80, no. 9, pp. 1667–1669, 2002.

[19] S. Kim, S. Na, J. Jo, D. Kim, and Y. Nah, “Plasmon enhanced performance of organic solar cells using electrodeposited ag nanoparticles,” *Applied Physics Letters*, vol. 93, no. 7, pp. 073307–073307, 2008.

[20] A. Y. Mahmoud, J. Zhang, J. K. Baral, R. Izquierdo, D. Ma, M. Packirisamy, and V.-V. Truong, “Low density of gold nanorods in the anodic layer for enhancing the efficiency of organic solar cells,” 2011, pp. 80071V–80071V–9. [Online]. Available: + http://dx.doi.org/-10.1117/12.904055

[21] J. Wu, F. Chen, Y. Hsiao, F. Chien, P. Chen, C. Kuo, M. Huang, C. Hsu *et al.*, “Surface plasmonic effects of metallic nanoparticles on the performance of polymer bulk heterojunction solar cells,” *ACS nano*, vol. 5, no. 2, p. 959, 2011.

[22] F. Chen, J. Wu, C. Lee, Y. Hong, C. Kuo, and M. Huang, “Plasmonic-enhanced polymer photovoltaic devices incorporating solution-processable metal nanoparticles,” *Applied Physics Letters*, vol. 95, no. 1, pp. 013305–013305, 2009.

[23] A. Mahmoud, N. Alamdari, R. Izquierdo, and V. Truong, “Gold nanorods on the cathode electrode for enhancing the efficiency of polymer solar cells,” in *Photonics North 2012*. International Society for Optics and Photonics, 2012, pp. 84121M–84121M.

[24] M. Park, B. Chin, J. Yu, M. Chun, and S. Han, “Enhanced photocurrent and efficiency of poly (3-hexylthiophene)/fullerene photovoltaic devices by the incorporation of gold

nanoparticles," *Journal of Industrial and Engineering Chemistry*, vol. 14, no. 3, pp. 382–386, 2008.

[25] D. Wang, D. Kim, K. Choi, J. Seo, S. Im, J. Park, O. Park, and A. Heeger, "Enhancement of donor–acceptor polymer bulk heterojunction solar cell power conversion efficiencies by addition of au nanoparticles," *Angewandte Chemie*, vol. 123, no. 24, pp. 5633–5637, 2011.

[26] J. Yang, J. You, C. Chen, W. Hsu, H. Tan, X. Zhang, Z. Hong, and Y. Yang, "Plasmonic polymer tandem solar cell," *ACS nano*, vol. 5, no. 8, pp. 6210–6217, 2011.

[27] P. Heremans, D. Cheyns, and B. Rand, "Strategies for increasing the efficiency of heterojunction organic solar cells: material selection and device architecture," *Accounts of chemical research*, vol. 42, no. 11, pp. 1740–1747, 2009.

[28] N. Sam-Shajing Sun and N. Sariciftci, *Organic Photovoltaics: Mechanism, Materials, And Devices*, ser. Optical Engineering Series. Taylor & Francis Group, 2005. [Online]. Available: http://books.google.ca/books?id=0RHNYMQmOVsC

[29] C. Heine and R. Morf, "Submicrometer gratings for solar energy applications," *Applied Optics*, vol. 34, no. 14, pp. 2476–2482, 1995.

[30] V. Shrotriya, E. Wu, G. Li, Y. Yao, and Y. Yang, "Efficient light harvesting in multiple-device stacked structure for polymer solar cells," *Applied physics letters*, vol. 88, no. 6, pp. 064104–064104, 2006.

[31] A. Moulé, J. Bonekamp, and K. Meerholz, "The effect of active layer thickness and composition on the performance of bulk-heterojunction solar cells," *Journal of applied physics*, vol. 100, no. 9, pp. 094503–094503, 2006.

[32] T. Savenije, *ORGANIC SOLAR CELLS*. Delft University of Technology.

[33] G. Dennler, M. Scharber, and C. Brabec, “Polymer-fullerene bulk-heterojunction solar cells,” *Advanced Materials*, vol. 21, no. 13, pp. 1323–1338, 2009.

[34] J. Nunzi, “Organic photovoltaic materials and devices,” *Comptes Rendus Physique*, vol. 3, no. 4, pp. 523–542, 2002.

[35] P. Miranda, D. Moses, and A. Heeger, “Ultrafast photogeneration of charged polarons in conjugated polymers,” *Physical Review B*, vol. 64, no. 8, p. 081201, 2001.

[36] P. Peumans, A. Yakimov, and S. Forrest, “Small molecular weight organic thin-film photodetectors and solar cells,” *Journal of Applied Physics*, vol. 93, no. 7, pp. 3693–3723, 2003.

[37] S. Gunes, H. Neugebauer, and N. Sariciftci, “Conjugated polymer-based organic solar cells,” *Chemical Reviews-Columbus*, vol. 107, no. 4, pp. 1324–1338, 2007.

[38] R. A. Street, M. Schoendorf, A. Roy, and J. H. Lee, “Interface state recombination in organic solar cells,” *Phys. Rev. B*, vol. 81, p. 205307, May 2010. [Online]. Available: http://-link.aps.org/doi/10.1103/PhysRevB.81.205307

[39] C. Im, W. Tian, H. Bässler, A. Fechtenkötter, M. Watson, and K. Müllen, “Photoconduction in organic donor–acceptor systems,” *The Journal of chemical physics*, vol. 119, p. 3952, 2003.

[40] A. Pivrikas, N. S. Sariciftci, G. JuÅ¡ka, and R. Ã–sterbacka, “A review of charge transport and recombination in polymer/fullerene organic solar cells,” *Progress in Photovoltaics: Research and Applications*, vol. 15, no. 8, pp. 677–696, 2007. [Online]. Available: http://-dx.doi.org/10.1002/pip.791

[41] S. Uchida, J. Xue, B. Rand, and S. Forrest, “Organic small molecule solar cells with a homogeneously mixed copper phthalocyanine: C60active layer,” *Applied physics letters*, vol. 84, no. 21, pp. 4218–4220, 2004.

[42] Y. Cheng, S. Yang, C. Hsu *et al.*, "Synthesis of conjugated polymers for organic solar cell applications," *ChemInform*, vol. 41, no. 13, 2010.

[43] H. Hoppe and N. S. Sariciftci, "Morphology of polymer/fullerene bulk heterojunction solar cells," *J. Mater. Chem.*, vol. 16, pp. 45–61, 2006. [Online]. Available: http://dx.doi.org/-10.1039/B510618B

[44] R. Janssen, J. Hummelen, and N. Sariciftci, "Polymer–fullerene bulk heterojunction solar cells," *MRS bulletin*, vol. 30, no. 01, pp. 33–36, 2005.

[45] E. Bundgaard and F. C. Krebs, "Low band gap polymers for organic photovoltaics," *Solar Energy Materials and Solar Cells*, vol. 91, no. 11, pp. 954 – 985, 2007. [Online]. Available: http://www.sciencedirect.com/science/article/pii/S0927024807000451

[46] K. Colladet, S. Fourier, T. J. Cleij, L. Lutsen, J. Gelan, D. Vanderzande, L. Huong Nguyen, H. Neugebauer, S. Sariciftci, A. Aguirre, G. Janssen, and E. Goovaerts, "Low band gap donor. acceptor conjugated polymers toward organic solar cells applications," *Macromolecules*, vol. 40, no. 1, pp. 65 – 72, 2007. [Online]. Available: http://pubs.acs.org/doi/-abs/10.1021/ma061760i

[47] K. Kawano, R. Pacios, D. Poplavskyy, J. Nelson, D. Bradley, and J. Durrant, "Degradation of organic solar cells due to air exposure," *Solar energy materials and solar cells*, vol. 90, no. 20, pp. 3520–3530, 2006.

[48] X. Yang, J. Loos, S. Veenstra, W. Verhees, M. Wienk, J. Kroon, M. Michels, and R. Janssen, "Nanoscale morphology of high-performance polymer solar cells," *Nano Letters*, vol. 5, no. 4, pp. 579–583, 2005.

[49] B. Gregg, "Excitonic solar cells," *The Journal of Physical Chemistry B*, vol. 107, no. 20, pp. 4688–4698, 2003.

[50] H. Hoppea and N. Sariciftci, “Organic solar cells: An overview,” *J. Mater. Res*, vol. 19, no. 7, p. 1925, 2004.

[51] S. Sze and K. Ng, *Physics of semiconductor devices*. Wiley-interscience, 2006.

[52] J. Rostalski and D. Meissner, “Monochromatic versus solar efficiencies of organic solar cells,” *Solar Energy Materials and Solar Cells*, vol. 61, no. 1, pp. 87 – 95, 2000. [Online]. Available: http://www.sciencedirect.com/science/article/pii/S0927024899000999

[53] L. Pettersson, L. Roman, and O. Inganas, “Modeling photocurrent action spectra of photovoltaic devices based on organic thin films,” *Journal of Applied Physics*, vol. 86, no. 1, pp. 487–496, 1999.

[54] J. Liu, Y. Shi, and Y. Yang, “Solvation-induced morphology effects on the performance of polymer-based photovoltaic devices,” *Advanced Functional Materials*, vol. 11, no. 6, pp. 420–424, 2001.

[55] B. P. Rand, D. P. Burk, and S. R. Forrest, “Offset energies at organic semiconductor heterojunctions and their influence on the open-circuit voltage of thin-film solar cells,” *Phys. Rev. B*, vol. 75, p. 115327, Mar 2007. [Online]. Available: http://link.aps.org/doi/10.1103/-PhysRevB.75.115327

[56] V. D. Mihailetchi, P. W. M. Blom, J. C. Hummelen, and M. T. Rispens, “Cathode dependence of the open-circuit voltage of polymer:fullerene bulk heterojunction solar cells,” *Journal of Applied Physics*, vol. 94, no. 10, pp. 6849 –6854, nov 2003.

[57] F. Monestier, J.-J. Simon, P. Torchio, L. Escoubas, F. Flory, S. Bailly, R. de Bettignies, S. Guillerez, and C. Defranoux, “Modeling the short-circuit current density of polymer solar cells based on p3ht:pcbm blend,” *Solar Energy Materials and Solar Cells*, vol. 91, no. 5, pp. 405 –

410, 2007. [Online]. Available: http://www.sciencedirect.com/science/article/pii/-S0927024806004247

[58] Y. M. Nam, J. Huh, and W. H. Jo, "Optimization of thickness and morphology of active layer for high performance of bulk-heterojunction organic solar cells," *Solar Energy Materials and Solar Cells*, vol. 94, no. 6, pp. 1118 – 1124, 2010. [Online]. Available: http://-www.sciencedirect.com/science/article/pii/S0927024810000942

[59] E. Chiew, M. Yahaya, and A. Othman, "Electrical characterization of p3ht/pcbm bulk heterojunction organic solar cell," *International Journal of Computational Materials Science and Engineering*, vol. 1, no. 01, 2012.

[60] C. Tabor, "Some optical and catalytic properties of metallic nanoparticles," Ph.D. dissertation, Georgia Institute of Technology, 2010.

[61] A. Skirtach, C. Dejugnat, D. Braun, A. Susha, A. Rogach, W. Parak, H. Möhwald, and G. Sukhorukov, "The role of metal nanoparticles in remote release of encapsulated materials," *Nano letters*, vol. 5, no. 7, pp. 1371–1377, 2005.

[62] H. Atwater and A. Polman, "Plasmonics for improved photovoltaic devices," *Nature materials*, vol. 9, no. 3, pp. 205–213, 2010.

[63] J. Homola, *Surface plasmon resonance based sensors*. Springer, 2006, vol. 4.

[64] N. Fang, H. Lee, C. Sun, and X. Zhang, "Sub–diffraction-limited optical imaging with a silver superlens," *Science*, vol. 308, no. 5721, pp. 534–537, 2005.

[65] L. Hirsch, R. Stafford, J. Bankson, S. Sershen, B. Rivera, R. Price, J. Hazle, N. Halas, and J. West, "Nanoshell-mediated near-infrared thermal therapy of tumors under magnetic resonance guidance," *Proceedings of the National Academy of Sciences*, vol. 100, no. 23, pp. 13549–13554, 2003.

[66] D. Koller, A. Hohenau, H. Ditlbacher, N. Galler, F. Reil, F. Aussenegg, A. Leitner, E. List, and J. Krenn, "Organic plasmon-emitting diode," *Nature Photonics*, vol. 2, no. 11, pp. 684–687, 2008.

[67] E. Hutter and J. Fendler, "Exploitation of localized surface plasmon resonance," *Advanced Materials*, vol. 16, no. 19, pp. 1685–1706, 2004.

[68] J. Zhang and C. Noguez, "Plasmonic optical properties and applications of metal nanostructures," *Plasmonics*, vol. 3, no. 4, pp. 127–150, 2008.

[69] G. Mie, "Beiträge zur optik trüber medien, speziell kolloidaler metallösungen," *Annalen der Physik*, vol. 330, no. 3, pp. 377–445, 1908. [Online]. Available: http://dx.doi.org/10.1002/-andp.19083300302

[70] I. Freestone, N. Meeks, M. Sax, and C. Higgitt, "The lycurgus cup–a roman nanotechnology," *Gold Bulletin*, vol. 40, no. 4, pp. 270–277, 2007.

[71] M. Garcia, "Surface plasmons in metallic nanoparticles: fundamentals and applications," *Journal of Physics D: Applied Physics*, vol. 44, no. 28, p. 283001, 2011.

[72] A. Zayats and I. Smolyaninov, "Near-field photonics: surface plasmon polaritons and localized surface plasmons," *Journal of Optics A: Pure and Applied Optics*, vol. 5, no. 4, p. S16, 2003.

[73] A. Trügler and U. Hohenester, "Optical properties of metallic nanoparticles," Ph.D. dissertation, Doctoral thesis at the Karl-Franzens University Graz, 2011.

[74] B.Lamprecht, "Ultrafast plasmon dynamics in metal nanoparticles," Ph.D. dissertation, Dissertation at the Karl-Franzens University of Graz, Institute for Experimental Physics, 2000.

[75] S. Maier, *Plasmonics: Fundamentals and Applications*. Springer, 2007. [Online]. Available: http://books.google.ca/books?id=yT2ux7TmDc8C

[76] C. Bohren, “How can a particle absorb more than the light incident on it?” *American Journal of Physics*, vol. 51, pp. 323–327, 1983.

[77] K. Kelly, E. Coronado, L. Zhao, and G. Schatz, “The optical properties of metal nanoparticles: the influence of size, shape, and dielectric environment,” *The Journal of Physical Chemistry B*, vol. 107, no. 3, pp. 668–677, 2003.

[78] M. Pelton, J. Aizpurua, and G. Bryant, “Metal-nanoparticle plasmonics,” *Laser & Photonics Reviews*, vol. 2, no. 3, pp. 136–159, 2008.

[79] U. Kreibig, B. Schmitz, and H. Breuer, “Separation of plasmon-polariton modes of small metal particles,” *Physical Review B*, vol. 36, pp. 5027–5030, 1987.

[80] C. Sönnichsen, T. Franzl, T. Wilk, G. Von Plessen, and J. Feldmann, “Plasmon resonances in large noble-metal clusters,” *New Journal of Physics*, vol. 4, no. 1, p. 93, 2002.

[81] M. Shopa, K. Kolwas, A. Derkachova, and G. Derkachov, “Dipole and quadrupole surface plasmon resonance contributions in formation of near-field images of a gold nanosphere,” *Opto-Electronics Review*, vol. 18, no. 4, pp. 421–428, 2010.

[82] I. Sosa, C. Noguez, and R. Barrera, “Optical properties of metal nanoparticles with arbitrary shapes,” *The Journal of Physical Chemistry B*, vol. 107, no. 26, pp. 6269–6275, 2003.

[83] O. Muskens, D. Christofilos, N. Del Fatti, and F. Vallée, “Optical response of a single noble metal nanoparticle,” *Journal of Optics A: Pure and Applied Optics*, vol. 8, no. 4, p. S264, 2006.

[84] P. Jain, X. Huang, I. El-Sayed, and M. El-Sayed, “Noble metals on the nanoscale: optical and photothermal properties and some applications in imaging, sensing, biology, and medicine,” *Accounts of Chemical Research*, vol. 41, no. 12, pp. 1578–1586, 2008.

[85] M. Hu, J. Chen, Z. Li, L. Au, G. Hartland, X. Li, M. Marquez, and Y. Xia, "Gold nanostructures: engineering their plasmonic properties for biomedical applications," *Chemical Society Reviews*, vol. 35, no. 11, pp. 1084–1094, 2006.

[86] P. Jain, S. Eustis, and M. El-Sayed, "Plasmon coupling in nanorod assemblies: optical absorption, discrete dipole approximation simulation, and exciton-coupling model," *The Journal of Physical Chemistry B*, vol. 110, no. 37, pp. 18243–18253, 2006.

[87] L. Liz-Marzán, "Nanometals," *reactions*, vol. 17, p. 18, 2004.

[88] H. Chen, X. Kou, Z. Yang, W. Ni, and J. Wang, "Shape-and size-dependent refractive index sensitivity of gold nanoparticles," *Langmuir*, vol. 24, no. 10, pp. 5233–5237, 2008.

[89] M. Miller and A. Lazarides, "Sensitivity of metal nanoparticle plasmon resonance band position to the dielectric environment as observed in scattering," *Journal of Optics A: Pure and Applied Optics*, vol. 8, no. 4, p. S239, 2006.

[90] S. Ghosh, T. Pal *et al.*, "Interparticle coupling effect on the surface plasmon resonance of gold nanoparticles: from theory to applications," *Chemical Reviews-Columbus*, vol. 107, no. 11, pp. 4797–4862, 2007.

[91] A. Welles, *Silver Nanoparticles: Properties, Characterization and Applications*, ser. Nanotechnology Science and Technology Series. Nova Science Pub Incorporated, 2010. [Online]. Available: http://books.google.ca/books?id=LeP6RQAACAAJ

[92] S. J. Oldenburg. Silver nanoparticles: Properties and applications. [Online]. Available: http://www.sigmaaldrich.com/materials-science/nanomaterials/silver-nanoparticles.html

[93] Nanocomposix, "Silver nanoparticles: Optical properties." [Online]. Available: http://-nanocomposix.com/kb/silver/optical-properties#size

[94] M. Stockman, “Nanoplasmonics: past, present, and glimpse into future,” *Optics Express*, vol. 19, no. 22, pp. 22029–22106, 2011.

[95] S. Derom, R. Vincent, A. Bouhelier, and G. des Francs, “Resonance quality, radiative/ohmic losses and modal volume of mie plasmons,” *EPL (Europhysics Letters)*, vol. 98, no. 4, p. 47008, 2012.

[96] J. Pérez-Juste, I. Pastoriza-Santos, L. Liz-Marzán, and P. Mulvaney, “Gold nanorods: synthesis, characterization and applications,” *Coordination Chemistry Reviews*, vol. 249, no. 17, pp. 1870–1901, 2005.

[97] “Nanopartz™ bare gold nanorodz™.” [Online]. Available: http://www.nanopartz.com/-bare_gold_nanorods.asp

[98] H. Nakashima, “Control of gold nanorod arrays through self-assembly of biomolecules,” *NTT Technical Review*, vol. 7, no. 8, pp. 1–5, 2009.

[99] R. Harrison and A. Ben-Yakar, “Role of near-field enhancement in plasmonic laser nanoablation using gold nanorods on a silicon substrate,” *Optics Express*, vol. 18, no. 21, pp. 22556–22571, 2010.

[100] S. Pillai and M. Green, “Plasmonics for photovoltaic applications,” *Solar Energy Materials and Solar Cells*, vol. 94, no. 9, pp. 1481–1486, 2010.

[101] M. Green and S. Pillai, “Harnessing plasmonics for solar cells,” *Nature Photonics*, vol. 6, no. 3, pp. 130–132, 2012.

[102] S. Basu Mallick, N. Sergeant, M. Agrawal, J. Lee, and P. Peumans, “Coherent light trapping in thin-film photovoltaics,” *MRS bulletin*, vol. 36, no. 06, pp. 453–460, 2011.

[103] Y. Akimov and W. Koh, “Resonant and nonresonant plasmonic nanoparticle enhancement for thin-film silicon solar cells,” *Nanotechnology*, vol. 21, no. 23, p. 235201, 2010.

[104] D. Duche, P. Torchio, L. Escoubas, F. Monestier, J. Simon, F. Flory, and G. Mathian, "Improving light absorption in organic solar cells by plasmonic contribution," *Solar Energy Materials and Solar Cells*, vol. 93, no. 8, pp. 1377–1382, 2009.

[105] F. Liu and J. Nunzi, "Enhanced organic light emitting diode and solar cell performances using silver nano-clusters," *Organic Electronics*, 2012.

[106] L. Qiao, D. Wang, L. Zuo, Y. Ye, J. Qian, H. Chen, and S. He, "Localized surface plasmon resonance enhanced organic solar cell with gold nanospheres," *Applied Energy*, vol. 88, no. 3, pp. 848–852, 2011.

[107] A. Morfa, K. Rowlen, T. Reilly, M. Romero, and J. van de Lagemaat, "Plasmon-enhanced solar energy conversion in organic bulk heterojunction photovoltaics," *Applied Physics Letters*, vol. 92, no. 1, pp. 013504–013504, 2008.

[108] W. Yoon, K. Jung, J. Liu, T. Duraisamy, R. Revur, F. Teixeira, S. Sengupta, and P. Berger, "Plasmon-enhanced optical absorption and photocurrent in organic bulk heterojunction photovoltaic devices using self-assembled layer of silver nanoparticles," *Solar Energy Materials and Solar Cells*, vol. 94, no. 2, pp. 128–132, 2010.

[109] A. Mahmoud, J. Zhang, D. Ma, R. Izquierdo, and V. Truong, "Optically-enhanced performance of polymer solar cells with low concentration of gold nanorods in the anodic buffer layer," *Organic Electronics*, 2012.

[110] F. Tang, J. Chang, W. Chou, H. Cheng, S. Hsu, J. Chen, and H. Sheu, "Effective oxygen plasma treatment on indium tin oxide electrode to improve organic solar cell efficiency," *physica status solidi (a)*, 2012.

[111] L. Nguyen, H. Hoppe, T. Erb, S. Günes, G. Gobsch, and N. Sariciftci, "Effects of annealing on the nanomorphology and performance of poly (alkylthiophene): Fullerene bulk-heterojunction solar cells," *Advanced Functional Materials*, vol. 17, no. 7, pp. 1071–1078, 2007.

[112] R. Steim, T. Ameri, P. Schilinsky, C. Waldauf, G. Dennler, M. Scharber, and C. Brabec, "Organic photovoltaics for low light applications," *Solar Energy Materials and Solar Cells*, vol. 95, no. 12, pp. 3256–3261, 2011.

[113] J. Blakesley and D. Neher, "Relationship between energetic disorder and open-circuit voltage in bulk heterojunction organic solar cells," *Physical Review B*, vol. 84, no. 7, p. 075210, 2011.

[114] R. S. Kim, J. Zhu, J. H. Park, L. Li, Z. Yu, H. Shen, M. Xue, K. L. Wang, G. Park, T. J. Anderson, and Q. Pei, "E-beam deposited ag-nanoparticles plasmonic organic solar cell and its absorption enhancement analysis using fdtd-based cylindrical nano-particle optical model," *Opt. Express*, vol. 20, no. 12, pp. 12649–12657, Jun 2012. [Online]. Available: http://-www.opticsexpress.org/abstract.cfm?URI=oe-20-12-12649

[115] D. Derkacs, S. Lim, P. Matheu, W. Mar, and E. Yu, "Improved performance of amorphous silicon solar cells via scattering from surface plasmon polaritons in nearby metallic nanoparticles," *Applied Physics Letters*, vol. 89, no. 9, pp. 093103–093103, 2006.

[116] M. Van Dijk, A. Tchebotareva, M. Orrit, M. Lippitz, S. Berciaud, D. Lasne, L. Cognet, and B. Lounis, "Absorption and scattering microscopy of single metal nanoparticles," *Phys. Chem. Chem. Phys.*, vol. 8, no. 30, pp. 3486–3495, 2006.

[117] K. Catchpole and A. Polman, "Design principles for particle plasmon enhanced solar cells," *Applied Physics Letters*, vol. 93, no. 19, pp. 191113–191113, 2008.

[118] I. Kim, T. Lee, D. Jeong, W. Lee, and K. Lee, "Size effects of metal nanoparticles embedded in a buffer layer of organic photovoltaics on plasmonic absorption enhancement," *Journal of Physics D: Applied Physics*, vol. 45, no. 6, p. 065101, 2012.

[119] X. Chen, C. Zhao, L. Rothberg, and M. Ng, "Plasmon enhancement of bulk heterojunction organic photovoltaic devices by electrode modification," *Applied Physics Letters*, vol. 93, no. 12, pp. 123302–123302, 2008.